Modélisation par éléments finis de la propagation des ondes ultrasonores dans des matériaux polycristallins

Xue Bai

NNT : 2017SACLC004

THESE DE DOCTORAT
DE
L'UNIVERSITE PARIS-SACLAY
PREPAREE A
"CENTRALESUPELEC"

ECOLE DOCTORALE N° 579
Sciences mécaniques et énergétiques, matériaux et géosciences
Spécialité de doctorat: mécanique des matériaux

Par

Xue BAI

Finite Element Modeling of Ultrasonic Wave Propagation in Polycrystalline Materials

Thèse présentée et soutenue à Châtenay-Malabry, le 02 Février 2017:

Composition du Jury :

M. Jean-Pierre VILOTTE	Professeur des universités, IPGP	Président
M. Alain LHÉMERY	Directeur de recherche, CEA Tech	Rapporteur
M. Joseph MOYSAN	Professeur des Universités, GMP, IUT, AMU	Rapporteur
M. Bertrand CHASSIGNOLE	Senior Scientiste, EDF Recherche et Développement	Examinateur
M. Denis AUBRY	Professeur, CentraleSupélec	Directeur de thèse
M. Jean-Hubert SCHMITT	Professeur, CentraleSupélec	Co-directeur de thèse
Mme. Bing TIE	Chargé de recherche, CentraleSupélec	Co-directrice de thèse

Acknowledgements

I finished this thesis in the Lab. Mécanique des Sols, Structures et Matériaux (MSSMat) at CentraleSupélec of the University of Paris-Saclay, financed by the China Scholarship Council (CSC) and the French National Centre for Scientific Research (CNRS). I would like to express my gratitude to all those who helped me during my PhD study.

My deepest gratitude goes first and foremost to my three supervisors: Mr. Denis AUBRY, Professor in the Lab. MSSMat at CentraleSupélec, Mr. Jean-Hubert Schmitt, Professor in the Lab. MSSMat at CentraleSupélec, and Mme. Bing TIE, CNRS Researcher in the Lab. MSSMat at CentraleSupélec, for their excellent guidance on my research work. Without their helpful suggestions and illuminating instruction, this thesis could not have researched its present form. It was a distinct privilege to work with three excellent supervisors together over the past three years and four months, during which time I learned a lot from them, not only various skills in theoretical and numerical investigations on ultrasonic inspections of polycrystalline microstructures, but also the attitude as a scientific researcher. They attended the regular meetings of my thesis almost once a week, to discuss each complex physical phenomenon and to provide me with inspiring advice. They took each detailed step of the formula derivation extremely seriously. They listened carefully to my academic presentations for international conferences and proposed valuable suggestions for modifications. Without their patient instruction, insightful criticism and expert guidance, the completion of this thesis would not have been possible.

I would like to express my special appreciation to the members of the defense committee: the president Mr. Jean-Pierre VILLOT, Professor in the Institute of Earth Physics of Paris, the examinator Mr. Bertrand CHASSIGNOLE, Senior Scientist in EDF Research and Development, the rapporteurs Mr. Alain LHELERY, Research Director in the CEA Tech, and Mr. Joseph MOYSAN, Professor in the Aix Marseille University. I am grateful for their brilliant comments and valuable suggestions on my research work, and for offering me a great of encouragement.

My sincere thanks are also given to all the teachers and staff members in the Lab. MSSMat, especially to Mme. Anne-Sophie MOURONVAL, Engineer in the computational science who have helped me a lot with the calculation implementation on the computing center; Mme. Véronique AUBIN, Professor in the Lab. MSSMat who contributed some helpful suggestions on my research in the regular meeting of the mechanics of materials research group; Mr. Jean-Marie FLEUREAU, Professor in the Lab. MSSMat who provided me with valuable advice for revising the manuscript of the thesis.

I would like to extend my heartful gratitude to many other colleagues in the Lab. MSSMat, with whom I discussed academic issues, spent the happy lunch time and coffee breaks, and shared all my

joy and sadness. They have offered me various kind help. Only a few are named here: Wen XU, Wang CHOW, Aurélie JAMONEA, Gilles LENOIR, Ahmed SRIDI, Michael CALLAHAN, Mathieu BONNERIC, Lucio DE ABREU CORREA, Maroua HAMMANI, Solenne DEVERAUX, Angkeara SVAY, Khalil ABENE, Filippo GATTI, Luciano DE CARVALHO PALUDO, Benhui FAN, Hang ZHAO, Yu LIU, Shuimiao DU, Delong HE, Shan FENG etc.

I feel grateful to Mr. Denis SOLAS, Associate Professor in the Paris-sud University, who gave me excellent guidance on the representation of crystallographic orientation and the calculation of the misorientation between two grains; and Mr. Tomas GARCIN, Research Associate in the Department of Materials Engineering at the University of British Columbia, with whom I discussed some interesting physical issues of ultrasonic wave propagation in polycrystalline materials during his visit to the Lab. MSSMat and also on the Facebook.

Last but not the least, I would like to extend my gratitude to my beloved parents and all the other families who have always been supporting me and caring for me, to all my dear friends, who live in China but also care for my safety in France.

Abstract

Correlation of ultrasonic wave propagation properties to polycrystalline microstructure features has significant implications in non-destructive evaluation (NDE). A numerical approach based on the finite element (FE) method to quantify ultrasonic attenuation and grain-noise scattering coefficients in both time and frequency domains for polycrystalline materials is presented. It is applicable for any material regardless of its anisotropy, crystallographic or morphological textures (grain size, grain elongation, etc.), and consequently allows accessing to more realistic polycrystalline microstructures in a more accurate way than classical analytical models, for which assumptions such as the single scattering or the Born approximations are required. More particularly, an original method based on the reciprocity theorem for the numerical evaluation of the grain-noise scattering coefficient is proposed. The advantage of using the same theoretical frameworks as classical analytical models to develop our numerical procedure is that it allows to validate the latter in the cases of idealized textures for which the considered analytical models can be applied and remain relevant. Two-dimensional (2D) analytical formulas of ultrasonic attenuation and backscattering coefficients are developed by using the Born approximation to validate numerical evaluations.

Then the proposed numerical approach is applied to the single-phase and un-textured polycrystalline titanium. First, 2D FE simulations are performed in idealized microstructures composed of equiaxed grains with different unimodal grain sizes. The involved frequency range with respect to the considered grains sizes is large enough so that the Rayleigh and stochastic, and Rayleigh-to-stochastic transition scattering regions between them are studied. Coherent comparison between numerical estimates and 2D analytical predictions is obtained. Numerical results show that the attenuation and backscattering coefficients as a function of the ratio of grain size to wavelength increase continuously at low frequencies and become insensitive to high frequencies. 2D model reduces the scattering mechanism in the Rayleigh region, and a second power dependence on grain size of the longitudinal wave attenuation is observed instead of a third power dependence on grain size in the three-dimensional (3D) case. Complex physical phenomena, such as large dispersions of attenuation between samples with the same grain size but different spatial distributions of crystallographic orientations, and significant oscillation level of backscattering deduced from the insufficient number of grains contributing to received noise echo signals, are investigated. Effects of attenuation due to multiple scattering on the backscattering measurement are quantified.

Secondly, polycrystals with bimodal grain sizes, frequently observed during recrystallization or heterogeneous grain growth, are considered. The advantage of numerical modeling is highlighted in this case, as no analytical model exists. Effects of different parameters on ultrasonic attenuation and backscattering are investigated, such as the volume fraction of the larger grains, the random location or clusters of the larger grains in the matrix of the smaller grains, layered microstructures with bands

of the smaller and larger grains. Numerical results indicate that for all studied bimodal microstructures, attenuation and backscattering coefficients in frequency domain are in-between the ones of unimodal microstructures and are mainly determined by volume fractions of the constituent grains. However they are only slightly affected by the grain location distributions. It is concluded that characterization of layered microstructures with bands of different grain sizes by inversion of ultrasonic attenuation or backscattering coefficients is not straightforward. The spatial autocorrelation function in bimodal microstructures is further quantified to gain an analytical interpretation of the above phenomena.

Keywords: Finite Element, Ultrasonic Waves, Polycrystalline Materials, Ultrasonic Attenuation, Ultrasonic Backscattering

Contents

Introduction

The motivation for the research on the ultrasonic wave propagation in polycrystalline materials is found in non-destructive evaluation (NDE). Microstructural evolutions during metallurgical processes, such as rolling, forging or isothermally annealing, influence significantly the final material properties. Since the ultrasonic wave can deeply penetrate into most of polycrystalline materials, it has been widely used to characterize the polycrystalline microstructural features.

When an ultrasonic wave propagates through polycrystalline materials, inhomogeneities in elastic properties and in density of individual crystallites lead to the variation of propagation velocities in each crystallite, consequently resulting in the scattered noise signals and the amplitude attenuation. It is believed that information on microstructure features, such as grain size, crystallographic and morphological textures, can be obtained by inversion of ultrasonic signals. Correlation of ultrasonic propagation properties to microstructural features is a fundamental research for the NDE of microstructural evolution. The classical theoretical investigation provides a fundamental understanding of how elastic waves are attenuated and backscattered at grain boundaries. However, its development is restricted because complex physics, such as multiple-scattering and scattering mechanisms across different characteristic regions, incorporate with the scattering-induced attenuation and microstructural noise signals. FE modeling is a promising approach to provide a more complete model describing the complex physical mechanism of ultrasonic wave scattering. It allows accessing to realistic polycrystalline microstructures more accurately regardless of the anisotropy, crystallographic or morphological textures since no restrictive assumptions are used. Herein it is chosen as the methodology to answer our research questions.

As far as FE modeling of ultrasonic wave scattering in polycrystalline materials is concerned, the prior study (Van Pamel et al. 2015, Kumar et al. 1992, Chassignole et al. 2009) has been contributed to the evaluation of ultrasonic attenuation. However, complicated ultrasonic-microstructure interactions in polycrystals with high anisotropy can lead to a low level of signal-to-noise ratio in pulse-echo inspections, which makes the measurement of ultrasonic attenuation difficult. Therefore, it is of significance to characterize the microstructure by inversion of scattered grain noises using FE modeling, which is still an open question. Moreover, the numerical investigation is also motivated by the extension of the classical understanding to some complex physical issues, such as effects of grain size distribution and spatial distribution of crystallographic orientations on ultrasonic attenuation and backscattering, large dispersions of attenuation between samples with the same mean grain size, etc.

The purpose of this manuscript is to gain a more complete understanding of how polycrystalline microstructure features affect ultrasonic wave attenuation and backscattering by using FE modeling and thus to improve characterization of polycrystalline microstructures by inversion of ultrasonic attenuation and backscattering. Specifically, a versatile approach to numerically evaluate scattering-

induced attenuation and scattered noise signals is developed first. Then further investigations are made to understand grain size effects on ultrasonic attenuation and backscattering in a unimodal polycrystalline microstructure. The third objective of this manuscript is to answer the question whether the volume fraction ratio between fine and coarse grains or the grain location distributions in the microstructure with bimodal grain sizes would be detected by the ultrasonic inspection.

The first chapter is devoted to giving a review of theoretical, experimental and numerical studies on ultrasonic wave scattering in polycrystals. Classical theoretical models for formulating analyses of ultrasonic attenuation and microstructural noises are first recalled. Then some experimental studies, that confirm the classical theories in the case of simple polycrystals or invalidate them in more complex cases such as duplex titanium alloys, are presented. Confronting such kind of more challenging scattering scenarios, FE modeling is introduced as a promising approach and its recent research development is subsequently described. Limitations and difficulties for each approach are also discussed.

The second chapter is focused on the theoretical and numerical evaluations of ultrasonic attenuation and backscattering. General formulas for ultrasonic attenuation and microstructural noise scattering coefficients in three-dimensional (3D) polycrystalline materials are reviewed. As a new contribution, two-dimensional (2D) analytical formulas of longitudinal wave attenuation and backscattering coefficients in single-phase and untextured polycrystals with the Born approximation are developed for validation of the proposed numerical approach. As another interesting theoretical result, two components of the longitudinal wave attenuation, the longitudinal-to-longitudinal and longitudinal-to-shear scattering, are decomposed within the framework of the unified Stanke-Kino model. Finally, as one of the most important contributions of the present work, an original method for the numerical evaluation of microstructural noise scattering by using FE modeling is proposed, which is established using the same framework based on the reciprocity theorem.

In the third chapter, generation of 2D numerical models for idealized single-phase and untextured polycrystalline microstructures by using an in-house software OOFE (Object Oriented Finite Element program) is introduced. Analysis of mesh convergence is made and the choice for adequate averaging of elastic moduli to define the equivalent homogeneous medium of a polycrystal is subsequently discussed. Post-processing procedures of numerical ultrasonic data are presented, especially how the attenuation and backscattering coefficients are calculated for the defined numerical models is specified.

Numerical estimates in both frequency and time domains for the ultrasonic attenuation and backscattering in a single-phase and untextured polycrystalline titanium alloy with unimodal and bimodal grain sizes are presented in the fourth chapter. Concerning the unimodal microstructure, grain size effects on ultrasonic attenuation and backscattering are at first numerically evaluated. Quantitative comparison with the 2D analytical predictions is further conducted. Effects of spatial distributions of crystallographic orientations on ultrasonic attenuation and backscattering are additionally taken into

account. Discussions of the attenuation effects due to multiple scattering on the quantification of ultrasonic backscattering are proposed. With regard to the idealized microstructure containing double-size, hexagonal grains, effects of the volume fraction of the larger grains, the location distributions of the larger grains in the matrix of the smaller grains, and banded microstructure of the larger and smaller grains on ultrasonic attenuation and backscattering are investigated. The two-point spatial autocorrelation function is also investigated to provide an analytical interpretation of the numerical results.

Concluding remarks and perspectives of the research on ultrasonic wave scattering in polycrystalline materials by using FE modeling have been given in the final chapter.

Chapter 1

Literature review

For online quality control both in laboratory and in industry, the ultrasonic wave provides an approach of obtaining polycrystalline microstructure information continuously and non-destructively (Lindh-Ulmgren et al. 2004). Indeed when ultrasonic waves propagate through a polycrystal composed of numerous discrete grains of varying size and shape with anisotropic elastic properties and position-dependent crystallographic orientations (Fig. 1.1), they scatter at grain boundaries resulting in amplitude attenuation as well as microstructural noise scattering. Inversely, the polycrystalline microstructure could be characterized by inversion of its ultrasonic properties.

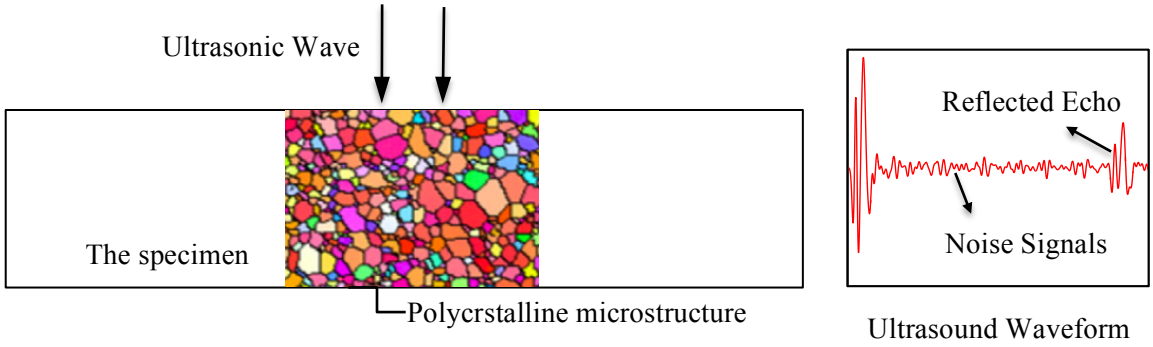

Fig. 1.1. Example of NDE of polycrystalline microstructure

In this chapter, inhomogeneities in a random polycrystalline medium are firstly introduced, which is the origin of ultrasonic wave scattering. Then, a review on the theoretical and experimental developments of ultrasonic wave scattering in polycrystals is given. Their development limitations are further analyzed. FE modeling is then presented as a promising methodology for improving ultrasonic inspections confronting more challenging scattering scenarios, and a recall on its current research progress is given. Advantages and restrictions of FE modeling for answering research questions about ultrasonic wave scattering is also presented. Since the dependence of ultrasonic properties on the polycrystalline microstructure has been investigated for many years, the literature work presented in this chapter is not exhaustive and only part of literature works directly related to the considered research questions in the present thesis are recalled.

1.1 Inhomogeneities in polycrystalline microstructures

A polycrystalline material is composed of numerous discrete grains, each having a regular crystalline atomic structure (Fig. 1.2.(a)), and its inhomogeneities consist in variations of shapes, sizes, crystallographic orientations and mechanical properties between grains. The shape of grains can be fairly spherical, elongated or fattened, and a wide grain size distribution can occur due to heterogeneous grain growth during thermomechanical processing. With respect to grain sizes and shapes, inhomogeneities associated with variations of crystallographic orientations and phases can be more significant.

Each crystallite in a polycrystalline medium is elastically anisotropic and has its own crystallographic orientation (Fig. 1.2.(b)). The elastic anisotropy of single crystal gives rise to inhomogeneous elastic constants in the global coordinate system of the polycrystal. Concerning singel-phase polycrystals, the overall crystallographic orientation distribution of the constituent grains defines the crystallographic texture of the polycrystal. The crystallographic texture affects significantly directionally dependent properties of a polycrystal, such as fracture toughness, electrical conductivity, superconductivity, etc. When all possible crystallographic orientations occur with equal frequency, the orientation dependence may disappear on an averaged macroscopic scale and in this specific case, the polycrystal is referred to be untextured. However, preferred orientation exists given that any crystallographic orientation with respect to the symmetry of the sample is more probable than others. Specific underlying mechanisms related to nucleation, growth, crystal plasticity and recrystallization as well as grain growth can lead to strong crystallographic textures as a result of synthesis and processing.

Furthermore, if all the grains do not have the same proportion of chemical constitutents, the same lattice constants or the same crystal structure, there are two or more phases. Phase transformations can lead to significant inhomogeneities of polycrystals.

In the view of ultrasonic wave propagation in single-phase polycrystalline materials, grain-to-grain variations of elastic properties trigger scattering phenomena at the grain boundaries, *i.e.* part of energy deviating from one straight trajectory into all directions. In the related literature, a simple variable, ξ, is classically defined to measure the departure of a polycrystalline medium from homogeneity (Stanke et al. 1984). In the case of a polycrystal with a low inhomogeneity degree, *i.e.* $\xi << 1$, ξ can be expressed in terms of the variance of elastic constants as follows (Stanke et al. 1984):

$$(\xi)^2 \cong \frac{1}{4} \frac{\langle (C_{ijkl}(\boldsymbol{x}) - C^0_{ijkl})^2 \rangle}{(C^0_{ijkl})^2} \tag{1.1}$$

where the subscript " *ijkl* " has the proper value for either the longitudinal wave or the shear wave, $C_{ijkl}(\boldsymbol{x})$ and C^0_{ijkl} denote the corresponding components of the fourth-order elastic moduli tensors in

the studied inhomogeneous domain and in the equivalent homogeneous medium, respectively. An ultrasonic wave propagating in such polycrystals scatters slightly at grain boundaries. Herein, a polycrystal of weak scattering refers to slight variation of elastic properties and so refers to a low degree of inhomogeneity..

The simplest polycryatlline microstructure is a single-phase and untextured material in the absence of dislocations, voids or defects. Many theorectical and experimental investigations have been made on elastic wave propagation in such a polycrystalline material, which is also considered in the present work.

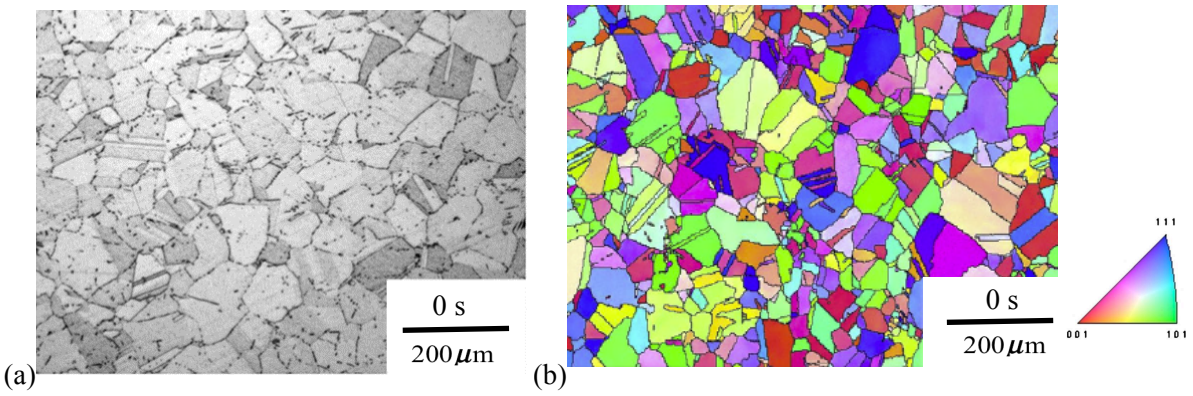

Fig. 1.2. (a) Optical micrograph and (b) EBSD map of a polycrystalline nickel alloy (Garcin et al. 2016).

1.2 Evaluation of scattering-induced attenuation

The attenuation measures the amplitude decay of elastic waves propagating in a polycrystal and is usually quantified by a scalar α called the attenuation coefficient. Both dissipation and scattering can cause the ultrasonic attenuation in polycrystalline materials. Attenuation by dissipation is caused by energy transformation into heat due to dislocations and the damping, etc. (Du et al. 2014). By contrast, attenuation by scattering is attributed to interactions between waves and grain boundaries due to inhomogeneities in elastic properties and in density between adjacent grains. It is mainly determined by the elastic anisotropy of the crystals, the grain size and shape, the crystallographic texture and the density variation. Thus, at least theoretically, some microstructure features are expected to be evaluated inversely by measuring the scattering-induced ultrasonic attenuation. In general, in the application of NDE by ultrasounds, the dissipation phenomenon is negligible with respect to the scattering phenomenon. In this thesis, the attenuation coefficient α specifically refers to the scattering-induced attenuation.

We note that in the following, both the subscript and the superscript “0” always indicate a mechanical field defined or obtained in the equivalent homogeneous medium, when it can be defined, of a heterogeneous medium. The parameter $\bar{d}$ denotes an effective average linear dimension of grains, λ_0 denotes wavelength and $k_0 = \omega / v_0$ denotes wave number in the equivalent homogeneous medium,

where $\omega = 2\pi f$ and v_0 are respectively the angular frequency and the phase velocity respectively. The amount and type of wave scattering at grain boundaries in a heterogeneous medium are strongly influenced by the ratio of grain size to wavelength and a normalized frequency parameter x_0 is classically defined by using this ratio (Stanke et al. 1984):

$$x_0 = k_0 \bar{d} = \frac{2\pi \bar{d}}{\lambda_0} = \frac{2\pi f \bar{d}}{v_0} \tag{1.2}$$

Three distinct frequency regions depending on this ratio are defined: the Rayleigh region where the grain size is much less than the wavelength, *i.e.* $x_0 << 1$, the stochastic region where the grain size is comparable to the wavelength, *i.e.* $1 < x_0 < 1/\xi$ and the geometric region where the grain size is much larger than the wavelength, *i.e.* $x_0 > 1/\xi$ (Fig. 1.3.).

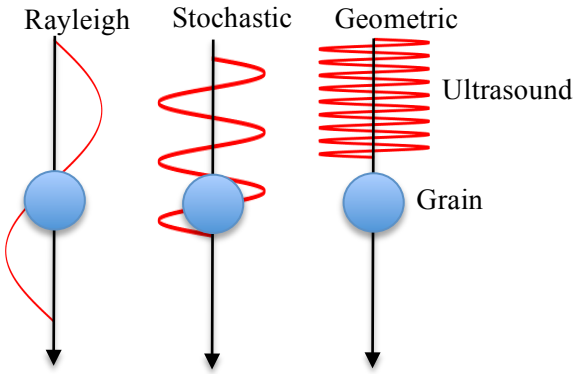

Fig. 1.3. Schematic of three scattering frequency regions

In this section, previous research on evaluation of ultrasonic scattering-induced attenuation in polycrystalline materials using theoretical and experimental methodologies is recalled. Open issues for ultrasonic attenuation are discussed according to limitations of the well-known existing theories and to difficulties of experimental measurements.

1.2.1 Theoretical investigations

Early theoretical investigation provides a basic understanding about the correlation of the ultrasonic wave scattering characteristics to the microstructure features of polycrystalline materials. Actually, elastic wave scattering in polycrystalline materials leads to complex physical phenomena, in particular, multiple-scattering effects, since the prior scattered waves are to be further scattered at grain boundaries. To get a first grasp, the single-scattering approximation is frequently used in early theoretical investigations, assuming that ultrasonic waves scatter at each grain boundary independently. At the beginning of this part, a recall on early investigations to develop the ultrasonic scattering theory based on the single-scattering assumption and the Born approximation is made. Consideration of multiple-scattering effects in the theoretical model is further introduced. Then, extension of those

well-known theories to effects of crystallographic textures and grain morphology on the ultrasonic scattering is presented and their limitations are finally discussed.

1.2.1.1 Single-scattering models

Early studies for the attenuation coefficient were limited to the Rayleigh scattering region. Bhatia performed the calculations for polycrystals with randomly-oriented grains having the same size with single-scattering approximation (Bhatia 1959). The attenuation coefficient was measured by the total scattering cross section of an isolated crystallite in an isotropic medium averaged over all crystallographic orientations multiplied by the number of grains per unit volume. It was valid only for slightly inhomogeneous materials due to the use of the first-order perturbation theory. Asymptotic formulas of attenuation coefficient in the Rayleigh region for polycrystals with cubic symmetry were presented. As Bhatia concluded, for an incident longitudinal wave, the scattered energy carried away by the shear wave due to mode conversion made a dominant contribution to the Rayleigh scattering.

A more general theory without limitation to the Rayleigh region was proposed by Hirsekorn (Hirsekorn 1982). She formulated the perturbation of the field in each scatterer using the Born series in power of the inhomogeneity degree ξ of polycrystals. Then she cut off the Born series after the second order term of ξ and performed the calculations of attenuation coefficient and velocities for a plane longitudinal wave in polycrystals with randomly oriented grains having the same size. As Stanke and Kino pointed out, her solution did not account for effects of multiple-scattering with the second-order perturbation theory, since exactly the same asymptotic results in the Rayleigh region as those derived by Bhatia were obtained (Stanke et al. 1984). The theory of Hirsekorn was limited to weakly anisotropic materials and was not valid in the frequency region beyond the stochastic scattering region.

It is noted that the Born approximation is adopted in both calculations by Hirsekorn and Bhatia, based on which the actual field in the studied domain perturbed by a scatterer is replaced by the unperturbed field. It is a good approximation in the limit of weak anisotropy. Grain size distribution and grain shape effects are also excluded in both calculations since spherical grains with a same size were assumed.

In the geometric region, the grain size is much larger than the wavelength, thus the attenuation coefficient is simply characterized by the area of the geometric cross section which the grain presents to the incident wave (Stanke et al. 1984). Consequently, it is inversely proportional to the mean grain size and is independent of both the frequency and the relative inhomogeneity degree of the medium.

Based on these theoretical models discussed above, the asymptotic results of the dependence of the attenuation coefficient on the frequency f and the effective grain size $\bar{d}$ are summarized in Table 1.1. A fourth power dependence on frequency and a third power dependence on grain size of the attenuation coefficient are found in the Rayleigh region. By contrast, a second power dependence on frequency and a linear dependence on grain size dominate the scattering in the stochastic region. The

attenuation in the geometric region is determined only by the reciprocal quantity of the effective grain size and is independent of frequency.

$x = 2\pi\bar{d}/\lambda$	Type of scattering	Attenuation
$x << 1,\ \bar{d} << \lambda$	Rayleigh	$\alpha \propto \bar{d}^3 f^4$
$1 < x < 1/\xi,\ \bar{d} \approx \lambda$	Stochastic	$\alpha \propto \bar{d} f^2$
$x > 1/\xi,\ \bar{d} >> \lambda$	Geometric	$\alpha \propto \bar{d}^{-1}$

Table 1.1. Asymptotic results of the attenuation coefficient in different characteristic regions of scattering

1.2.1.2 Multiple-scattering frameworks

The single-scattering assumption and the Born approximation restrict the frequency range over which early theoretical studies of attenuation coefficient are valid. A unified theory valid in all frequency regions for evaluation of scattering-induced attenuation coefficient and phase velocity variations of elastic waves in single-phase polycrystalline media was developed by Stanke and Kino (Stanke et al. 1984). Their unified framework was based on the second-order Keller approximation proposed by Keller (Karal et al. 1964). The wave field of each grain was first expressed using the perturbation theory accurate up to the second-order term of the inhomogeneity degree ξ. Further, the mean wave field was formulated and an implicit expression for the effective wave vector of the mean plane wave was finally presented. The real part of the effective wave vector revealed the variation in phase velocity, and the attenuation coefficient due to scattering was derived from the imaginary part. Compared with the previous presented theory of Hirsekorn, effects of the grain geometry on the ultrasonic wave propagation are considered through a spatial autocorrelation function in this unified theory, avoiding artifacts that probably occur if all grains are assumed to have identical shape and size. This theory takes some degree of multiple scattering into account by formulating the scattered field in terms of the averaged wave in the whole media which has been scattered at grain boundaries. It is applicable to single-phase polycrystalline materials without limitations of crystallographic texture, grain size and shape. Even if it is only valid in the limitation of weak scattering, it stands by far as one of the most general theories for calculation of attenuation coefficient and phase velocity alteration in polycrystalline materials.

We note that formulas of this unified theory will be recalled in detail in the Section 2.1. Indeed the Rayleigh scattering, which is proportional to the volume of the scatterer, may be reduced in 2D domains. Therefore 2D formulas for attenuation coefficient need to be developed, which is important to perform relevant comparison between theoretical predictions and numerical evaluations of ultrasonic attenuation by using 2D FE simulations.

Instead of the perturbation theory based on the second-order Keller approximation in the unified theory of Stank and Kino, Weaver used the Dyson equation to account for the multiple-scattering effects (Weaver1990). He formulated the elastic Green's dyadics for the averaged response of the heterogeneous medium in terms of the one for the Voigt-average equivalent homogeneous medium and the self-energy operator. Effects of multiple-scattering were considered through the self-energy operator which described the interactions of the single particle at the observation point with the surrounding many-particle system. The Born approximation was further employed to simplify the evaluation of self-energy term. He finally presented the explicit equations for the attenuation coefficient in untextured polycrystals with cubic symmetry. Compared to the unified theory of Stanke and Kino, this theory is also valid for only weakly anisotropic materials. We remark that for all previously recalled theories, the application of the Born approximation confines their validity to frequency regions below the geometric scattering one.

1.2.1.3 Extension of the general models

Both Weaver and Stanke performed the restricted case of calculations in untextured polycrystals with equiaxial grains of cubic symmetry. Extension of these known models to untextured polycrystalline materials with elongated grains or crystallographically textured polycrystals was further investigated.

Based on the unified theory of Stanke and Kino, Ahmed et al. calculated the attenuation coefficient in untextured cubic-symmetry polycrystalline media with elongated grains (Ahmed et al. 2003). Slight effect of grain elongation on attenuation in the Rayleigh region was found for grains with the same effective volume. Afterwards, Yang et al. (Yang et al. 2011) refined the calculations about dependence of attenuation coefficient on ratios of major and minor ellipsoid axes in the Rayleigh and the stochastic scattering regions using the Weaver model. He found that the attenuation in the stochastic region was dependent only on the grain dimension in the propagation direction.

Several researchers extended also the well-known models mentioned immediately above to the case of crystallographically textured polycrystals. Hirsekorn presented the extension of her own theory to the plane longitudinal and shear waves of arbitrary propagation and polarization direction in single-phase cubic polycrystals of orthorhombic texture symmetry with weak anisotropy (Hirsekorn 1986). Analytical formulas for the attenuation coefficient and phase velocity variations were developed. Grain size distribution and grain shape variations were excluded in her theoretical model. The results were limited for the geometric scattering region. Afterwards, Ahmed et al. extended the unified Stanke-Kino model to carry out the calculation of propagation constants in the transversely isotropic medium containing cubic crystallites in which one of the cube axes was aligned in a preferred direction with the other two axes randomly oriented (Ahmed et al. 1996). Dependence of attenuation coefficients and phase velocity variations on both frequency and wave propagation direction for

longitudinal and shear waves was presented. A good overall agreement with the results of Hirsekorn (Hirsekorn 1986) for longitudinal wave attenuation was shown except in the Rayleigh-to-stochastic transition region where the latter shows the unphysical fluctuations with frequency due to the uniform grain size and shape assumption. The prediction of the shear wave attenuation coefficient was quantitatively smaller than the one of Hirsekorn. The application of the Keller approximation made his results applicable to all frequencies from the Rayleigh to the geometric scattering regions. Later on, the Weaver model was also explored to the application in crystallographically textured polycrystals with equiaxial grains (Turner 1999). The explicit expressions for the attenuation coefficient of quasi-longitudinal and quasi-shear waves were developed for the transversely isotropic polycrystalline materials containing equiaxed cubic grains with one single aligned coordinate axis. Similar results about directional dependence of ultrasonic attenuation coefficient to those of Ahmed et al. were obtained. However, the isotropic Green's function was used in the study by Ahmed et al. to describe the scattering in textured media. In fact, in the case of textured media, the choice of the isotropic Green's function might be not appropiate since the equivalent homogeneous medium was anisotropic. By contrast, Turner used the anisotropic Green's function in transverly isotropic media for modeling the ultrasonic scattering.

The Voigt averaged elastic moduli is used in both the models of Weaver and Stanke and Kino to define the equivalent homogeneous polycrystalline medium. By using the Voigt average, the unweighted average of the elastic tensor variations in an untextured medium is equal to zero. Therefore, the first order approximation term due to the elastic tensors perturbation vanishes in the unified formulation, which simplifies greatly the solution of attenuation. However, with the assumption of uniform strain, the Voigt average gives the upper bounds of the elastic moduli and thus may lead to overestimation of the ultrasonic scattering. Recently, Kube and Turner (Kube et al. 2015) demonstrated the influence of the self-consistent (SC) method of averaging elastic moduli on the evaluation of the ultrasonic attenuation based on both models of Weaver and Stanke and Kino. The covariance tensor of elastic moduli perturbations from the homogeneous equivalent medium was derived using SC averaging method and found to be considerably smaller than the one obtained by the Voigt average. The SC attenuation in this article was obtained by simply replacing the Voigt-average elastic moduli and the anisotropy coefficient in the second-order perturbation terms of the expressions for the longitudinal wave attenuation given by Weaver and Stanke and Kino with the corresponding SC quantities. Frequency dependence of the longitudinal wave attenuation coefficient deduced from the SC averaged properties was significantly smaller than that found from the Voigt average. They concluded that the attenuation predicted through the SC averaged properties provided an improved estimation compared with the Voigt attenuation, which was supported by the coherence between the SC attenuation and the experimental measurements of Zhang et al. (Zhang et al. 2004). However, as the formulas for the longitudinal wave attenuation given by the unified Stanke-Kino model are derived

by the Voigt-average properties to insure that the first-order perturbation term relevant to the averaged elastic constant deviation from the equivalent homogeneous material vanish for an untextured microstructure, we keep using this average instead of the SC average in the theoretical and numerical analyses in the present work.

1.2.1.4 Limitations

Despite all improvements discussed above, there are still several limitations associated with the analytical research on ultrasonic attenuation in polycrystalline materials:

1) The existing theoretical models are valid in the limit of weak-scattering due to the application of the Born approximation or the second-order Keller approximation. They are inapplicable to strongly anisotropic polycrystals or the case when the ultrasonic wave has been significantly attenuated due to a large propagation distance.

2) Ultrasonic attenuation in real polycrystals with complex microstructures is likely beyond the predictions of the existing theories due to a number of complicated physical issues, such as the inhomogeneous grain size distribution.

3) Effects of full multiple-scattering are difficult to account for completely with individual scatterer model or the second-order Keller approximation.

4) Application of the Born approximation in some analytical frameworks limits the validity of analytical calculations for the geometric scattering region where the grain size is considerably larger than the wavelength.

1.2.2 Experimental investigations

Besides theoretical investigations, experiment research provides an indispensable complementary approach, which is not restricted to the complexity of a polycrystalline microstructure. A variety of microstructural characterizations from ex-situ experimental measurements of ultrasonic attenuation have been carried out. On the other hand, in-situ monitoring of polycrystalline microstructural evolutions by laser-ultrasonics during thermomechanical processing is also in progress. The literature work presented here is not exhaustive and the focus is attached to the grain size measurements since one of the research objectives of this thesis is to improve the understanding of grain size effects on ultrasonic attenuation by using FE modeling. Comparison of experimental results with the existing theoretical models leads to new reflections on difficulties of experimental investigations of NDE. Then, identification of complex microstructures by inversion of ultrasonic attenuation is also briefly introduced, such as the polycrystalline titanium with high anisotropy degree.

1.2.2.1 Characterization of grain size by inversion of ultrasonic attenuation

A plenty variety of experimental investigations on characterization of grain size by inversion of ultrasonic attenuation have been undertaken. Comparison of experimental measurements with the

classical theoretical predictions is of interest to quantify the validity of the theoretical model. Diverse results were obtained.

On the one hand, coherent comparison between experimental measurement and the unified theoretical model was obtained in slightly inhomogeneous polycrystalline material. Thompson's experimental measurements of ultrasonic attenuation in a single-phase copper sample with fine and equiaxed grains provided confidence in the accuracy of the Stanke-Kino unified model in the limit of weak scattering (Thompson et al. 2008). Grain size growth in the samples of hot rolled 4mm low carbon steel sheet with low anisotropy degree was measured in real time by laser-ultrasonics (Lindh-Ulmgren et al. 2004). Attenuation coefficient was experimentally determined by the successive echoes with weaker and weaker amplitude. The grain size was determined by comparing the experimental values with analytical results predicted by the Stanke-Kino unified model. It fitted well with the values determined by optical microscopy.

On the other hand, there are also a number of experimental measurements showing incoherent comparison with the theoretical predictions. Zhang et al. (Zhang et al. 2004) also carried out the measurements of the dependence of ultrasonic attenuation on frequency and averaged grain size in copper samples. The focus of his study was given to the Rayleigh frequency region. A second power dependence on frequency and a linear dependence on the average grain size of the attenuation levels were observed, rather than a fourth power dependence on frequency and a third power dependence on averaged grain size as predicted by the Stanke-Kino unified model. Significant deviation of the metallographic-determined grain size distribution from the Poisson distribution assumed in the theoretical prediction was suspected, however, the authors made the comment that the grain size distribution could not explain completely the disagreement between the theoretical prediction and the experimental measurement.

Otherwise, experimental confirmation of the Stanke-Kino unified model in the stochastic region was also made by Zeng et al. (Zeng et al. 2010). They measured the attenuation in high purity niobium samples with a grain size in the range of 30-70 μm. Close to a second power dependence on frequency and a linear dependence on grain size of ultrasonic attenuation were observed, which was in good agreement with the stochastic scattering prediction. However, the magnitude was found to be larger than that predicted by the Stanke-Kino unified model. The sources of this difference were discussed, such as the microstructure containing fine and coarse grain bands, and the measured grain size distribution with a great probability of large grains, both of which were not considered in the theoretical model.

Concerning the in-situ measurements, Garcin et al. carried out online evaluations of heterogeneous grain growth during isothermal annealing of nickel-base superalloy using laser ultrasonics (Garcin et al. 2016). Frequency dependence of ultrasonic attenuation was experimentally measured. Then, the authors used a second power law modeling the dependence of attenuation on

grain size in the Rayleigh region, rather than a third power law given by the Stanke-Kino unified model, to quantify the grain size evolution. The results were validated by metallographic observations. We remark that this incoherence of power dependence of attenuation on grain size in the Rayleigh region between the prediction of Stanke and Kino and the experimental study by Garcin et al. is probably attributed to a high probability of large grains compared with the Poisson distribution assumed in the theoretical prediction. The study of ultrasonic wave scattering in microstructures with bimodal grain sizes presented in Section 4.2 may provide a supportive argument for this point of view.

1.2.2.2 Characterization of complex microstructures by inversion of ultrasonic attenuation

Ultrasonic attenuation in complex polycrystalline microstructures with a relatively high degree of anisotropy also attracts the investigator's interest, which is beyond the prediction of the existing classical theories.

Panetta and Thompson (Panetta et al. 1999) investigated ultrasonic attenuation in titanium alloys consisting of a particular duplex microstructure with elongated grains. The duplex microstructure was composed of randomly oriented macrograins containing colonies with crystallographically related orientations. However, the attenuation induced by crystallites within the colonies was neglected. A number of ultrasonic wave phenomena in such complex microstructure were further investigated, such as fluctuations of the backwall echoes and variations in the mean attenuation depending on propagation distance, degree of beam focusing, and nature of the reflector (Margetan et al. 1998, Thompson et al. 2008). Yang et al. studied also ultrasonic attenuation in elongated duplex titanium alloys, whose duplex microstructure consisting of elongated microtextured regions formed by much smaller crystallites with preferred orientations (Yang et al. 2012). It was shown that attenuation in such microstructure could be quantified approximately by addition of two parts: the attenuation of the microtextured regions which was considered as an ellipsoidal single crystal with the mean elastic properties, and the attenuation by crystallites inside the microtextured regions. The attenuation generated by microtextured regions was dominant for strong microtexture, and the attenuation generated by crystallites made a major contribution for a relatively weak microtexture.

1.2.2.3 Difficulties

Referring to the experimental measurements of ultrasonic scattering-induced attenuation in slight inhomogeneous polycrystalline materials, there are several difficulties for experimental confirmation of classical theoretical model: Firstly, scatterers such as voids, precipitates, bulk cracks and impurities at grain boundaries, are contained in most polycrystalline microstructures, whose contribution to the attenuation is difficult or even impossible to eliminate from the scattering at grain boundaries. Secondly, some researchers found that the grain size distribution indeed affect the ultrasonic attenuation level, such as a log-normal size distribution, which has a greater possibility of large grain size with respect to the Poisson grain size distribution employed in the theoretical prediction. Whereas,

there are still open questions related with the quantitative evaluation of grain size distribution. Thirdly, attenuation due to the dissipation, such as the dislocation damping and viscosity, can hold the quadratic dependence on frequency (Zhang et al. 2004). Accordingly, it makes the attenuation induced by scattering at grain boundaries difficult to identify. These factors lead to a number of physical issues, which are unresolved by the classical theoretical models.

Concerning the complex polycrystalline microstructure with strong inhomogeneity degree, a number of complicated experimental phenomena are observed for ultrasonic attenuation, which are beyond the classical theoretical predictions.

1.3 Evaluation of microstructural noise scattering coefficient

Since the research on ultrasonic attenuation is frequently restricted by signal-to-noise ratio for strong anisotropy material, research efforts have also been dedicated to scattered noise signals to improve inspections of microstructural evolution.

The microstructural noise scattering effectiveness in a particular spatial direction for a given angular frequency ω is usually quantified by a coefficient $\eta(\omega)$. For the analytical evaluation of $\eta(\omega)$, it is necessary to calculate the total cross section which measures the ratio of the average power flux scattered into all directions to the average intensity of the incident fields. Then, $\eta(\omega)$ is defined as the differential scattering cross section per unit volume by the differential solid angle in the given spatial direction (Margetan et al. 2005a). In comparison with ultrasonic attenuation, the research on grain-noise scattering is less well developed. Both theoretical and experimental developments for evaluation of grain-noise scattering, especially the backscattered noise signals, in polycrystalline materials will be introduced in this part. Limitations and difficulties of these two investigations will also be discussed.

1.3.1 Theoretical investigations

Two constructive methods to evaluate the scattering effectiveness in a given spatial direction are first introduced in this part, which laid the foundation for the theoretical development. The first one is based on the isolated scatterer model, *i.e.*, the single-scattering assumption, and the second one is based on the reciprocity theorem. Research on the equivalence between two models based on the Born approximation is further presented. Limitations of these two existing theoretical models are finally discussed.

1.3.1.1 The isolated scatterer model

For the current grain-noise scattering theories, models based on the single-scattering assumption is privileged. Gubernatis et al. provided the solution to the scattering of ultrasonic waves from a bounded single flaw embedded in an infinite isotropic elastic medium (Gubernatis et al. 1977a). With the assumption that the observation point was far from the scatterer, the noise scattering coefficient for an arbitrarily shaped flaw with uniform elastic stiffness constants and uniform density was formulated.

Afterwards, the authors (Gubernatis et al. 1977b) simplified the scattered field far from the scatterer using the Born approximation, with which the perturbed displacement and strain fields were replaced by the incident plane wave fields. It was concluded that the Born approximation was valid on the condition that the wavelength was an order of magnitude larger than the scatterer.

Extended theoretical investigation with single-scattering assumption and the Born approximation was conducted for the ultrasonic backscattering in duplex microstructures composed of random-oriented macrograins containing colonies with crystallographically related orientations (Han et al. 1997). Considering two main differences between a duplex microstructure and a single-phase microstructure, *i.e.*, the differences in two-point autocorrelation function of elastic tensors and in spatial correlation function, general formulas of the backscattering coefficient were developed based on the isolated scatterer model. It was then applied to the specific case of titanium alloys. It was found that the macrograins, which was considered as a homogeneous medium defined by the Voigt average of elastic properties, dominate the backscattered noise for sufficiently small colonies. However, when the colony size was comparable to the wavelength, colonies made a significant contribution to the backscattering level.

1.3.1.2 The reciprocity theorem

The reciprocity theorem dates back to the nineteenth century and is used to demonstrate the interchangeability of the source and the receiver in the electromagnetic wave and elastic wave transmission problems. The application of the reciprocity theorem to the quantitative evaluation of the elastic wave scattering coefficient originated from the research work of Auld (Auld 1979). He calculated the Rayleigh wave scattering from a surface-breaking crack in an isotropic medium based on the Born and quasi-static approximations. Then Kino adapted the scattering matrix used much in the electromagnetic theory to derive the scattering formulas for scattering of acoustic waves from flaws (Kino 1978). Amplitude of the scattered wave field was expressed both in terms of perturbations and in terms of integration over the whole flaw volume or over the boundary surface of the flaw. His contributions to the application of the reciprocity theorem to ultrasonic scattering in polycrystalline materials are fundamental.

Application of the reciprocity theorem to cracks and to bulk flaws was further demonstrated (Kino et al. 1992). Bulk flaw volume and stress intensity factor of the crack were measured based on the reciprocity theorem and results were in good agreement with the experimental measurements. Afterwards Rose gave explicit formulas for the calculation of the backscattering coefficient with the Born approximation in single-phase and untextured polycrystalline materials with cubic symmetry based on the reciprocity theorem (Rose 1992). Influence of grain elongation on ultrasonic backscattering effectiveness was also investigated based on the reciprocity theorem with the single-scattering approximation (Ahmed et al. 1995).

1.3.1.3 Equivalence between the reciprocity theorem and the isolated scatterer model

The equivalence between the isolated scatterer model and the reciprocity theorem for the computation of microstructural noise scattering coefficient was demonstrated by Rose (Rose 1992) and Margetan et al. (Margetan et al. 2005a). They evaluated the parameters using the weak-scattering Born approximation and applying the unweighted Voigt average to define the effective elastic stiffness of the medium in the presence of scatterers. Based on the equivalence, the general expression for the backscattering coefficient in polycrystalline materials was presented. It was valid in the limit of weak-scattering by individual crystallite since the Born approximation and the single-scattering assumption were made. Analytical formulas of the backscattering coefficient for untextured polycrystals with cubic or hexagonal symmetry were given.

It is worth to remark that multiple-scattering effects are neglected in the isolated scatterer model based on which the polycrystals are modeled as a collection of individual scatters. By contrast, some degree of multiple-scattering effects can be considered by the model based on the reciprocity theorem if the scattered field is evaluated using a more complicated approximation, such as the second-order Keller approximation (Karal et al. 1964, Stanke et al. 1984). Further investigations are therefore needed for the consideration of multiple-scattering effects.

1.3.1.4 Limitations

Since the Born approximation and the single-scattering assumption have been applied in the theoretical evaluation of both ultrasonic attenuation and backscattering, the identical limitations for the analytical investigation of ultrasonic backscattering to the ultrasonic attenuation have been found. In the absence of multiple-scattering consideration, the existing theories are restricted to weakly-scattering materials and to frequency ranges below the geometric scattering region. Due to these limitations, the theoretical analysis for ultrasonic backscattering is confined to the early time portion of the grain-noise scattered signals such that the incident wave will not be significantly attenuated (Han et al. 1997).

1.3.2 Experimental investigations

As for the experimental investigation of microstructural noise scattering, most of efforts have been devoted to the study of backscattered microstructural noise because of the noticeably feasibility. A mathematical model based on the single-scattering assumption for the experimental evaluation of ultrasonic backscattering is firstly introduced, and its numerous applications to both simple and complex polycrystals are recalled. Evidence for the multiple-scattering effects found in the experimental measurement is presented, which proves the necessity of a more complete model including multiple scattering. Limitations of the experimental investigation of microstructural noise scattering are discussed finally.

1.3.2.1 Experimental quantification based on single scattering model

Quantitative study of the time-series backscattered noise levels is essential to make predictions for microstructural features. A mathematical model for the experimental evaluation of backscattering coefficient in ultrasonic narrowband tone burst inspections is initiated by the work of Margetan and Thompson (Margetan et al. 1991, Margetan et al. 1993, Margetan et al. 1994). It was based on the previously presented isolated scatterer model, assuming that the backscattered noise signals observed at a given transducer position was an incoherent superposition of echoes from individual grains. The formulas expressed the absolute backscattered noise level observed in an ultrasonic inspection in terms of the parameters of the measurement system and a factor describing the contribution of polycrystalline microstructure to the backscattered noise. This factor was referred as Figure-of-Merit (FOM) and frequency-dependent, which was the square root of the backscattering coefficient derived in the article of Rose (Rose 1992). In addition, a version of the model applicable to a broadband ultrasonic signal was also derived, using the incoherent superposition assumption to obtain an expression for the root-mean-squared (rms) spectral components of the noise on a finite time interval. The model was applicable to weakly-scattering perfect polycrystalline materials without defects.

Two distinct practical applications of this backscattered noise model were presented. Firstly, the time dependence of rms average of the backscattered noise echoes was analyzed to deduce the FOM (Margetan et al. 1994). Conversely, with the FOM determined first, the model was used to predict the absolute noise levels that would be observed in ultrasonic inspections (Margetan et al. 1995). The predictions reproduced the measured backscattered noise echoes with reasonable accuracy.

Experimental investigations in relatively simple polycrystals were conducted using this backscattered noise model (Thompson et al. 2008). The model was firstly validated in the weakly anisotropic material, a fine-grained, single-phase, equiaxed and untextured copper sample. Excellent coherence between the measured noise FOM and the predicted FOM deduced independently from knowledge of the microstructure was observed, which demonstrated the accuracy of the mathematical model in weak-scattering limit. Given this validation, this backscattered noise model was then applied for determining the elastic constants of the single crystal in nickel-based superalloys with the grain size information obtained from optical observation.

Furthermore, a number of complex wave propagation phenomena were also observed in titanium alloys with elongated and duplex microstructure, such as a significant dependence of the noise level on the wave propagation direction (Margetan et al. 1995) and strong fluctuations in observed noise signals (Thompson et al. 2008). They were beyond the prediction of the classical theories. Additional analytical interpretation of these phenomena by simple 2D scalar models was presented in the same work and the authors believed that these complex phenomena were associated with grain-to-grain velocity variations.

1.3.2.2 Evidence of multiple scattering

A series of experiments have been undertaken to search for the evidence for multiple scattering in the backscattered ultrasonic grain noise (Margetan et al. 2005b, Thompson et al. 2008):

-) In pulse-echo measurements within nickel-base superalloys, the effect of multiple scattering presumably led to discrepancies between the experimental measurements and the analytical predictions of the time-dependent rms noise level at later times. Reinforce of this effect with grain size and the inspection frequency was observed.

-) In pitch-catch inspections, the noise signals arising from scattering by grains beyond the beam overlap region provided a strong evidence for the existence of multiple scattering.

Their investigations suggest that a more relevant approach including multiple scattering is required to correctly describe and quantify ultrasonic phenomena in real polycrystalline microstructures.

1.3.2.3 Limitations

The previously presented backscattered noise model for experimental measurements of backscattering coefficient developed by Margetan et al. is not applicable to the material with a complex microstructure or strong anisotropy because of the single scattering assumption. Significant modulations in amplitude and phase of an ultrasonic beam observed in the duplex titanium alloys with elongated grains provides an evidence for the argument above (Thompson et al. 2008). Besides, multiple-scattering mechanism is not included in the model.

1.4 FE modeling of ultrasonic wave scattering

Confronting the limitations and difficulties in the present theoretical studies, two approaches are the alternative ways to improve the understanding of the physical mechanism of elastic wave scattering: semi-analytical methods and numerical modeling. Analytical approximations are generally used for semi-analytical approaches, which allow deriving mathematical solutions (Lhémery et al. 2000). By contrast, without analytical approximations, numerical modeling is an effective tool to predict ultrasonic signals by appropriate finite discretization analysis. A variety of numerical modeling methods have been used for simulating the wave propagation in heterogeneous media. On the one hand we can cite the finite difference (FD) method (Alford et al. 1974), the FD pesudospectral method (Fornberg 1988), the boundary element method (Liu et al. 2001), and the elastodynamic finite integration technique (EFIT) (a FD time domain scheme based on an integral formulation of the governing equations of elastodynamics (Fellinger et al. 1995, Schubert et al. 2001)). Each of them is applicable to wave propagation simulation in certain heterogeneous media, however, none is suitable to polycrystalline media.

On the other hand, the FE method capable of using any unstructured meshes allows a more accurate access to complex geometries and heterogeneities in a very simple way. Its variational framework also offers powerful enrichments to achieve high quality required by wave modeling (Komatitich et al. 1998, Tie et al. 2006). Recently, FE method has been adopted to the computation for elastic wave propagation in polycrystalline materials. In contrast to the analytical method, FE simulations allow to grasp the complex physical process of wave propagation in polycrystals, including the effects of multiple-scattering (Shahjahan et al. 2014, Van Pamel et al. 2015). It is applicable to quantify the scattering effectiveness from grain boundaries by modeling the perfect polycrystalline microstructure, free of the defects such as voids, cracks. Besides, progress in the Electron Backscatter Diffraction (EBSD) technique makes it possible to obtain complex realistic microstructures for numerical modeling. Its accuracy and versatility in modifying the microstructural model make the FE modeling a promising approach for further developments of nondestructive inspection.

In this part, several FE codes and examples of their application to model ultrasonic scattering in polycrystals are presented. Their respective theoretical frameworks and results are summarized. Difficulties and prospects for the FE modeling of elastic wave scattering are discussed to end this part.

1.4.1 FE codes and applications

The commercial package ABAQUS is usually used to perform the FE simulations for elastic wave propagation in polycrystalline microstructures. Ghoshal et al. (2009) conducted FE modeling of ultrasonic wave scattering for equiaxed, untextured polycrystalline materials: weakly-scattering aluminum, a moderately-scattering fictitious material, and a strongly-scattering copper (Ghoshal et al. 2009). Their research focused on the grain-scale description of the polycrystalline microstructure. Their FE modeling used Voronoi polycrystal model composed of convex polygons in two dimensions (Kumar et al. 1992). In the 3D case, they proposed a pseudo-3D model constructed through extruding a 2D Voronoi polycrystal by a depth comparable to the element size, which facilitated the use of a 3D crystallographic orientation. Normal grain size distribution was generated. Ultrasonic attenuation of the longitudinal wave was measured for a wide range of frequencies covering the Rayleigh-to-stochastic transition and stochastic scattering regions. By comparison with the previously presented Weaver's model, good agreement between the numerically evaluated attenuation and the theoretical model was observed in low frequency region for all the materials, which proved the capability of FE modeling to accurately simulate the ultrasonic scattering in polycrystalline materials. Besides, it was found that the numerically measured attenuation for strongly-scattering material in the high frequency region did not fit well with the theoretical prediction, which showed the limitation of the established theory.

However, FE modeling is time and memory consuming due to an exact representation of each crystallite leading to very small discretization size in both space and time domains. Several FE codes have emerged recently to satisfy various requirements, such as the efficiency of the calculation, the modeling of anisotropy media with arbitrary shaped defects, and the adaptive remeshing capability, etc.

1.4.1.1 FE code using the graphical processing unit (GPU)

To improve the calculation speed, an approach to perform explicit time domain FE simulations of elastodynamic problems using the GPU was developed (Huthwaite 2014). Using a new aligned mesh partitioner which aimed to arrange the subdivisions of the mesh in a more optimal manner, it was demonstrated to be more efficient than the commercial software ABAQUS. Afterwards, this FE code was applied to simulate the ultrasonic scattering of longitudinal waves in polycrystalline materials for both 2D and 3D cases (Van Pamel et al. 2015). The material was assumed to be a single-phase, untextured medium with equiaxed grains of cubic symmetry and a relatively strong anisotropy degree. Voronoi algorithms were used to numerically generate the 2D and 3D morphologies. Different from the pseudo-3D model of Ghoshal et al. (2009), convex polyhedrons in 3D spaces were constructed using 3D Voronoi tessellation, that were geometrically similar to a naturally occurring polycrystalline microstructure. Frequency dependence of ultrasonic attenuation coefficient and phase velocities were analyzed and further compared with the Stanke-Kino unified scattering theory. Good agreement between the numerically evaluated attenuation and the established theory was shown in the transition region from the Rayleigh to stochastic scattering region for both 2D and 3D models. However, it was found that 2D model reduced the scattering mechanism in the Rayleigh region because the Rayleigh scattering is a 3D phenomenon closely linked to the volume of grains.

1.4.1.2 The ATHENA FE code

The FE code called ATHENA was developed by Electricity of France (EDF) in collaboration with The French Institute for Research in Computer Science and Automation (INRIA) dedicated to simulating wave propagation in anisotropic and heterogeneous media with defects of arbitrary shape and orientation (Chassignole et al. 2009, Dupond et al. 2011). It was based on a new family of mixed FE method, constructing the formulation expressed in terms of velocity and stress fields and not the traditional displacement field (Bécache et al. 2000, Bécache et al. 2002, Chassignole et al. 2009). It was implemented by a quasi-explicit time discretization scheme through mass lumping. The fictitious domain method was used, extending the calculation zone to a domain of simple geometry that ignores the defect. It made the mesh of the defect independent of the structured mesh of the calculation zone, thus allowing the compatibility of the structured mesh computation rapidity with the capability of modeling the arbitrary shaped defects.

The 2D version of the ATHENA code was first applied to model the ultrasonic wave propagation in austenitic stainless steel welds (Chassignole et al. 2009, Chassignole et al. 2010). The motivation of

FE modeling was to explain and predict quantitatively the complex features of wave propagation in welds with strong anisotropy varying continuously from one area to another. In the studied case, the inspection plane was a plane of symmetry of the orthotropic material, which made the 2D simplification justified. The early version of the FE code ATHENA 2D did not take into account grain scattering, and thereby underestimated the ultrasonic echo amplitude losses (Chassignole et al. 2010). Afterwards, a model considering the scattering-induced attenuation was developed and was further validated through comparison with experimental configurations with austenitic stainless steel welds (Chassignole et al. 2009). The ability of this code to reproduce multiple wave scattering features in a coarse-grain microstructure was evaluated (Shahjahan et al. 2014). The coherent backscattering intensity was analyzed, which represented the interference between scattering waves following different paths.

Because of the advance in computing processor speed and memory, the ATHENA 3D FE code was developed (Rose et al. 2014). Based on the fictitious domain method, the calculation domain was described using a regular 3D mesh, while the defect of complex geometry was discretized using a separate 2D mesh. The capability of ATHENA 3D to reproduce the ultrasonic wave propagation and the interaction between the wave and the defect was demonstrated using several test configurations in isotropic and homogeneous media. Further validation tests and comparisons with experimental data for heterogeneous and anisotropic media are in progress (Rose et al. 2014, Shahjahan et al. 2014).

1.4.1.3 FE code based on adaptive time discontinuous Galerkin method

An in-house FE code named OOFE dedicated to the simulation of elastic wave propagation was developed based on an adaptive remeshing method (Tie et al. 2006, Tie et al. 2010). It was defined within the framework of the space-time discontinuous Galerkin method, considering the whole space-time domain by subdividing it into space-time slabs (Hughes et al. 1988, Li et al. 1998, Tie et al. 2006). Compared with the classical Newmark scheme, it increased the computational accuracy and was particularly suitable for dealing with adaptive time-varying meshes, because the discontinuities of the unknown fields were directly involved and treated in the weak formulation. The unstructured mesh improved the discretization of complex geometry. Nevertheless, the method leading to an implicit unconditionally stable solver is more time and memory consuming than explicit solvers.

Furthermore, the OOFE code was applied to the simulation of elastic wave propagation in plate and shells under moving loads were presented and the powerful capability of the adaptive remeshing method to capture the shock wave fronts was demonstrated (Tie et al. 2003). Afterwards, this code was used to provide the quantitative analyses and predictions for the elastic shock waves in hexagonal honeycomb sandwich panels for the application to space launcher (Grede et al. 2006, Tie et al. 2005).

The application of such dynamic solver to FE modeling of the elastic wave propagation in crystalline materials was researched (Thebault 2009, Tie et al. 2010). Significant effects of

crystallographic orientations on the ultrasonic attenuation in the single crystal were evaluated quantitatively. Numerical investigations on ultrasonic wave propagation in the bicrystal showed that the misorientations between crystals influence significantly the wave reflection and transmission on the grain boundary. Preliminary research on grain size effects on ultrasonic attenuation in polycrystalline materials comprising single-size, hexagonal grains was carried out.

1.4.2 Limitations and perspectives

Despite the successful application of FE modeling to the elastic wave scattering in polycrystalline materials, the calculation in the geometric scattering region is restricted by the induced computational cost, as a result of numerically discretizing polycrystals with meshes whose size is quite small compared to the wavelength.

Most of recent study for FE modeling of elastic wave scattering uses the 2D polycrystalline model which leads to several simplifications (Van Pamel et al. 2015). It correctly represents neither the grain size distribution of a 3D material nor 3D propagation mechanisms quite different from those in 2D cases. Furthermore, in 2D and 3D cases, wave propagation are very different. In addition, the Rayleigh scattering phenomenon is not fully reproduced because it is proportional to the grain volume. Thus, the fourth power law dependence of the ultrasonic attenuation on frequency has been reduced. Further progress in the 3D simulations for elastic wave propagation is urgently needed.

Quantitative evaluation of microstructural noise scattering coefficient considering the full effects of multiple-scattering by using the FE modeling is of interest. Compared with the theoretical approach, the potential ability of FE modeling to reproduce complex real polycrystalline microstructures in a more flexible manner is attractive.

1.5 Conclusions

This chapter addresses the recent investigations of elastic wave scattering in polycrystalline materials for the achievements of the NDE, referring to some classical theories, experimental advancements and FE numerical modeling developments.

The classical theories for evaluation of ultrasonic attenuation and backscattering have been recalled, such as the Stanke-Kino unified model and the Weaver's model for the quantification of the ultrasonic attenuation, the isolated scatterer model and the application of the reciprocity theorem to the measurement of ultrasonic noise scattering. It is indicated that the theoretical development has been held back by difficulties in finding a mathematical description and modeling of the complex polycrystalline microstructure and of the sophisticated physical mechanisms including multiple scattering. With regard to the experimental investigation, the validation of the classical theories for wave scattering in simple polycrystals has been presented, and a number of unresolved physical issues of wave scattering in complex polycrystals have been discussed. Because of its accuracy and

flexibility, the FE modeling is considered as a promising tool to further improve the inspections of NDE. Several FE codes developed to meet various modeling and calculation needs are presented, and the current progress in the quantification of microstructural features using elastic wave scattering characteristics based on these codes is discussed.

Chapter 2

Theoretical and numerical evaluations of the ultrasonic wave scattering in polycrystals

In this chapter, theoretical and numerical evaluations of ultrasonic wave scattering in polycrystals are considered. Using the Born approximation and the single scattering assumption, analytical formulas of ultrasonic attenuation and backscattered noises are presented for single-phase, untextured polycrystals composed of equiaxed grains with cubic symmetry and unimodal size distribution. On the other hand numerical evaluation approaches without any restrictive assumption are proposed.

Concerning the ultrasonic attenuation, general formulas for ultrasonic attenuation coefficient α in polycrystalline materials based on the Stanke-Kino unified model are presented. 3D analytical formulas of the longitudinal wave attenuation in the single-phase, untextured polycrystalline microstructure composed of equiaxed grains with cubic symmetry are recalled. Two new contributions are made within the framework of the Stanke-Kino unified model: Firstly, explicit formulas for two components of the longitudinal wave attenuation, *i.e.* the longitudinal-to-longitudinal and the longitudinal-to-shear scattering-induced attenuation, are developed. They are based on the Born approximation and on an additional assumption stating that the polarization displacement vector of the quasi-longitudinal wave in a slightly inhomogeneous medium remains parallel to the wave propagation direction (Section 2.1.2). Secondly, 2D formulas for the attenuation coefficient in single-phase and untextured polycrystals composed of equiaxed grains with cubic symmetry are developed and make possible comparisons between theoretical predictions and 2D numerical results (Section 2.1.3).

Concerning the grain-scattered noises, 3D analytical formulas for microstructural noise scattering coefficient η are recalled by considering the equivalence between the amplitudes of scattered noise signals calculated by two different methods: the one based on the reciprocity theorem and the other based on far-field analysis of the isolated scatterer model. The key assumption is weak scattering so that the Born approximation can be applied. As an important contribution, theoretical measure of the microstructural noise scattering coefficient in the 2D space is investigated: Firstly, far-field amplitude of the scattered noise signals is developed based on the isolated scatterer model (Section 2.2.3.3). Second, a coefficient of proportionality depending on the spatial dimension is determined based on the equivalence of the reciprocity theorem and the isolated scatter model under the Born approximation and the single-scattering assumption (Section 2.2.4.1). Thirdly, 2D theoretical formulas for the noise backscattering coefficient in single-phase and untextured polycrystals with equiaxed grains are developed (Section 2.2.4.3). As one of the most important results of the present work, a numerical evaluation approach and the corresponding expressions of the ultrasonic noise scattering coefficient

using FE modeling in both 2D and 3D cases are proposed within the framework of the reciprocity theorem (Section 2.2.4.2).

2.1 Theoretical evaluation of ultrasonic attenuation by the Keller perturbation series

For theoretical evaluation of ultrasonic attenuation, two kinds of approximations are made. The first one is the second-order Keller approximation (Karal et al. 1964, Stanke et al. 1984). It applies the perturbation theory to express the wave field in each anisotropic grain accurately up to the second order of the inhomogeneity degree ξ of the medium. Then the average field of the whole medium is formulated accurately up to the second order of ξ. The second one is the Born aproximation, *i.e.* the actual field in each grain is replaced by the unperturbed field in the equivalent homogeneous medium. Both approximations are expected to be relevant under the condition of weak scattering, *i.e.* $\xi << 1$.

In this thesis, with regard to the material heterogeneity, the following hypotheses are postulated to obtain the general formulas for both attnuation and backscattering coefficients:

1) Concerning the degree of anisotropy, polycrystals are assumed to be weakly anisotropic, which means that deviations of the elastic constants from their average properties is much smaller than the latters.
2) Concerning the crystallographic texture, polycrystals are assumed to be single-phase without density variation and the crystallographic orientations of grains are randomly distributed.
3) Concerning the morphologic texture, the grains are approximately equiaxed with a Poisson grain size distribution and have a cubic symmetry.

For convenience, we name the above hypothesis as “assumptions on the material heterogeneity”. These assumptions ensure the validaty of the following conditions:

4) The media are macroscopically homogeneous, i.e. the average equivalent medium is homogeneous.
5) The elastic constant variation and the characteristic function of each grain vary independently.
6) The grain-to-grain deviation in the elastic constants varies independently.

These conditions allow the simplification for the average of the two-point autocorrelation function of elastic tensors, which is thereby approximated by the elastic constants of single crystallite and the spatial autocorrelation function.

2.1.1 Formulas for ultrasonic attenuation in the general case

Considering an elastic medium occupying a region Ω bounded by a surface $\partial\Omega$ and defined by a position-dependent elastic stiffness tensor $\boldsymbol{C}(\boldsymbol{x})$ and a position-independent density field ρ. The spatial dimension of Ω is N_{dim}, $N_{dim} = 3$ in the 3D case while $N_{dim} = 2$ in the 2D case. The time harmonic elastic wave equation without any source term inside Ω can be written as:

$$\mathbf{Div}_x \boldsymbol{\sigma}(\boldsymbol{x}) + \rho\omega^2 \boldsymbol{u}(\boldsymbol{x}) = 0 \tag{2.1}$$

where $\boldsymbol{u}(\boldsymbol{x})$ denotes the Fourier transform of the time-varying displacement field $\boldsymbol{u}(\boldsymbol{x},t)$ in frequency domain, $\mathbf{Div}_x$ denotes the usual divergence operator of a second order tensor with respect to the position $\boldsymbol{x}$, ω denotes the angular frequency, $\boldsymbol{\sigma}(\boldsymbol{x})$ is the stress tensor and defined by:

$$\boldsymbol{\sigma}(\boldsymbol{x}) = \boldsymbol{C}(\boldsymbol{x}) : \boldsymbol{\varepsilon}(\boldsymbol{x}) \tag{2.2}$$

where $\boldsymbol{\varepsilon}(\boldsymbol{x}) = 1/2(\nabla_x \boldsymbol{u}(\boldsymbol{x}) + \nabla_x^T \boldsymbol{u}(\boldsymbol{x}))$ is the strain tensor. For ease of notation, we keep using $\boldsymbol{\sigma}(\boldsymbol{x})$, $\boldsymbol{\varepsilon}(\boldsymbol{x})$ to denote the Fourier transform of $\boldsymbol{\sigma}(\boldsymbol{x}, t)$, $\boldsymbol{\varepsilon}(\boldsymbol{x}, t)$ in frequency domain. Herein, tensors and vectors are denoted using bold letters.

By defining a position-dependent linear operator $L(\boldsymbol{x})$, (2.1) can be put into the following generic form:

$$L(\boldsymbol{x})\, \boldsymbol{u}(\boldsymbol{x}) = 0 \tag{2.3}$$

This operator is denoted by L^0 in the equivalent homogeneous medium of the studied heterogeneous medium. Under the assumptions on the material heterogeity, L^0 is independent of $\boldsymbol{x}$, invertible and differ slightly from $L(\boldsymbol{x})$. Then it is assumed that $L(\boldsymbol{x})$ can be developed from L^0 with respect to the inhomogeneity degree ξ (Karal et al. 1964):

$$L(\boldsymbol{x}) = L^0 - \xi L_1(\boldsymbol{x}) - \xi^2 L_2(\boldsymbol{x}) - o(\xi^3) \tag{2.4}$$

Here $L_1(\boldsymbol{x})$ and $L_2(\boldsymbol{x})$ are perturbing operators characterizing inhomogeneity effects.

The objective is to find the solution of the average displacement field $\langle \boldsymbol{u}(\boldsymbol{x}) \rangle$ with $\langle \cdot \rangle$ denoting an average over ensembles. Taking the second-order Keller approximation (see Appendix A) and omitting the $o(\xi^3)$ term, an explicit equation for $\langle \boldsymbol{u}(\boldsymbol{x}) \rangle$ accurate to ξ^2 is written as follows (Karal et al. 1964, Stanke et al. 1984):

$$\left(L^0 - \xi \langle L_1(\boldsymbol{x}) \rangle - \xi^2 \left(\langle L_1(\boldsymbol{x}) (L^0)^{-1} L_1(\boldsymbol{x}) \rangle - \langle L_1(\boldsymbol{x}) \rangle (L^0)^{-1} \langle L_1(\boldsymbol{x}) \rangle + \langle L_2(\boldsymbol{x}) \rangle \right) \right) \langle \boldsymbol{u}(\boldsymbol{x}) \rangle = 0 \tag{2.5}$$

In the present work the only perturbation is the deviations of the local elastic tensors from the equivalent homogeneous medium: $\delta \boldsymbol{C}(\boldsymbol{x}) = \boldsymbol{C}(\boldsymbol{x}) - \boldsymbol{C}^0$, with $\boldsymbol{C}^0$ denotes as the elastic stiffness tensor of the equivalent homogeneous material. Therefore the operators L^0, $L_1(\boldsymbol{x})$ and $L_2(\boldsymbol{x})$ are defined as:

$$\begin{cases} L^0 \boldsymbol{u}(\boldsymbol{x}) = \mathbf{Div}_x \left(\boldsymbol{C}^0 : \boldsymbol{\varepsilon}\left(\boldsymbol{u}(\boldsymbol{x}) \right) \right) + \rho^0 \omega^2 \boldsymbol{u}(\boldsymbol{x}) \\ \xi L_1(\boldsymbol{x}) \boldsymbol{u}(\boldsymbol{x}) = -\mathbf{Div}_x \left(\delta \boldsymbol{C}(\boldsymbol{x}) : \boldsymbol{\varepsilon}\left(\boldsymbol{u}(\boldsymbol{x}) \right) \right) \\ \xi^n L_n(\boldsymbol{x}) \boldsymbol{u}(\boldsymbol{x}) = 0, \; n > 1 \end{cases} \tag{2.6}$$

By the substitution of (2.6) into (2.5), it is found that the average displacement solution $\langle \boldsymbol{u}(\boldsymbol{x}) \rangle$ satisfies the following equation:

$$\begin{aligned} 0 = {} & \rho^0\omega^2\langle \boldsymbol{u}(\boldsymbol{x})\rangle + \mathbf{Div}_x\left(\boldsymbol{C}^0 \colon \boldsymbol{\varepsilon}\left(\langle \boldsymbol{u}(\boldsymbol{x})\rangle\right)\right) + \mathbf{Div}_x\left(\langle \delta\boldsymbol{C}(\boldsymbol{x})\rangle : \boldsymbol{\varepsilon}\left(\langle \boldsymbol{u}(\boldsymbol{x})\rangle\right)\right) \\ & -\left\langle \mathbf{Div}_x\left(\delta\boldsymbol{C}(\boldsymbol{x}) : \int \nabla_x \boldsymbol{G}^T(\boldsymbol{x}';\boldsymbol{x}) : \mathbf{Div}_{x'}\left(\delta\boldsymbol{C}(\boldsymbol{x}') : \boldsymbol{\varepsilon}\left(\langle \boldsymbol{u}(\boldsymbol{x}')\rangle\right)\right) dV'\right)\right\rangle \\ & +\mathbf{Div}_x\left(\langle \delta\boldsymbol{C}(\boldsymbol{x})\rangle : \int \nabla_x \boldsymbol{G}^T(\boldsymbol{x}';\boldsymbol{x}) : \mathbf{Div}_{x'}\left(\langle \delta\boldsymbol{C}(\boldsymbol{x}')\rangle : \boldsymbol{\varepsilon}\left(\langle \boldsymbol{u}(\boldsymbol{x}')\rangle\right)\right) dV'\right) \end{aligned} \tag{2.7}$$

where the kernel of the operator $(L^0)^{-1}$ appearing in (2.5) is expressed as an integral in terms of the Green's function tensor $\boldsymbol{G}(\boldsymbol{x}';\boldsymbol{x})$. We recall that $\boldsymbol{G}(\boldsymbol{x}';\boldsymbol{x})$ in an infinite homogeneous region can be written as follows:

$$\boldsymbol{G}(\boldsymbol{x}';\boldsymbol{x}) = \sum_{m=1,\cdots,N_{dim}} \boldsymbol{e}_m \otimes \boldsymbol{g}_m(\boldsymbol{x}';\boldsymbol{x}) \tag{2.8}$$

where $(\boldsymbol{e}_m)_{m=1,\cdots,N_{dim}}$ is the global Cartesian basis, $\otimes$ denotes the tensor product and $\boldsymbol{g}_m(\boldsymbol{x}';\boldsymbol{x})$ is the solution of the following wave problem in the equivalent homogeneous medium with a Dirac delta source term applied at point $\boldsymbol{x}'$ in the direction $\boldsymbol{e}_m$:

$$\mathbf{Div}_x\left(\boldsymbol{C}^0 : \boldsymbol{\varepsilon}(\boldsymbol{g}_m(\boldsymbol{x}';\boldsymbol{x}))\right) + \rho^0\omega^2\boldsymbol{g}_m(\boldsymbol{x}';\boldsymbol{x}) + \delta(\boldsymbol{x}-\boldsymbol{x}')\boldsymbol{e}_m = 0 \tag{2.9}$$

The expression (2.7) for the average displacement field is valid for all frequencies based on the fundamental assumption that $\xi << 1$. It is accurate to the second order of ξ, and $\langle \boldsymbol{u}(\boldsymbol{x})\rangle$ is a second order approximation to $\boldsymbol{u}(\boldsymbol{x})$. The terms on the right-hand side of (2.7) can be easy to interpret. The first and second terms give the zeroth-order approximation $\boldsymbol{u}^0$ of $\langle \boldsymbol{u}(\boldsymbol{x})\rangle$, which is the solution of the following wave equation in the equivalent homogeneous medium:

$$\mathbf{Div}_x(\boldsymbol{C}^0 \colon \boldsymbol{\varepsilon}(\boldsymbol{u}^0)) + \rho^0\omega^2\boldsymbol{u}^0 = 0 \tag{2.10}$$

The third term is involved with the first-order perturbation of the actual field due to the scattering. The last two terms are associated with the second-order approximation, accounting for some degree of multiple-scattering since the interactions between two arbitrary points are considered and the propagation constant is solved by the mean plane wave which is itself attenuated by the scattering (Stanke et al. 1984).

It is assumed that the deviation of elastic tensor $\delta\boldsymbol{C}(\boldsymbol{x})$ in each grain is constant and is denoted as $\delta\boldsymbol{C}^I$ for the I^{th} grain g^I, and γ^I denotes its characteristic function, defined to be one inside g^I and zero elsewhere. It is obvious that we have $\delta\boldsymbol{C}(\boldsymbol{x}) = \sum_I \delta\boldsymbol{C}^I\gamma^I(\boldsymbol{x})$. One-point average $\langle \delta\boldsymbol{C}\rangle$ is affected only by the crystallographic texture of the whole medium and is equal to zero only if the medium is untextured. Due to single-phase assumption, it is obvious that $\langle \delta\boldsymbol{C}^I\rangle = \langle \delta\boldsymbol{C}^I\rangle_\Theta$ with Θ standing for the average over all crystallographic orientations. $\langle \delta\boldsymbol{C}^I\rangle_\Theta$ is grain independent and will be denoted in the following as $\langle \delta\boldsymbol{C}^g\rangle_\Theta$. Otherwise, under the assumption that the elastic constant variation and the characteristic function vary independently, the average two-point correlation function of elastic stiffness tensors $\langle \delta\boldsymbol{C}(\boldsymbol{x}) \otimes \delta\boldsymbol{C}(\boldsymbol{x}')\rangle$ can be developed in the following way:

$$\langle \delta\boldsymbol{C}(\boldsymbol{x}) \otimes \delta\boldsymbol{C}(\boldsymbol{x}')\rangle = \sum_I \sum_J \langle \delta\boldsymbol{C}^I \otimes \delta\boldsymbol{C}^J\rangle_\Theta \langle \gamma^I(\boldsymbol{x})\gamma^J(\boldsymbol{x}')\rangle \tag{2.11}$$

To further simplify (2.11), it is assumed that $\langle \delta \boldsymbol{C}^I \otimes \delta \boldsymbol{C}^J \rangle_\Theta = 0$ when $I \neq J$ based on the hypothesis that the grain-to-grain deviation in the elastic constants varies independently. On the other hand, we recall that the spatial correlation function of two points $\boldsymbol{x}$ and $\boldsymbol{x}'$ describing the possibility that they are in the same grain g^I, where $\boldsymbol{r} = \boldsymbol{x} - \boldsymbol{x}'$, is denoted as:

$$W(\boldsymbol{r}) = \sum\nolimits_I \langle \gamma^I(\boldsymbol{x}) \gamma^I(\boldsymbol{x}') \rangle \tag{2.12}$$

In other words, $1 - W(\boldsymbol{r})$ quantifies the possibility that two points $\boldsymbol{x}$ and $\boldsymbol{x}'$ are in two different grains *I* and *J*. Due to the single phase assumption, it is obvious that $\langle \delta \boldsymbol{C}^I \otimes \delta \boldsymbol{C}^J \rangle_\Theta = \langle \delta \boldsymbol{C}^g \otimes \delta \boldsymbol{C}^g \rangle_\Theta$. By applying all above presented hypotheses, (2.11) can be written as:

$$\langle \delta \boldsymbol{C}(\boldsymbol{x}) \otimes \delta \boldsymbol{C}(\boldsymbol{x}') \rangle = W(\boldsymbol{r}) \langle \delta \boldsymbol{C}^g \otimes \delta \boldsymbol{C}^g \rangle_\Theta + \big(1 - W(\boldsymbol{r})\big) \langle \delta \boldsymbol{C}^g \rangle_\Theta \otimes \langle \delta \boldsymbol{C}^g \rangle_\Theta \tag{2.13}$$

Finally (2.7) is rewritten as follows:

$$\begin{aligned} 0 = {} & \rho^0 \omega^2 \langle \boldsymbol{u}(\boldsymbol{x}) \rangle + \mathbf{Div}_x \Big(\boldsymbol{C}^0 : \boldsymbol{\varepsilon}\big(\langle \boldsymbol{u}(\boldsymbol{x}) \rangle \big) \Big) + \mathbf{Div}_x \Big(\langle \delta \boldsymbol{C}^g \rangle_\Theta : \boldsymbol{\varepsilon}\big(\langle \boldsymbol{u}(\boldsymbol{x}) \rangle \big) \Big) \\ & - \Big(\langle \delta \boldsymbol{C}^g \otimes \delta \boldsymbol{C}^g \rangle_\Theta - \langle \delta \boldsymbol{C}^g \rangle_\Theta \otimes \langle \delta \boldsymbol{C}^g \rangle_\Theta \Big) : \boldsymbol{Q}(\boldsymbol{x}) \end{aligned} \tag{2.14}$$

In the last term on the right-hand side of (2.14), "$:$" denotes the contraction operator between an 8th-order tensor and a 7th-order tensor and is defined by $(\boldsymbol{A} : \boldsymbol{B})_i = A_{ijklm'n'p'q'} B_{jklm'n'p'q'}$ using Einstein's summation convention, and $\boldsymbol{Q}$ is a 7th-order tensor, expressed in the index notation as follows:

$$Q_{jklm'n'p'q'}(\boldsymbol{x}) = \Big(\int G^T_{km',l}(\boldsymbol{x}'; \boldsymbol{x}) \big(W(\boldsymbol{x} - \boldsymbol{x}') \varepsilon_{p'q'} \big)_{,n'} dV' \Big)_{,j} \tag{2.15}$$

where the comma notation is adopted for differentiation.

To solve the problem (2.14), It is assumed that the average field of the heterogeneous medium has the form of a plane wave, expressed as follows:

$$\langle \boldsymbol{u}(\boldsymbol{x}) \rangle = \boldsymbol{U} \exp(ik \hat{\boldsymbol{k}} \cdot \boldsymbol{x}) \tag{2.16}$$

where $\hat{\boldsymbol{k}}$ is a unit vector defining the propagation direction, $\boldsymbol{U}$ specifies the polarization vector of the displacement field. By substitution of (2.16) to (2.14), it is found that the propagation constant *k* of the mean wave solution can be obtained by solving the following eigenvalue problem of the acoustic tensor $\boldsymbol{\Gamma}$:

$$\big(\boldsymbol{\Gamma} - \rho^0 \omega^2 / k^2 \mathbf{I}_{N_{dim}} \big) \cdot \boldsymbol{U} = 0 \tag{2.17}$$

Here, $\mathbf{I}_{N_{dim}}$ is $N_{dim} \times N_{dim}$ the identity matrix and $\boldsymbol{\Gamma}$ is a second-order symmetric tensor, defined by:

$$\boldsymbol{\Gamma} \cdot \boldsymbol{a} = \Big(\boldsymbol{C}^{per} : (\hat{\boldsymbol{k}} \otimes_s \boldsymbol{a}) \Big) \cdot \hat{\boldsymbol{k}} \tag{2.18}$$

where $\boldsymbol{a}$ is an arbitrary vector, $\otimes_S$ denotes the symmetric tensor product defined by $\boldsymbol{a} \otimes_S \boldsymbol{b} = 1/2 (\boldsymbol{a} \otimes \boldsymbol{b} + \boldsymbol{b} \otimes \boldsymbol{a})$ and $\boldsymbol{C}^{per}$ is written as:

$$\boldsymbol{C}^{per} = \boldsymbol{C}^0 + \langle \delta \boldsymbol{C}^g \rangle_\Theta + \Big(\langle \delta \boldsymbol{C}^g \otimes \delta \boldsymbol{C}^g \rangle_\Theta - \langle \delta \boldsymbol{C}^g \rangle_\Theta \otimes \langle \delta \boldsymbol{C}^g \rangle_\Theta \Big) : \boldsymbol{P} \tag{2.19}$$

with $\boldsymbol{P}$ a 4th-order tensor:

$$P_{m'n'p'q'} = \int_{\Omega} dV G^{T}_{p'm'}(\boldsymbol{x}';\boldsymbol{x})\left(W(\boldsymbol{r})\exp(ik\hat{\boldsymbol{k}}\cdot\boldsymbol{r})\right)_{q'n'} \tag{2.20}$$

In the particular case of the equivalent homogeneous medium, there is no scattering-induced attenuation due to the absence of elastic tensor perturbation. The acoustic tensor $\boldsymbol{\Gamma}^0$ is expressed by the constant elasticity tensor $\boldsymbol{C}^0$:

$$\boldsymbol{\Gamma}^0\cdot\boldsymbol{a} = \left(\boldsymbol{C}^0 : (\hat{\boldsymbol{k}}_0 \otimes_s \boldsymbol{a})\right)\cdot\hat{\boldsymbol{k}}_0 \tag{2.21}$$

$\boldsymbol{\Gamma}^0$ has three distinct real eigenvalues, corresponding to the propagation constants of one longitudinal wave, $k_{0L} = \omega/v_{0L}$, and two shear waves, $k_{0S} = \omega/v_{0S}$ in the unperturbed medium. Accordingly, the phase velocity for the longitudinal wave and the shear wave are given respectively as $v_{0L} = \sqrt{(\lambda^0 + 2\mu^0)/\rho}$ and $v_{0S} = \sqrt{\mu^0/\rho}$, with λ^0 and μ^0 as the Lamé parameters. The subscripts "*L*, *S*" denote respectively the longitudinal and the shear wave. On the other hand, for the studied heterogeneous medium, the wave scattering due to elastic tensor perturbations takes responsibility for amplitude attenuation and variation of wave velocity, so the wave number *k* is searched under the form $k = \omega/v + i\alpha$. Indeed the difference between the real part of *k* and k_0 quantifies the phase velocity deviation from the unperturbed medium, and the non-negative attenuation is determined by the imaginary part of *k*. The influence of the preferred crystallographic orientation to the scattering are introduced to the first order perturbation term of (2.19), $\langle\delta\boldsymbol{C}^g\rangle_\Theta$. Here, the unweighted Voigt average of the elastic tensor is chosen so that $\langle\delta\boldsymbol{C}^g\rangle_\Theta = 0$ for an untextured medium. We remark that for the Voigt averaging, the assumption of uniform strain is required and the upper bounds of the elastic moduli are obtained. The third term of (2.19) introduces some degree of multiple-scattering effects, measuring the influence of grain size and shape by the two-point spatial correlation function $W(\boldsymbol{r})$ and evaluating the effect of the crystallographic orientation accurately to ξ^2 through the factor $\langle\delta\boldsymbol{C}^g\otimes\delta\boldsymbol{C}^g\rangle_\Theta - \langle\delta\boldsymbol{C}^g\rangle_\Theta\otimes\langle\delta\boldsymbol{C}^g\rangle_\Theta$. Finally we note that, in the case where $\langle\delta\boldsymbol{C}^g\rangle_\Theta = 0$, (2.19) is simplified as:

$$\boldsymbol{C}^{per} = \boldsymbol{C}^0 + \langle\delta\boldsymbol{C}^g\otimes\delta\boldsymbol{C}^g\rangle_\Theta : \boldsymbol{P} \tag{2.22}$$

2.1.2 3D formulas for ultrasonic attenuation in cubic polycrystalline media

The particular case satisfying the previously defined "assumptions on the material heterogeneity" is frequently studied in the NDE experimental research, *i.e.* the single-phase and untextured polycrystals with equiaxed grains of cubic symmetry. Analytical formulas of the ultrasonic attenuation coefficient in such polycrystalline media are to be obtained in the following, which are useful for the validation of our numerical evaluation procedure.

Under the hypothesis of equiaxed grains, the spatial correlation function $W(\boldsymbol{x}-\boldsymbol{x}')$ of two points $\boldsymbol{x}$ and $\boldsymbol{x}'$ is simplified to a large extent and depends only on the distance $r = |\boldsymbol{x}-\boldsymbol{x}'|$ between these

two points, thus we can relate the function $W(\boldsymbol{r})$, describing a 3D characteristics, to a one-dimensional function $W(r)$. In the related literature it is often approximated by an exponential function, defined as (Stanke et al. 1984):

$$W(r) = \exp(-2r/\bar{d}) \tag{2.23}$$

The assumption of grains with a cubic symmetry makes possible to evaluate analytically the averages $\langle \delta \boldsymbol{C}^g \otimes \delta \boldsymbol{C}^g \rangle_\Theta$.

Assuming that the spatial correlation function $W(\boldsymbol{r})$ has an exponential form, as given in (2.23) and evaluating the derivatives and integrations in (2.20) analytically, an equation for normalized frequency of the longitudinal wave, $x_L = k_L \bar{d}$, without using the Born approximation is obtained (Stanke et al. 1984):

$$\begin{aligned}
&(x_L)^2 - (x_{0L})^2 \\
&= \frac{(\xi_L)^2}{4} \frac{(x_L)^2}{(x_{0L})^2} \left\{ \arctan\left(\frac{x_L}{2 + i x_{0L}} \right) \left(x_L + \frac{1}{x_L}\left(12 + 15(x_{0L})^2\right) + \frac{1}{(x_L)^3}\left(48 + 72(x_{0L})^2 + 15(x_{0L})^4\right) \right.\right. \\
&+ \frac{1}{(x_L)^5}\left(64 + 48(x_{0L})^2 + 12(x_{0L})^4 + (x_{0L})^6\right) \Big) - \arctan\left(\frac{x_L}{2 + i x_{0S}} \right) \left(x_L + \frac{1}{x_L}\left(12 - 9(x_{0S})^2\right) \right. \\
&+ \frac{1}{(x_L)^3}\left(48 - 24(x_{0S})^2 - 9(x_{0S})^4\right) + \frac{1}{(x_L)^5}\left(64 + 48(x_{0S})^2 + 12(x_{0S})^4 + (x_{0S})^6\right) \Big) \\
&- \frac{16(x_{0L})^2\left(4 + 4ix_{0L} + (x_L)^2\right)}{4 + 4ix_{0L} + (x_L)^2 - (x_{0L})^2} - \frac{20(x_{0S})^2\left(4 + 4ix_{0S} + (x_L)^2\right)}{4 + 4ix_{0S} + (x_L)^2 - (x_{0S})^2} + i(x_{0L} - x_{0S}) \\
&+ \frac{2}{(x_L)^2}\left(4i(x_{0L} - x_{0S}) - 8\left(2(x_{0L})^2 + (x_{0S})^2\right) + \frac{i}{3}\left(23(x_{0L})^3 + 13(x_{0S})^3\right) \right) \\
&\left. + \frac{1}{(x_L)^4}\left(16i(x_{0L} - x_{0S}) - 16\left((x_{0L})^2 - (x_{0S})^2\right) + 8i\left((x_{0L})^3 - (x_{0S})^3\right) - 2\left((x_{0L})^4 - (x_{0S})^4\right) + i\left((x_{0L})^5 - (x_{0S})^5\right)\right)\right\}
\end{aligned} \tag{2.24}$$

Obviously, (2.24) is an implicit equation and there is no exact analytical solution for the propagation constant *k*. Thus, the Born approximation is applied by setting $(x_L)^2 - (x_{0L})^2 \approx 2x_{0L}(x_L - x_{0L})$ on the left hand side and $x_L \approx x_{0L}$ on the right hand side so that an explicit formulas for the attenuation coefficient can be derived.

(2.24) reveals that the relative inhomogeneity of the material ξ has a dominant influence on the longitudinal wave attenuation level. For an incident wave propagating in an untextured polycrystal with cubic symmetry along the $\boldsymbol{e}_2$ direction, ξ can be approximated for the longitudinal wave as follows:

$$(\xi_L)^2 \approx \frac{4}{525} \frac{(a_c)^2}{(C^0_{2222})^2} \tag{2.25}$$

and for the shear wave:

$$(\xi_S)^2 \approx \frac{3}{700} \frac{(a_c)^2}{(C^0_{1212})^2} \tag{2.26}$$

a_c denotes the invariant anisotropy factor for crystallites of cubic symmetry:

$$a_c = C_{1111} - C_{1122} - 2C_{2323} \tag{2.27}$$

Moreover, the Rayleigh limit of the longitudinal wave, *i.e.* $x_L \to 0$, is written as (Stanke et al. 1984):

$$\alpha_L^{Rayleigh} = \frac{7}{20}\left(1+\frac{3}{2}\left(\frac{v_{0L}}{v_{0S}}\right)^5\right)(\xi_L)^2(k_{0L})^4(\bar{d})^3 \tag{2.28}$$

and the stochastic asymptote, *i.e.* $x_L \to \xi_L$, is given by (Stanke et al. 1984):

$$\alpha_L^{stochastic} = (\xi_L)^2(k_{0L})^2\bar{d} \tag{2.29}$$

It is concluded that the attenuation coefficient of the longitudinal wave is proportional to the n^{th} power of frequency and $(n-1)^{\text{th}}$ power of grain size, with $n=4$ in the Rayleigh region and $n=2$ in the stochastic region. The proportionality constant is determined by the inhomogeneity degree ξ_L of the material.

For a purely longitudinal incident wave propagating in a heterogeneous and anisotropic polycrystal, the quasi-longitudinal wave mode occurs. The particle motion is mainly longitudinal but has a small transverse component, *i.e.* the polarization vector $\boldsymbol{U}$ of the quasi-longitudinal wave has a fairly slight component perpendicular to the wave propagation direction $\hat{\boldsymbol{k}}$. It makes complicated to solve the eigenvalues of the acoustic tensor by (2.17). Nevertheless, for a slightly inhomogeneous medium, the transverse component of $\boldsymbol{U}$ is insignificant and thus can be negligible. This approximation is applied in the following analytical investigation of attenuation, making possible to gain the accessible formulas for two components of the longitudinal wave attenuation, *i.e.* the longitudinal-to-longitudinal and the longitudinal-to-shear wave scattering-induced attenuation. The validity of this approximation is to be evaluated by comparison with the result (2.24) by Stanke and Kino. Then, as another new contribution, analytical results for the attenuation coefficient and its longitudinal-to-longitudinal and longitudinal-to-shear components in the 2D case are plotted under this assumption. We remark that all the analytical results are plotted for a titanium alloy (Petry et al. 1991), whose properties are presented in Table 2.1.. Its inhomogeneity degree for the longitudinal wave is twice larger than the one of weakly-scattering material of aluminum (Stanke et al. 1984).

Consider a purely longitudinal incident wave propagating along the $\boldsymbol{e}_2$ direction. Under the approximation that the polarization vector $\boldsymbol{U}$ of the quasi-longitudinal wave is parallel to the wave propagation direction $\boldsymbol{e}_2$, an equation for k_L is found based on (2.17), which is considerably easier to work with:

$$\boldsymbol{e}_2 \cdot \boldsymbol{\Gamma} \cdot \boldsymbol{e}_2 - \rho^0 \omega^2 / \left(k_L\right)^2 = 0 \tag{2.30}$$

An implicit equation for the normalized frequency x_L is then deduced as:

$$(x_L)^2 = (x_{0L})^2 + \frac{(x_L)^2}{C^0_{2222}}\left\{\langle \delta C^g_{22p'q'}\delta C^g_{m'n'22}\rangle_\Theta \int_\Omega dV G^T_{p'm'}(\boldsymbol{x}';\boldsymbol{x})\left(W(\boldsymbol{r})\exp(ik_L r_2)\right)_{,q'n'}\right\} \tag{2.31}$$

Here, the two-point averages of elastic constant for the longitudinal wave can be denoted as:

$$\langle \delta C^g_{22p'q'}\delta C^g_{m'n'22}\rangle_\Theta = \langle \delta C^2\rangle_{p'q'm'n'} \tag{2.32}$$

and the dominant component for crystals with a cubic symmetry are evaluated as (Stanke et al. 1984):

$$\begin{aligned}&\langle \delta C^2\rangle_{2222} = \frac{16}{525}(a_c)^2,\ \langle \delta C^2\rangle_{2211} = \frac{-8}{525}(a_c)^2,\ \langle \delta C^2\rangle_{2121} = \frac{2}{105}(a_c)^2,\\ &\langle \delta C^2\rangle_{3131} = \frac{1}{105}(a_c)^2,\ \langle \delta C^2\rangle_{1111} = \frac{3}{175}(a_c)^2.\end{aligned} \tag{2.33}$$

The others can be identified by using the inherent symmetry characteristics in the elastic tensors.

The expression of Green's function in an elastically isotropic and homogeneous medium for 3D free space is know as (Eringen et al. 1975):

$$\boldsymbol{G}^{3D}(\boldsymbol{x}-\boldsymbol{x}') = \frac{1}{4\pi\rho^0\omega^2}\left(\nabla_r\left(\nabla_r\left(\frac{\exp(ik_{0S}r)}{r}-\frac{\exp(ik_{0L}r)}{r}\right)\right)+(k_{0S})^2\frac{\exp(ik_{0S}r)}{r}\mathbf{I}_3\right) \tag{2.34}$$

It is evident that the Green's tensor depends only upon the vector $\boldsymbol{r}=\boldsymbol{x}-\boldsymbol{x}'$ and is convenient to be decomposed into two tensors, noted as $\boldsymbol{G}^{L,3D}$ and $\boldsymbol{G}^{S,3D}$, associated with the longitudinal wave and the shear wave respectively. After the evaluation of derivatives, these two tensors are written as:

$$\boldsymbol{G}^{L,3D}(\boldsymbol{r}) = \frac{1}{4\pi\rho^0\omega^2}\left(\frac{\exp(ik_{0L}r)}{r^3}\left(\left(3-3ik_{0L}r-(k_{0L})^2r^2\right)\hat{\boldsymbol{r}}\otimes\hat{\boldsymbol{r}}-\left(1-ik_{0L}r\right)\mathbf{I}_3\right)\right) \tag{2.35}$$

$$\boldsymbol{G}^{S,3D}(\boldsymbol{r}) = \frac{-1}{4\pi\rho^0\omega^2}\left(\frac{\exp(ik_{0S}r)}{r^3}\left(\left(3-3ik_{0S}r-(k_{0S})^2r^2\right)\hat{\boldsymbol{r}}\otimes\hat{\boldsymbol{r}}-\left(1-ik_{0S}r-(k_{0S})^2r^2\right)\mathbf{I}_3\right)\right) \tag{2.36}$$

Here $\hat{\boldsymbol{r}}$ is the unit vector along the $\boldsymbol{r}$ direction.

Taking into account the decomposition above and applying the Born approximation in (2.31), the attenuation coefficient of the longitudinal wave is:

$$\alpha_L = \alpha_{LL} + \alpha_{LS} \tag{2.37}$$

with

$$\alpha_{LL} = \mathrm{Im}\left\{\frac{k_{0L}}{2C^0_{2222}}\langle \delta C^g_{22p'q'}\delta C^g_{m'n'22}\rangle_\Theta \int_\Omega dV G^{L,3D}_{p'm'}(\boldsymbol{r})\left(W(\boldsymbol{r})\exp(ik_{0L}r_2)\right)_{,q'n'}\right\} \tag{2.38}$$

$$\alpha_{LS} = \mathrm{Im}\left\{\frac{k_{0L}}{2C^0_{2222}}\langle \delta C^g_{22p'q'}\delta C^g_{m'n'22}\rangle_\Theta \int_\Omega dV G^{S,3D}_{p'm'}(\boldsymbol{r})\left(W(\boldsymbol{r})\exp(ik_{0L}r_2)\right)_{,q'n'}\right\} \tag{2.39}$$

where "Im" specifies the imaginary part. The indices "LL" and "LS" denote the longitudinal-to-longitudinal and the longitudinal-to-shear wave scattering respectively. The inhomogeneity of the

elastic media causes the conversion mode of the longitudinal wave to the shear wave, which induces a considerable part of the longitudinal wave attenuation.

Equations (2.37)-(2.39) have been numerically solved using Matlab and Mathematica. The evolution of the longitudinal attenuation coefficients with respect to the frequency $f \in [0, 16]$MHz is shown in Fig. 2.1. for a titanium alloy sample with averaged grain size of 160μm and compared with the analytical solution (2.24) proposed by Stanke and obtained by using the Born approximation.

It is shown that the approximated result by (2.37) is coherent with the unified solution of Stanke as shown in (2.24) with the application of the Born approximation. Only 0.4% difference is found at the maximum frequency with the assumption that the polarization vector $\boldsymbol{U}$ of the longitudinal wave in the studied heterogeneous medium is parallel to the wave propagation direction. Furthermore, only 2.7% contribution of longitudinal-to-longitudinal wave scattering to the total attenuation is observed, indicating that the longitudinal wave attenuation is caused primarily by the longitudinal-to-shear wave scattering in the considered frequency range.

Properties	Elastic Stiffness Constant			Relative Anisotropy ξ_L	Relative Anisotropy ξ_S	ρ(kg/m^3)
	C_{1111} (GPa)	C_{1122} (GPa)	C_{1212} (GPa)			
Heterogeneous polycrystalline titanium	134.0	110.0	36.0	2.74×10^{-2}	1.19×10^{-1}	4428
Reference homogeneous and isotropic material	153.0	100.0	26.5	0	0	4428

Table 2.1. Material Properties of the studied polycrystalline material

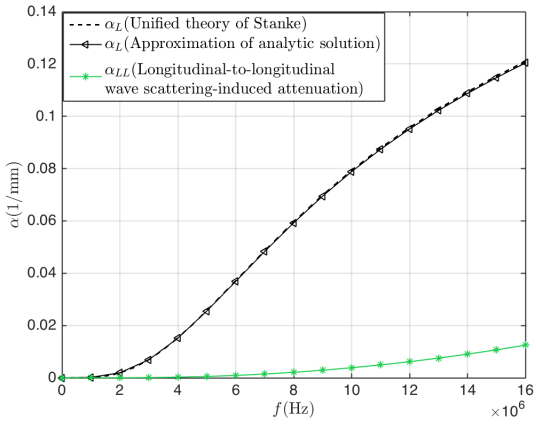

Fig. 2.1. Analytical longitudinal wave attenuation coefficient as a function of frequency for a titanium alloy sample with an averaged grain size of 160μm

Fig. 2.2. exhibits the dependence of logarithmic attenuation per crystallite ($\log_{10}(\alpha d)$) on the logarithmic normalized frequency ($\log_{10}(x_0)$). The curve is independent of the choice of grain size d. The components of attenuation due to the longitudinal-to-longitudinal scattering α_{LL} and the longitudinal-to-shear scattering α_{LS}, as well as the Rayleigh and stochastic asymptotes are also plotted in Fig. 2.2.. In the Rayleigh domain, a fourth power dependence of attenuation on the normalized frequency x_0 ((2.28)) is indicated in the curve ($\log_{10}(\alpha d)$ vs. $\log_{10}(x_0)$) in the earlier frequency region where $x_0 \le 0.3$ ($\log_{10}(x_0) \le -0.5$). It is found that the attenuation in the Rayleigh region is determined by the scattering into shear wave. This argument is in accordance with the phenomenon observed in Fig. 2.1. that only 2.7% contribution of longitudinal-to-longitudinal wave scattering to the total attenuation is observed. On the other hand, a second power dependence of attenuation on the normalized frequency x_0 in the stochastic asymptote ((2.29)), is exhibited in the frequency region where $x_0 \ge 15.9$ ($\log_{10}(x_0) \ge 1.2$). It is also seen that the longitudinal-to-longitudinal wave scattering dominates the attenuation in the stochastic region. Thereafter, a smooth transition from a fourth to a second power dependence on the normalized frequency is observed in the Rayleigh-stochastic transition region. The physical explanation for the Rayleigh-to-stochastic transition region is the change of scattering mechanism transition, *i.e.*, the longitudinal-to-shear wave scattering into the longitudinal-to-longitudinal wave scattering. This conclusion has a significant importance to the experimental measurement for the wave attenuation with the pure longitudinal incident wave. The velocity of the particle movement vertical to the wave propagation direction arises from the conversion mode and can be detected mainly in the Rayleigh region.

Particular attention should be paid to the plateau of the longitudinal-to-shear scattering curve α_{LS}, which is an indication of the stochastic-to-geometric transition for the shear wave. It is shown that the stochastic-to-geometric transition point occurs at the normalized frequency $x_{0L} \approx 4.2$ ($\log_{10}(x_{0L}) \approx 0.6$), thus at $x_{0S} \approx 8.4$. It is identical to the prediction by Stanke and Kino, *i.e.* $x_{0S} = 1/\xi_S \approx 8.4$.

As estimated by the unified theory of Stanke, the stochastic-to-geometric transition frequency for the longitudinal-to-longitudinal wave scattering-induced attenuation α_{LL} occurs at $x_{0L} = 1/\xi_L \approx 36.5$. This plateau cannot be observed due to the application of the Born approximation, which is not a good approximation in the geometric region owing to the significant attenuation. Evidently, the stochastic-to-geometric transition of the longitudinal wave occurs much later than that of shear wave. In terms of the longitudinal wave transition frequency for a given medium, it is about 4.3 times as large as that of the shear wave.

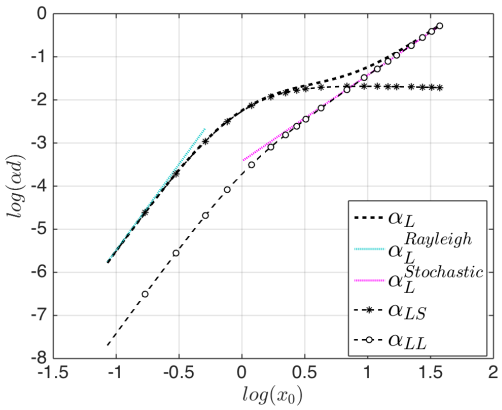

Fig. 2.2. Analytical result for logarithmic longitudinal wave attenuation per crystallite as a function of logarithmic normalized frequency in a polycrystalline titanium. α_L denotes the longitudinal wave attenuation; α_{LL}, α_{LS} are respectively the longitudinal-to-longitudinal and the longitudinal-to-shear wave scattering-induced components; $\alpha_L^{Rayleigh}$, $\alpha_L^{Stochastic}$ are respectively the Rayleigh and stochastic limits of the longitudinal wave attenuation.

2.1.3 2D formulas for ultrasonic attenuation in cubic polycrystalline media

Few analytical formulas have been developed in the related literature for ultrasonic attenuation in the 2D case. However many numerical simulations are still performed with 2D assumption, it is therefore interesting to investigate its effects. In this section, the analytical formulas for the longitudinal wave attenuation coefficient in the 2D space are developed, which are very useful for comparison with the numerical results presented in Chapter 4, as only 2D FE simulations have been conducted in the present work.

The Green's function in a 2D elastically isotropic and homogeneous medium is written as (Eringen et al. 1975):

$$\boldsymbol{G}^{2\mathrm{D}}(\boldsymbol{x}-\boldsymbol{x}') = \frac{i}{4\rho^0\omega^2}\left(\boldsymbol{\nabla}_r\left(\boldsymbol{\nabla}_r\left(H_0^{(1)}(k_{0S}r)-H_0^{(1)}(k_{0L}r)\right)\right)+(k_{0S})^2H_0^{(1)}(k_{0S}r)\mathbf{I}_2\right) \tag{2.40}$$

Here $H_0^{(1)}(.)$ denotes the Hankel function of the first kind, which expresses the outward-propagating cylindrical wave solutions since it is assumed to be uniform along $\boldsymbol{e}_3$ direction for 2D problems. (2.40) can be decomposed into linear combinations of two independent tensors associated with the longitudinal wave and shear wave field:

$$\begin{aligned}\boldsymbol{G}^{L,2\mathrm{D}}(\boldsymbol{x}-\boldsymbol{x}') = \frac{i}{4\rho^0\omega^2}\Bigg(&\left(\frac{(k_{0L})^2}{r}H_1^{(1)}(k_{0L}r)-\frac{(k_{0L})^2}{2}\left(H_0^{(1)}(k_{0L}r)-H_2^{(1)}(k_{0L}r)\right)\right)\hat{\boldsymbol{r}}\otimes\hat{\boldsymbol{r}}\\&-\left(\frac{k_{0L}}{r}H_1^{(1)}(k_{0L}r)\right)\mathbf{I}_2\Bigg)\end{aligned} \tag{2.41}$$

$$\boldsymbol{G}^{S,2\mathrm{D}}(\boldsymbol{x}-\boldsymbol{x}') = \frac{-i}{4\rho^0\omega^2}\left(\left(\frac{k_{0S}}{r}H_1^{(1)}(k_{0S}r) - \frac{(k_{0S})^2}{2}\left(H_0^{(1)}(k_{0S}r) - H_2^{(1)}(k_{0S}r)\right)\right)\hat{\boldsymbol{r}}\otimes\hat{\boldsymbol{r}} - \left(\frac{k_{0S}}{r}H_1^{(1)}(k_{0S}r) - (k_{0S})^2 H_0^{(1)}(k_{0S}r)\right)\mathbf{I}_2\right) \tag{2.42}$$

Referring to (2.37)-(2.39), the 2D integral formulas for the attenuation coefficient are numerically solved by Matlab. Result for the logarithm of attenuation per crystallite, $(\log_{10}(\alpha d))$, as a function of the logarithm of normalized frequency, $(\log_{10}(x_0))$, in the 2D space are plotted in Fig. 2.3. and is compared with result in 3D case. The slopes of the curves for $(\log_{10}(\alpha d))$ vs. $(\log_{10}(x_0))$ in both 2D and 3D cases are presented in Fig. 2.4..

Considering the longitudinal wave attenuation, it is obvious that the 2D model reduces the slope of curve at low frequencies. A cubic power dependence on the normlized frequency x_0 of the normalized attenuation αd (Fig. 2.4.) is found in the Rayleigh domain, rather than a fourth power. Since $x_0 = k_0 d$, so the attenuation α follows a second power denpendence on grain size d in the Rayleigh domain of the 2D case. In fact, as claimed by (2.28), the Rayleigh scattering is linked closely to the scattering cross section and is proportional to the volume of one grain in the 3D model. Since it is the area of the scatter that works for the scattering mechanism in the 2D model, the grain size dependence reduces to the second power. Further mathematical considerations for the Rayleigh limit in 2D model is not given since the function in (2.37)-(2.39) for the 2D model can not be analytically integrated. Whereas, a second power dependence on the normalized frequency x_0 of the normalized attenuation αd is obtained in the stochastic asymptote of the 2D model, which is identical with the 3D model. It is indicated that attenuaiton α is proportional to grain size d in the stochastic limit. Effectively, the stochastic scattering is a one-dimensional phenomenon and linked only to the effective averaged grain dimension in the wave propagation direction (Yang et al. 2011), shown in (2.29). Therefore, the 2D and 3D models are equivalent at higher frequencies for the same medium. Furthermore, the components of the longitudinal-to-longitudinal and the longitudinal-to-shear scattering-induced attenuation in the 2D model are also presented in Fig. 2.3.. The identical scattering mechanisms with the 3D model for both the Rayleigh and stochastic regions are found. However, the transition from the Rayleigh to stochastic region in the 2D case occurs slightly earlier than the 3D case. As described in Fig. 2.4., the slope of the curve $(\log_{10}(\alpha d))$ vs. $(\log_{10}(x_0))$ in the 3D case is larger in the frequency region where $x_0 < 2$ and afterwards becomes smaller than that of 2D models.

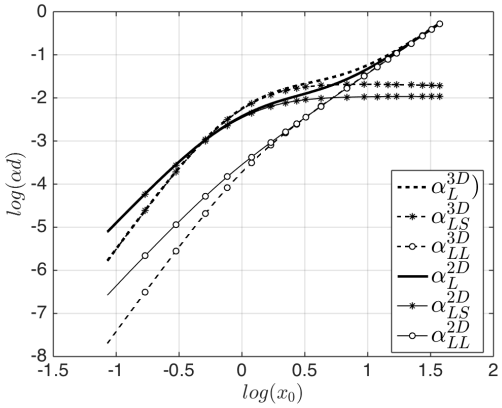

Fig. 2.3. Comparison of analytical longitudinal wave attenuation per crystallite versus normalized frequency between 2D and 3D models in a polycrystalline titanium. α_L denotes the longitudinal wave attenuation; α_{LL}, α_{LS} are respectively the longitudinal-to-longitudinal and the longitudinal-to-shear wave scattering-induced components.

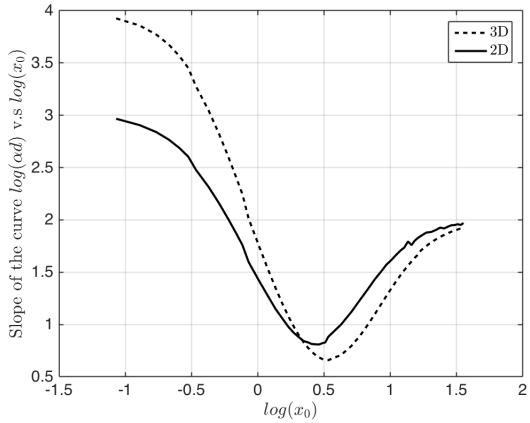

Fig. 2.4. Comparison of the slope of the curves $(\log_{10}(\alpha d))$ vs. $(\log_{10}(x_0))$ between 2D and 3D models.

To exhibit grain size effects on attenuation, 3D and 2D analytical curves of longitudinal wave attenuation coefficient versus frequency $f \in [0,16]$MHz for the polycrystalline titanium with three different grain sizes of 80μm, 160μm and 320μm ($x_0 = 2\pi fd/v_0 \in [0,1.4]$, $[0,0.28]$, $[0,0.56]$ respectively) are plotted (Fig. 2.5.). It is seen that attenuation increases with grain size in the low frequency region where $f < 8$MHz. Attenuation for the sample with a larger grain size intersects with the curve of a smaller grain size at a certain frequency due to the transition of scattering region. Comparison between 3D and 2D results shows that longitudinal wave attenuation in the 2D case is slightly larger than that of 3D space in the Rayleigh region and smaller than that of 3D space in a higher frequency region for a given grain size.

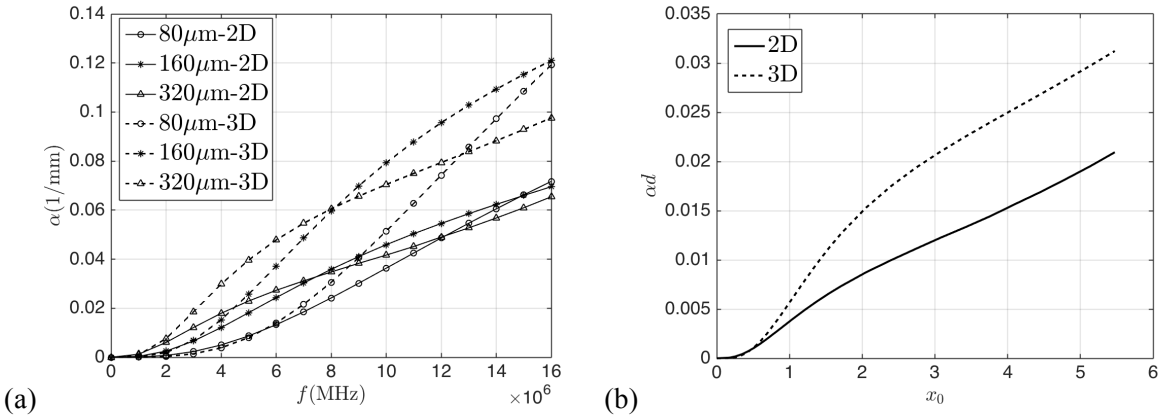

Fig. 2.5. Analytical results of the longitudinal wave attenuation coefficient for a polycrystalline titanium with different grain sizes in the 3D and 2D cases (a) α vs. f; (b) master curves αd vs. x_0.

2.2 A unified framework for theoretical and numerical evaluations of grain-noise scattering coefficient

In this section, a unified framework for theoretical and numerical evaluations of microstructural noise scattering coefficient is presented. First, formulas for microstructural noise scattering coefficient in the 3D space based on the reciprocity theorem and the isolated scatter model are reviewed. 2D general formulas are further developed as a new contribution. A coefficient of proportionality depending on the spatial dimension N_{dim} is determined based on the equivalence of the reciprocity theorem and isolated scatter model with the Born approximation and the single-scattering assumption. The 3D analytical formulas for the backscattering coefficient in single-phase, equiaxed and untextured polycrystalline microstructures are recalled and the corresponding 2D explicit analytical formulas are developed as a new result. Finally as one of the most important results of the present work, an original approach based on FE modeling for numerical evaluation of microstructural noise scattering coefficient within the unified framework of the reciprocity theorem is presented.

2.2.1 Reciprocity gap due to the microstructural scattering

Consider an elastic wave propagating in a slightly inhomogeneous polycrystalline medium as defined by the time harmonic equations (2.1). Based on the reciprocity theorem, the basic idea of evaluating the grain-noise scattering is to quantify the so-called "reciprocity gap", which is derived by the comparison between the studied heterogeneous domain and the equivalent homogeneous domain in which the time harmonic equations are defined by (2.10) (shown in Fig. 2.6.). Then the following variational formulations are straightforward for both systems:

$$(\boldsymbol{\sigma}, \boldsymbol{\varepsilon}(\boldsymbol{u}^0))_\Omega - (\rho^0\omega^2\boldsymbol{u}, \boldsymbol{u}^0)_\Omega = (\boldsymbol{\sigma}\cdot\boldsymbol{n}, \boldsymbol{u}^0)_{\partial\Omega} \tag{2.43}$$

$$(\boldsymbol{\sigma}^0, \boldsymbol{\varepsilon}(\boldsymbol{u}))_\Omega - (\rho^0\omega^2\boldsymbol{u}^0, \boldsymbol{u})_\Omega = (\boldsymbol{\sigma}^0\cdot\boldsymbol{n}, \boldsymbol{u})_{\partial\Omega} \tag{2.44}$$

where $\boldsymbol{n}$ is the outward unit normal to the boundary $\partial\Omega$, $(\cdot,\cdot)_\Omega$ and $(\cdot,\cdot)_{\partial\Omega}$ denote integrations respectively over the volume Ω and the surface $\partial\Omega$ of the appropriate dot product between two vectors or two tensors. Subtracting (2.44) from (2.43) leads to the following general equation of the reciprocity theorem for elastic waves in the presence of scatterers, such as flaws or grain boundaries:

$$(\boldsymbol{\sigma}\cdot\boldsymbol{n},\boldsymbol{u}^0)_{\partial\Omega}-(\boldsymbol{\sigma}^0\cdot\boldsymbol{n},\boldsymbol{u})_{\partial\Omega}=(\delta\boldsymbol{C}:\boldsymbol{\varepsilon}(\boldsymbol{u}),\boldsymbol{\varepsilon}(\boldsymbol{u}^0))_\Omega \tag{2.45}$$

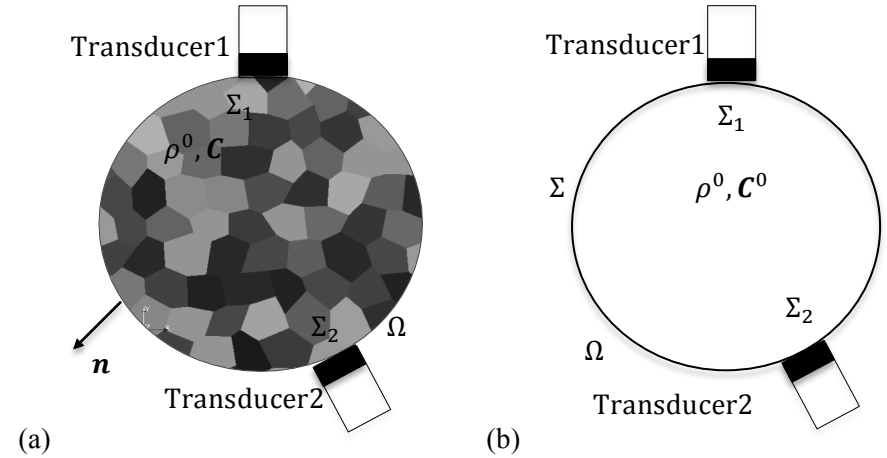

Fig. 2.6. Schematic diagram of the systems considered in the measurement of scattering in (a) a heterogeneous medium by comparison with (b) a homogeneous reference medium

Both terms represent a reciprocity gap and can be used to measure the degree of perturbation due to the inhomogeneities in the studied medium. Furthermore the equation (2.45) points out that there are two ways to evaluate the reciprocity gap. The first one is to integrate over the whole volume of the studied domain by using a Green's function approach under the Born approximation assumption and gives rise to a theoretical estimation of the scattering. The second one is to calculate a surface integration involving only the mechanical quantities available on the boundary of the studied domain and therefore can be used for experimental measurements.

2.2.2 Physical signification of the reciprocity theorem applied to microstructural scattering analysis

In this section we reformulate, in the case of polycrystalline materials, the scattering formulas proposed by Kino (Kino 1978). Indeed it allows an interesting insight into how the reciprocity gap is precisely related to the amplitude of elastic wave noise signals scattered by the inhomogeneity of polycrystalline microstructure using the reciprocity theorem.

For both heterogeneous and homogeneous reference systems, two transducers in contact with the boundary $\partial\Omega$ are considered and the contact areas are respectively denoted as Σ_1 and Σ_2. The transducer used as a transmitter can generate elastic waves in Ω by applying prescribed displacements or surface loadings on its contact area, and the elastic wave fields within Ω are assumed to be not perturbed by the transducers. On the remainder of the boundary, *i.e.* $\Sigma=\partial\Omega-(\Sigma_1\cup\Sigma_2)$, the free

boundary condition is assumed. At the surface of the transmitter Σ_m, the displacement and stress vector fields in time domain can be described as:

$$\boldsymbol{u}_m^+(\boldsymbol{x}, t) = A_m^+ \boldsymbol{u}_m^+(\boldsymbol{x}) \exp(-i\omega t) \tag{2.46}$$

$$\boldsymbol{\sigma}_m^+(\boldsymbol{x}, t) \cdot \boldsymbol{n} = A_m^+ \boldsymbol{\sigma}_m^+(\boldsymbol{x}) \cdot \boldsymbol{n} \exp(-i\omega t) \tag{2.47}$$

where $m = 1, 2$ represents a transducer, the superscript "$+$" represents the fields associated to the transmitter and A_m^+ is the amplitude of elastic waves excited by the transducer m. For a given angular frequency ω, the power rate at which energy is carried across Σ_m is classically calculated as the time average within the corresponding period $T = 2\pi\omega$:

$$P_m(\omega) = \frac{1}{T} \int_0^T \left(\mathrm{Re}\left(\boldsymbol{\sigma}_m^+(\boldsymbol{x}, t) \cdot \boldsymbol{n}\right), \mathrm{Re}\left(\dot{\boldsymbol{u}}_m^+(\boldsymbol{x}, t)\right) \right)_{\Sigma_m} dt \tag{2.48}$$

where the dot above the displacement field indicates the derivative with respect to time. Then it can be shown that:

$$P_m(\omega) = \frac{1}{2} A_m^+ A_m^{+*} \left(\mathrm{Re}\left(\boldsymbol{\sigma}_m^+(\boldsymbol{x}) \cdot \boldsymbol{n}\right), \mathrm{Re}\left(\dot{\boldsymbol{u}}_m^+(\boldsymbol{x})\right) \right)_{\Sigma_m} = -\frac{\omega}{2} A_m^+ A_m^{+*} \mathrm{Im}\left(\boldsymbol{\sigma}_m^+(\boldsymbol{x}) \cdot \boldsymbol{n}, \boldsymbol{u}_m^{+*}(\boldsymbol{x})\right)_{\Sigma_m} \tag{2.49}$$

where the superscript "$*$" indicates the complex conjugate.

When $\boldsymbol{u}_m^+(\boldsymbol{x})$ and $\boldsymbol{\sigma}_m^+(\boldsymbol{x}) \cdot \boldsymbol{n}$ are chosen, the unit power rate is obtained:

$$\frac{1}{2} \left(\mathrm{Re}\left(\boldsymbol{\sigma}_m^+(\boldsymbol{x}) \cdot \boldsymbol{n}\right), \mathrm{Re}\left(\dot{\boldsymbol{u}}_m^+(\boldsymbol{x})\right) \right)_{\Sigma_m} = -\frac{\omega}{2} \mathrm{Im}\left(\boldsymbol{\sigma}_m^+(\boldsymbol{x}) \cdot \boldsymbol{n}, \boldsymbol{u}_m^{+*}(\boldsymbol{x})\right)_{\Sigma_m} = 1 \tag{2.50}$$

Then (2.49) becomes:

$$P_m(\omega) = A_m^+ A_m^{+*} \tag{2.51}$$

Once the prescribed displacements of the surface loadings vanish, the transducers can also serve as a receiver recording to the elastic wave propagating in the opposite direction. If we assume that the received displacements and stress vectors have exactly the same form as (2.46) and (2.47), they can be written as follows:

$$\boldsymbol{u}_m^-(\boldsymbol{x}, t) = A_m^- \boldsymbol{u}_m^-(\boldsymbol{x}) \exp(-i\omega t) \tag{2.52}$$

$$\boldsymbol{\sigma}_m^-(\boldsymbol{x}, t) \cdot \boldsymbol{n} = A_m^- \boldsymbol{\sigma}_m^-(\boldsymbol{x}) \cdot \boldsymbol{n} \exp(-i\omega t) \tag{2.53}$$

with

$$\boldsymbol{u}_m^-(\boldsymbol{x}) = \boldsymbol{u}_m^{+*}(\boldsymbol{x}) \tag{2.54}$$

$$\boldsymbol{\sigma}_m^-(\boldsymbol{x}) \cdot \boldsymbol{n} = -\boldsymbol{\sigma}_m^{+*}(\boldsymbol{x}) \cdot \boldsymbol{n} \tag{2.55}$$

where the superscript "$-$" represents the receiver and the minus sign in the expression of $\boldsymbol{\sigma}_m^-(\boldsymbol{x}) \cdot \boldsymbol{n}$ is due to the fact that the wave vector of the received waves is in the opposite direction to the one of the

incident waves. Since the considered systems here are linear, the displacement and the stress vector fields on the contact area of each transducer can be summed up:

$$\boldsymbol{u}_m(\boldsymbol{x}) = A_m^+ \boldsymbol{u}_m^+(\boldsymbol{x}) + A_m^- \boldsymbol{u}_m^-(\boldsymbol{x}) \tag{2.56}$$

$$\boldsymbol{\sigma}_m(\boldsymbol{x}) \cdot \boldsymbol{n} = A_m^+ \boldsymbol{\sigma}_m^+(\boldsymbol{x}) \cdot \boldsymbol{n} - A_m^- \boldsymbol{\sigma}_m^-(\boldsymbol{x}) \cdot \boldsymbol{n} \tag{2.57}$$

Then the scattering matrix $[S]$ that contains ratios of received wave amplitudes to incident wave amplitudes is defined as:

$$\begin{pmatrix} A_1^- \\ A_2^- \end{pmatrix} = \begin{bmatrix} S_{11} & S_{12} \\ S_{21} & S_{22} \end{bmatrix} \begin{pmatrix} A_1^+ \\ A_2^+ \end{pmatrix} \tag{2.58}$$

$[S]$ is decomposed in two parts: $S = S^0 + \delta S$ where $[S^0]$ is the scattering matrix in the homogeneous reference medium. Considering the interchangeability of the transmitter and the receiver, the reciprocity relation simply reads as $S_{21}^0 = S_{12}^0$. Herein only the microstructural noise scattering matrix $[\delta S]$ is of interest. Each term of $[\delta S]$ can be determined by different experimental settings.

As an example a typical situation is considered: Transducer 1 used as transmitter and Transducer 2 used as receiver for the heterogeneous medium for which the solutions are denoted as $(\boldsymbol{u}^{1\to 2}, \boldsymbol{\sigma}^{1\to 2})$; Transducer 1 used as receiver and Transducer 2 used as transmitter for the reference medium for which the solutions are denoted as $(\boldsymbol{u}^{0;2\to 1}, \boldsymbol{\sigma}^{0;2\to 1})$. In this situation the amplitudes of the elastic wave signals received or emitted by the transducers in both systems can be written as:

$$A_1^+ = \text{finite}, A_1^- = 0; A_2^+ = 0, A_2^- = (S_{21}^0 + \delta S_{21}) A_1^+ \tag{2.59}$$

$$\left(A_1^+\right)^0 = 0, \left(A_1^-\right)^0 = S_{21}^0 \left(A_2^+\right)^0; \left(A_2^+\right)^0 = \text{finite}, \left(A_2^-\right)^0 = 0 \tag{2.60}$$

Taking into account (2.59) and (2.60) and substituting the displacement and stress vector fields defined respectively in (2.56) and (2.57) into the left-hand side of the reciprocity relation in (2.46), the following expression can be easily obtained:

$$\left(\boldsymbol{\sigma}^{1\to 2} \cdot \boldsymbol{n}, \boldsymbol{u}^{0;2\to 1}\right)_{\partial\Omega} - \left(\boldsymbol{\sigma}^{0;2\to 1} \cdot \boldsymbol{n}, \boldsymbol{u}^{1\to 2}\right)_{\partial\Omega} = \frac{-4}{i\omega} \delta S_{21}(\omega) P_0(\omega) \tag{2.61}$$

with $P_0(\omega)$ the incident power rate emitted by the transmitter:

$$P_0(\omega) = -\frac{\omega}{2} A_1^+ \left(A_2^+\right)^0 \operatorname{Im}\left(\boldsymbol{\sigma}_1^+(\boldsymbol{x}) \cdot \boldsymbol{n}, \boldsymbol{u}_1^{+*}(\boldsymbol{x})\right)_{\Sigma_1} = A_1^+ \left(A_2^+\right)^0 \tag{2.62}$$

Therefore, the amplitude of the microstructural noise signals scattered by the polycrystalline medium and received by the transducer 2, when an incident signal is emitted from the transducer 1, can be calculated as:

$$\delta S_{21}(\omega) = \frac{-i\omega}{4 P_0(\omega)} \left(\delta \boldsymbol{C} : \boldsymbol{\varepsilon}(\boldsymbol{u}^{1\to 2}), \boldsymbol{\varepsilon}(\boldsymbol{u}^{0;2\to 1})\right)_{\Omega} \tag{2.63}$$

$$\delta S_{21}(\omega) = \frac{-i\omega}{4P_0(\omega)}\left(\left(\boldsymbol{\sigma}^{1\to 2}\cdot\boldsymbol{n},\boldsymbol{u}^{0;2\to 1}\right)_{\partial\Omega} - \left(\boldsymbol{\sigma}^{0;2\to 1}\cdot\boldsymbol{n},\boldsymbol{u}^{1\to 2}\right)_{\partial\Omega}\right) \tag{2.64}$$

Equations (2.63) and (2.64) express two equivalent ways to evaluate the microstructural noise scattering amplitude δS_{21} using respectively a volume and a surface integration. In the following, the equation (2.63) is used to obtain analytical formulas of the scattering coefficient based on an isolated scatterer model and using the Green's function approach, while the equation (2.64) allows the definition of our numerical procedure to measure the scattering coefficient using recorded mechanical data at the boundary of the studied domain. Otherwise it is interesting to indicate that the scattered signal amplitude in an arbitrary spatial direction may be obtained by placing the two transducers 1 and 2 along this direction. For the particular case of the backscattering coefficient, the same formulas for the backscattering amplitude δS_{11} are obtained by using two coincident transducers.

2.2.3 Theoretical formulas of scattered amplitudes and differential cross sections based on the isolated scatterer model

The theoretical analysis of scattered amplitudes and differential cross sections in 3D case proposed by Gubernatis et al. (Gubernatis et al. 1977) is recalled. As a new contribution, the development of the theoretical formulas in 2D case is given. The obtained 2D formulas are important for the comparison between the theoretical estimation and the 2D numerical simulations.

The analysis is based on the isolated scatterer model as the differential cross section is calculated by considering a bounded region of scatterers Ω_{SC} embedded in an infinite homogeneous region R and by using the far-field values of the scattered displacement and stress fields.

2.2.3.1 Far-field scattered displacement solution

In a very classical way, the displacement field in the whole region R is decomposed into two parts: the incident wave field $\boldsymbol{u}^{inc}$ and the scattered wave field $\boldsymbol{u}^{scat}$:

$$\boldsymbol{u}(\boldsymbol{x}) = \boldsymbol{u}^{inc}(\boldsymbol{x}) + \boldsymbol{u}^{scat}(\boldsymbol{x}) \tag{2.65}$$

then for all $\boldsymbol{x}\in \mathrm{R}$, the time harmonic elastic wave equation (2.1) can be transformed in the following way by considering the perturbation of inhomogeneities as a source term $\boldsymbol{f}$:

$$\mathbf{Div}_x\left(\boldsymbol{C}^0 : \boldsymbol{\varepsilon}(\boldsymbol{u})\right) + \rho^0\omega^2\boldsymbol{u} + \boldsymbol{f} = 0 \tag{2.66}$$

with

$$\boldsymbol{f} = \mathbf{Div}_x\left(\gamma\delta\boldsymbol{C} : \boldsymbol{\varepsilon}(\boldsymbol{u})\right) \tag{2.67}$$

The characteristic function $\gamma(\boldsymbol{x})$ of the flaw region Ω_{SC} is equal to one in Ω_{SC} and to zero otherwise.

According to the well-known Green's function approach, the following formula of $\boldsymbol{u}(\boldsymbol{x})$ is straightforward for all $\boldsymbol{x}\in \mathrm{R}$:

$$\boldsymbol{u}(\boldsymbol{x}) = \boldsymbol{u}^{inc}(\boldsymbol{x}) + \int_{\mathrm{R}} \boldsymbol{G}^{T}(\boldsymbol{x}';\boldsymbol{x}) \cdot \boldsymbol{f}(\boldsymbol{x}') d\boldsymbol{x}' \tag{2.68}$$

Substituting (2.67) into (2.68) and taking into account the fact $\boldsymbol{G}(\boldsymbol{x}';\boldsymbol{x}) \to \boldsymbol{G}(0;\boldsymbol{x}-\boldsymbol{x}')$ when $|\boldsymbol{x}| \to \infty$, the far-field solution of the scattered displacement $\boldsymbol{u}^{scat}(\boldsymbol{x})$ is finally obtained:

$$\boldsymbol{u}^{scat}(\boldsymbol{x}) = \int_{\Omega_{\mathrm{SC}}} \left(\boldsymbol{\varepsilon}(\boldsymbol{u}(\boldsymbol{x}')) : \delta\boldsymbol{C} : \boldsymbol{\varepsilon}(\boldsymbol{G}(\boldsymbol{x}-\boldsymbol{x}') \cdot \boldsymbol{e}_m) \right) \boldsymbol{e}_m \, d\boldsymbol{x}' \tag{2.69}$$

where for ease of notation, $\boldsymbol{G}(0;\boldsymbol{x}-\boldsymbol{x}')$ is denoted as $\boldsymbol{G}(\boldsymbol{x}-\boldsymbol{x}')$.

It is obvious that (2.69) expressing the scattered wave field in terms of integration over the volume of the scatter region Ω_{SC} cannot be directly used, as the displacement field $\boldsymbol{u}(\boldsymbol{x})$ within Ω_{SC} is generally unknown. However it is useful to develop a theoretical estimation of the scattered amplitudes when the Green's function $\boldsymbol{G}(\boldsymbol{x}-\boldsymbol{x}')$ is known. It is precisely the case for an infinite isotropic and homogeneous elastic domain.

2.2.3.2 Far-field scattered amplitudes in the 3D case

We consider at first the 3D case for which the coordinate system is presented in Fig. 2.7. The centroid of the scatterer domain Ω_{SC} is set to be coincident with the origin of the coordinate system.

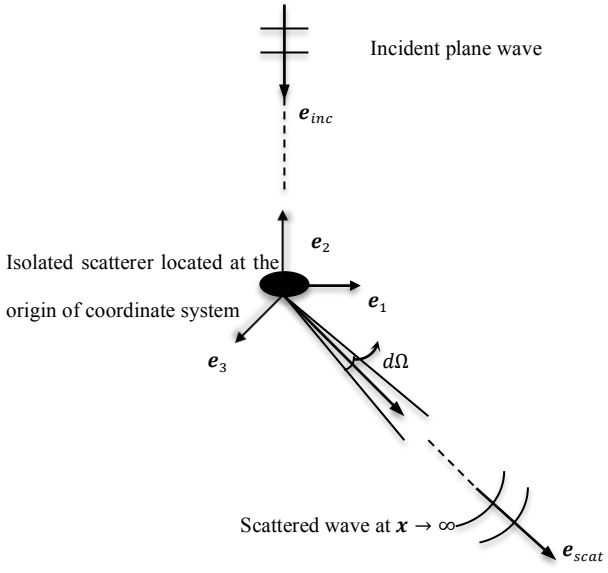

Fig. 2.7. Diagram of the systems considered in the isolated scatter model

Denoting by $\boldsymbol{e}_{scat}(\boldsymbol{x})$ the considered unit scattered direction vector, *i.e.* $\boldsymbol{x} = |\boldsymbol{x}| \boldsymbol{e}_{scat}$, and taking into account the fact that, for $\boldsymbol{x}' \in \Omega_{\mathrm{SC}}$ and $\boldsymbol{x} \in \mathrm{R}$, we have $r^{-1} \sim |\boldsymbol{x}|^{-1}$ and $r^{-1} \sim |\boldsymbol{x}| - \boldsymbol{x}' \cdot \boldsymbol{e}_{scat}$ when $\boldsymbol{x} \to \infty$, the far-field solution of the scattered displacement $\boldsymbol{u}^{scat}$ and stress $\boldsymbol{\sigma}^{scat}$ can be derived from (2.69) as follows (see also Appendix B):

$$\boldsymbol{u}^{scat}(\boldsymbol{x}) \sim \sum_{l=L,S} \boldsymbol{A}_l(\boldsymbol{e}_{scat}) \frac{\exp(i k_{0l} |\boldsymbol{x}|)}{|\boldsymbol{x}|} \tag{2.70}$$

$$\boldsymbol{\sigma}^{scat}(\boldsymbol{x}) \sim i\lambda k_{0L}(\boldsymbol{A}_L \cdot \boldsymbol{e}_{scat}) \frac{\exp(i k_{0L}|\boldsymbol{x}|)}{|\boldsymbol{x}|} \mathbf{I}_3 + 2i\mu \sum_{l=L,S} k_{0l}(\boldsymbol{A}_l \otimes_S \boldsymbol{e}_{scat}) \frac{\exp(i k_{0l}|\boldsymbol{x}|)}{|\boldsymbol{x}|} \tag{2.71}$$

with

$$\boldsymbol{A}_L(\boldsymbol{e}_{scat}) = (\boldsymbol{e}_{scat} \otimes \boldsymbol{e}_{scat}) \cdot \boldsymbol{a}(\boldsymbol{k}_{0L}) \tag{2.72}$$

$$\boldsymbol{A}_S(\boldsymbol{e}_{scat}) = (\mathbf{I}_3 - \boldsymbol{e}_{scat} \otimes \boldsymbol{e}_{scat}) \cdot \boldsymbol{a}(\boldsymbol{k}_{0S}) \tag{2.73}$$

$$\boldsymbol{a}(\boldsymbol{k}_{0l}) = \frac{\chi(k_{0l}, N_{dim})}{4\pi\rho^0 (v_{0l})^2} \int_{\Omega_{SC}} -i\boldsymbol{k}_{0l} \left(\delta\boldsymbol{C}(\boldsymbol{x}') : \boldsymbol{\varepsilon}(\boldsymbol{u}(\boldsymbol{x}'))\right) \exp(-i\boldsymbol{k}_{0l} \cdot \boldsymbol{x}')\, d\boldsymbol{x}' \tag{2.74}$$

where the symbol "∼" indicates the asymptotic forms, $\boldsymbol{k}_{0L} = k_{0L}\boldsymbol{e}_{scat}$ and $\boldsymbol{k}_{0S} = k_{0S}\boldsymbol{e}_{scat}$ are the wave vectors of respectively the longitudinal waves and the shear waves.

In the present work, we introduce a constant $\chi(k_{0l}, N_{dim})$, which depends on the space dimension. It is equal to *1* for the 3D case with $N_{dim} = 3$ and will be calculated in the following section for the 2D case. The equation (2.70) shows that the scattered field $\boldsymbol{u}^{scat}$ can be decomposed into a longitudinal wave contribution with amplitude $\boldsymbol{A}_L$ parallel to $\boldsymbol{e}_{scat}$ and a shear wave contribution with amplitude $\boldsymbol{A}_S$ perpendicular to $\boldsymbol{e}_{scat}$. Both amplitudes are determined by the vectors $\boldsymbol{k}_{0l}(l = L, S)$, whose complete calculation requires the complete information of the field $\boldsymbol{u}$ inside Ω_{SC}.

2.2.3.3 Far field scattered amplitudes in the 2D case

Following the same theoretical development presented above for the 3D case, analytical formulas for the far-field displacements can be obtained in the 2D case. When $|\boldsymbol{x}| \to \infty$, substituting the Green's function of the 2D case (2.40) into (2.69), the following formulas for the far-field solution of the scattered displacement $\boldsymbol{u}^{scat,2D}$ and stress $\boldsymbol{\sigma}^{scat,2D}$ are obtained like in the 3D case (see also Appendix B):

$$\boldsymbol{u}^{scat,2D}(\boldsymbol{x}) \sim \sum_{l=L,S} \boldsymbol{A}_l(\boldsymbol{e}_{scat}) \frac{\exp(i k_{0l}|\boldsymbol{x}|)}{|\boldsymbol{x}|^{1/2}} \tag{2.75}$$

$$\boldsymbol{\sigma}^{scat,2D}(\boldsymbol{x}) \sim i\lambda k_{0L}(\boldsymbol{A}_L \cdot \boldsymbol{e}_{scat}) \frac{\exp(i k_{0L}|\boldsymbol{x}|)}{|\boldsymbol{x}|^{1/2}} \mathbf{I}_2 + 2i\mu \sum_{l=L,S} k_{0l}(\boldsymbol{A}_l \otimes_S \boldsymbol{e}_{scat}) \frac{\exp(i k_{0l}|\boldsymbol{x}|)}{|\boldsymbol{x}|^{1/2}} \tag{2.76}$$

where $\boldsymbol{A}_L$ and $\boldsymbol{A}_S$ are always defined by (2.72)-(2.74), but with the following space dimension dependent constant $\chi(k_{0l}, N_{dim})$, which is an important result of the present work:

$$\chi(k_{0l}, N_{dim} = 2) = \frac{(1+i)\pi^{1/2}}{(k_{0l})^{1/2}} \tag{2.77}$$

2.2.3.4 Theoretical formulas for differential cross sections

Classically the differential cross section $dP(\omega)/d\Omega$ gives, for a given angular frequency ω, the measure of the fraction of incident power scattered into a particular direction $\boldsymbol{e}_{scat}$ across the surface

dA defined by the differential element of solid angle $d\Omega$ in that direction. In the 3D case, we have $dA = |\boldsymbol{x}|^2 \, d\Omega$, while in the 2D case, we have $dA = |\boldsymbol{x}| d\Omega$.

It can be proven that in the 3D case:

$$\frac{dP(\omega)}{d\Omega}(\boldsymbol{e}_{scat}) = \lim_{|x|\to\infty}\left(-\frac{\omega}{2}\mathrm{Im}\left(|\boldsymbol{x}|^2 \left(\boldsymbol{\sigma}^{scat}\cdot\boldsymbol{e}_{scat}\right)\cdot\left(\boldsymbol{u}^{scat}\right)^*\right)\right) \Big/ P_0(\omega) \tag{2.78}$$

while in the 2D case:

$$\frac{dP(\omega)}{d\Omega}(\boldsymbol{e}_{scat}) = \lim_{|x|\to\infty}\left(-\frac{\omega}{2}\mathrm{Im}\left(|\boldsymbol{x}| \left(\boldsymbol{\sigma}^{scat,2D}\cdot\boldsymbol{e}_{scat}\right)\cdot\left(\boldsymbol{u}^{scat,2D}\right)^*\right)\right) \Big/ P_0(\omega) \tag{2.79}$$

where $P_0(\omega)$ is the power rate of the incident fields defined in Section 2.2.2. When $|\boldsymbol{x}| \to \infty$, as $\boldsymbol{\sigma}^{scat}$ and $\boldsymbol{u}^{scat}$ are respectively proportional to $|\boldsymbol{x}|^{-1}$ and $|\boldsymbol{x}|^{-1/2}$ in the 3D and 2D cases (see (2.70), (2.71), (2.75) and (2.76)), the equations of the differential cross sections (2.78) and (2.79) show that they are independent of the distance from the scatter.

In the case of an incident wave containing both the longitudinal and the shear waves of amplitude $\boldsymbol{A}_{iL}$ and $\boldsymbol{A}_{iS}$, the displacement field is defined in the following way:

$$\boldsymbol{u}^{inc}(\boldsymbol{x}) = \boldsymbol{A}_{iL}\exp(ik_{0L}\boldsymbol{e}_{inc}\cdot\boldsymbol{x} - i\omega t) + \boldsymbol{A}_{iS}\exp(ik_{0S}\boldsymbol{e}_{inc}\cdot\boldsymbol{x} - i\omega t) \tag{2.80}$$

It can be shown that the differential cross sections for both 3D and 2D cases have the same expression as follows:

$$\frac{dP(\omega)}{d\Omega}(\boldsymbol{e}_{scat}) = \frac{k_{0L}(\lambda^0 + 2\mu^0)\left|\boldsymbol{A}_L(\boldsymbol{e}_{scat})\right|^2 + \mu^0 k_{0S}\left|\boldsymbol{A}_S(\boldsymbol{e}_{scat})\right|^2}{k_{0L}(\lambda^0 + 2\mu^0)\left|\boldsymbol{A}_{iL}\right|^2 + \mu^0 k_{0S}\left|\boldsymbol{A}_{iS}\right|^2} \tag{2.81}$$

So the scattered amplitudes are directly linked to the differential cross sections.

In the case where the incident field contains only longitudinal waves, *i.e.* $|\boldsymbol{A}_{iS}| = 0$, we have:

$$\frac{dP(\omega)}{d\Omega}(\boldsymbol{e}_{scat}) = \frac{\left|\boldsymbol{A}_L(\boldsymbol{e}_{scat})\right|^2}{\left|\boldsymbol{A}_{iL}\right|^2} + \frac{v_{0S}}{v_{0L}}\frac{\left|\boldsymbol{A}_S(\boldsymbol{e}_{scat})\right|^2}{\left|\boldsymbol{A}_{iL}\right|^2} \tag{2.82}$$

The two terms on the right hand side of (2.82) are respectively the longitudinal-to-longitudinal and longitudinal-to-shear differential cross sections. In the following, only the longitudinal-to-longitudinal differential cross section $\left|\boldsymbol{A}_L(\boldsymbol{e}_{scat})\right|^2 \Big/ \left|\boldsymbol{A}_{iL}\right|^2$ is considered for the theoretical analysis.

2.2.4 Theoretical and numerical evaluations of microstructural noise scattering coefficient

The microstructural noise scattering effectiveness is quantified by the scattering coefficient $\eta(\omega, \boldsymbol{e}_{scat})$, defined as the differential scattering cross section per unit volume for a given angular frequency ω and in a particular direction $\boldsymbol{e}_{scat}$ per unit incident power rate. Sections 2.2.2 and 2.2.3 present two ways to evaluate $\eta(\omega, \boldsymbol{e}_{scat})$ and we recall in the present section the equivalence between them under the assumption of weak-scattering and with the use of the Born approximation.

Furthermore, the comparison of both methods allows the identification of a proportionality coefficient between them, already given in the literature for the 3D case. Then as a new result this proportionality coefficient is identified in the 2D case.

2.2.4.1 Theoretical measure of the scattering coefficient

Now we consider the polycrystalline domain Ω by assuming that it is single phase with randomly oriented grains and is macroscopically isotropic and homogeneous. We denote by N the total number of grains in the active volume V_{pc} of grain scattering (Rose 1992).

By the first method based on the independent scattering approximation, each grain in Ω is regarded as an isolated scatterer placed in the homogeneous reference medium and their contributions to the total scattering are summed up incoherently. This gives rise to the following formula of the scattering coefficient:

$$\eta(\omega, \boldsymbol{e}_{scat}) = \frac{1}{\left|\boldsymbol{A}_{iL}\right|^2} \frac{N}{V_{pc}} \left\langle \left| \boldsymbol{A}_L(g^I, \boldsymbol{e}_{scat}) \right|^2 \right\rangle = \frac{1}{\left|\boldsymbol{A}_{iL}\right|^2} \frac{N}{V_{pc}} \frac{\sum_I \left| \boldsymbol{A}_L(g^I, \boldsymbol{e}_{scat}) \right|^2}{N} \tag{2.83}$$

where $\langle \cdot \rangle$ denotes an average over all the N grains. Note the longitudinal-to-shear scattering part is not considered in (2.83).

Due to the single phase assumption and when N is large enough, the average $\langle \delta \boldsymbol{C}^I \otimes \delta \boldsymbol{C}^I \rangle_\Theta$ over all grains is equal to the average over all crystallographic orientations and is grain independent, thus we have $\langle \delta \boldsymbol{C}^I \otimes \delta \boldsymbol{C}^I \rangle_\Theta = \langle \delta \boldsymbol{C}^g \otimes \delta \boldsymbol{C}^g \rangle_\Theta$. According to the far-field scattering amplitude presented in Section 2.2.3 and using the Born approximation by replacing the scattered field $\boldsymbol{u}^I(\boldsymbol{x})$ in each grain g^I of (2.72)-(2.74) by the unperturbed field $\boldsymbol{u}^{inc}(\boldsymbol{x})$ in the homogeneous medium, the scattering coefficient can finally be written as:

$$\begin{aligned} &\eta(\omega, \boldsymbol{e}_{scat}) \left(\frac{1}{V_{pc}} \frac{\left|\chi(k_{0L}, N_{dim})\right|^2}{\left(4\pi\rho^0 (v_{0l})^2\right)^2 \left|\boldsymbol{A}_{iL}\right|^2} \right)^{-1} \\ =&\sum_I \int_\Omega d\boldsymbol{x} \int_\Omega d\boldsymbol{x}' (\boldsymbol{k}_{0L})^2 \langle \gamma^I(\boldsymbol{x}) \gamma^I(\boldsymbol{x}') \rangle \boldsymbol{E}_1(\boldsymbol{x}) : \langle \delta \boldsymbol{C}^g \otimes \delta \boldsymbol{C}^g \rangle_\Theta : \boldsymbol{E}_1^*(\boldsymbol{x}') \exp\left(-ik_{0L} \boldsymbol{e}_{scat} \cdot (\boldsymbol{x} - \boldsymbol{x}')\right) \end{aligned} \tag{2.84}$$

with $\boldsymbol{E}_1(\cdot) = \boldsymbol{e}_{scat} \otimes \boldsymbol{e}_{scat} \otimes \boldsymbol{\varepsilon}(\boldsymbol{u}^{inc}(\cdot))$ and $\langle \gamma^I(\boldsymbol{x}) \gamma^I(\boldsymbol{x}') \rangle$ the spatial correlation function of two points $\boldsymbol{x}$ and $\boldsymbol{x}'$, which quantifies the possibility that they belong to the same grain g^I.

The second method proposed by Rose (1992) is based on the reciprocity theorem and states that $\eta(\omega, \boldsymbol{e}_{scat})$ can be obtained from the scattered noise signal amplitude $\delta S(\omega)$ defined by (2.61) in the following way:

$$\eta(\omega, \boldsymbol{e}_{scat}) = \frac{\beta \langle \delta S(\omega) \delta S^*(\omega) \rangle}{V_{pc}} \tag{2.85}$$

where $\langle\cdot\rangle$ is an average over all samples, β is a coefficient of proportionality and can be determined by the equivalence between the two methods (2.83) and (2.85) by considering some particular cases.

It is important to recall that, when the reciprocity theorem based method is used, it is required that $\langle \delta S(\omega)\rangle = 0$, so $\eta(\omega, \boldsymbol{e}_{scat})$ can be considered as the variance measure of noises. This requirement leads to $\langle \delta \boldsymbol{C}(\boldsymbol{x})\rangle = 0$ and implies the use of the Voigt average for the elastic tensor, denoted by $\langle \delta \boldsymbol{C}(\boldsymbol{x})\rangle^{\text{Voigt}}$, as the stiffness tensor for the reference medium. By substituting (2.63) into (2.85) we obtain:

$$\eta(\omega, \boldsymbol{e}_{scat})\left(\frac{\beta}{V_{pc}}\left(\frac{\omega}{4P_0(\omega)}\right)^2\right)^{-1} = \int_\Omega d\boldsymbol{x}\int_\Omega d\boldsymbol{x}' \boldsymbol{E}_2(\boldsymbol{x}) : \langle \delta \boldsymbol{C}(\boldsymbol{x}) \otimes \delta \boldsymbol{C}(\boldsymbol{x}')\rangle : \boldsymbol{E}_2^*(\boldsymbol{x}') \tag{2.86}$$

with $\boldsymbol{E}_2(\cdot) = \boldsymbol{\varepsilon}(\boldsymbol{u}^{1\to 2}(\cdot)) \otimes \boldsymbol{\varepsilon}(\boldsymbol{u}^{0;2\to 1}(\cdot))$. With the assumption on $\langle \delta \boldsymbol{C}\rangle$ and the analysis already presented concerning the term $\langle \delta \boldsymbol{C}(\boldsymbol{x}) \otimes \delta \boldsymbol{C}(\boldsymbol{x}')\rangle$ in (2.13), we finally obtain:

$$\eta(\omega, \boldsymbol{e}_{scat})\left(\frac{\beta}{V_{pc}}\left(\frac{\omega}{4P_0(\omega)}\right)^2\right)^{-1} = \int_\Omega d\boldsymbol{x}\int_\Omega d\boldsymbol{x}' \boldsymbol{E}_2(\boldsymbol{x}) : \langle \delta \boldsymbol{C}^g \otimes \delta \boldsymbol{C}^g\rangle_\Theta : \boldsymbol{E}_2^*(\boldsymbol{x}') W(\boldsymbol{r}) \tag{2.87}$$

Once more, under the Born approximation, the unknown fields $\boldsymbol{u}^{1\to 2}$ in (2.87) is replaced by $\boldsymbol{u}^{0;1\to 2}$, the solution of the same problem for $\boldsymbol{u}^{1\to 2}$ but in the homogeneous reference medium. In the case of backscattering, the two transducers 1 and 2 coincide and we have furthermore $\boldsymbol{u}^{0;1\to 2} = \boldsymbol{u}^{0;2\to 1}$, then theoretical formulas of η of backscattering can be obtained (see Equations (2.101) and (2.102)).

Finally to identify the constant of proportionality β, the equations (2.84) and (2.87) are compared under the Born approximation and in the particular case of backscattering with an incident wave that is assumed to be the following longitudinal plane wave with the propagating direction $\boldsymbol{e}_{inc} = -\boldsymbol{e}_{scat}$ and of amplitude U_L^0:

$$\boldsymbol{u}^{inc}(\boldsymbol{x}) = U_L^0 \boldsymbol{e}_{inc} \exp(ik_{0L}\boldsymbol{e}_{inc}\cdot\boldsymbol{x}) \tag{2.88}$$

By denoting $\boldsymbol{E}_{scat} = \boldsymbol{e}_{scat}\otimes\boldsymbol{e}_{scat}\otimes\boldsymbol{e}_{scat}\otimes\boldsymbol{e}_{scat}$, it is straightforward that $\boldsymbol{E}_1(\cdot) = iU_L^0 k_{0L}\boldsymbol{E}_{scat}\exp(ik_{0L}\boldsymbol{e}_{scat}\cdot(\cdot))$ and $\boldsymbol{E}_2(\cdot) = -(U_L^0 k_{0L})^2 \boldsymbol{E}_{scat}\exp(-2ik_{0L}\boldsymbol{e}_{scat}\cdot(\cdot))$, (2.84) and (2.87) then become:

$$\begin{aligned}&\eta(\omega, \boldsymbol{e}_{scat})\left(\frac{1}{V_{pc}}\frac{\left|\chi(k_{0L}, N_{dim})\right|^2 (k_{0L})^4}{\left(4\pi\rho^0 (v_{0L})^2\right)^2}\right)^{-1} \\ &= \int_\Omega d\boldsymbol{x}\int_\Omega d\boldsymbol{x}' \exp\left(-2ik_{0L}\boldsymbol{e}_{scat}\cdot(\boldsymbol{x}-\boldsymbol{x}')\right) W(\boldsymbol{x}-\boldsymbol{x}')\boldsymbol{E}_{scat} : \langle \delta \boldsymbol{C}^g \otimes \delta \boldsymbol{C}^g\rangle_\Theta : \boldsymbol{E}_{scat}\end{aligned} \tag{2.89}$$

$$\begin{aligned}&\eta(\omega, \boldsymbol{e}_{scat})\left(\frac{\beta}{V_{pc}}\left(\frac{\omega}{4P_0(\omega)}\right)^2 (U_L^0)^4 (k_{0L})^4\right)^{-1} \\ &= \int_\Omega d\boldsymbol{x}\int_\Omega d\boldsymbol{x}' \exp\left(-2ik_{0L}\boldsymbol{e}_{scat}\cdot(\boldsymbol{x}-\boldsymbol{x}')\right) W(\boldsymbol{x}-\boldsymbol{x}')\boldsymbol{E}_{scat} : \langle \delta \boldsymbol{C}^g \otimes \delta \boldsymbol{C}^g\rangle_\Theta : \boldsymbol{E}_{scat}\end{aligned} \tag{2.90}$$

The comparison between (2.89) and (2.90) finally results in the following formula of β, which depends also on the space dimension N_{dim}:

$$\beta(\omega, N_{dim}) = \left(\frac{4P_0(\omega)}{\omega}\right)^2 \frac{1}{(U_L^0)^2 (U_L)^2} \frac{\left|\chi(k_{0L}, N_{dim})\right|^2}{\left(4\pi\rho^0 (v_{0L})^2\right)^2} \tag{2.91}$$

where $(U_L^0)^4$ is replaced by $(U_L^0)^2(U_L)^2$ in order to preserve the generality when the Born approximation is not applied, especially for the formulas developed for the numerical approach presented in the next section.

In the 3D case, (2.91) gives the same result as obtained by Margetan et al. (Margetan et al. 2005). In the 2D case, it is necessary to add a multiplier equal to $\left|\chi(k_{0L}, N_{dim}=2)\right|^2 = 2\pi/k_{0L}$, which is inversely proportional to the wave number k_{0L}.

Finally introducing (2.91) in (2.85), we obtained the following formula of the scattering coefficient based on the reciprocity theorem in general cases, which is used to define our numerical measure strategy (Section 2.2.4.2):

$$\eta(\omega, \boldsymbol{e}_{scat}) = \frac{1}{V_{pc}} \frac{1}{(U_L^0)^2 (U_L)^2} \frac{\left|\chi(k_{0L}, N_{dim})\right|^2}{\left(4\pi\rho^0 (v_{0L})^2\right)^2} \left(\frac{4P_0(\omega)}{\omega}\right)^2 \langle \delta S(\omega) \delta S^*(\omega) \rangle \tag{2.92}$$

2.2.4.2 Numerical measure of the scattering coefficient

For the numerical measurement of the scattering coefficient using FE simulations, we propose to follow the procedure shown in Fig. 2.6.: Considering a single-phase, macroscopically isotropic and homogeneous polycrystalline medium with randomly oriented grains, for a given distribution of grain crystallographic orientations Θ, two FE transient simulations are performed in the time domain. The first one in the heterogeneous media of interest, by applying external loadings (prescribed displacements or surface forces) on the emitter part of boundary Σ_1, and by recording displacements on the receiver part of boundary Σ_2. The second one is performed with the homogeneous reference medium by interchanging roles played by Σ_1 and Σ_2. The rest of the boundary Σ remains free surface. With such a configuration, the unit vector directed from Σ_1 toward Σ_2 defines the scattering direction $\boldsymbol{e}_{scat}$ of interest. When Σ_1 coincides with Σ_2, the backscattering is considered.

Time-series signals of the wave displacement fields, incorporating the attenuation and the noise, are recorder by FE simulations. As the scattered solution $\boldsymbol{u}^{1\to 2}$ is completely given by the FE analysis for a given distribution Θ, there is no need to use the Born approximation. The Fourier transform in the frequency domain of FE data are then used to calculate the scattering coefficient as follows:

$$\eta(\omega, \boldsymbol{e}_{scat}, \Theta) = \frac{1}{V_{pc}} \frac{1}{(U_L^0)^2 (U_L)^2} \frac{\left|\chi(k_{0L}, N_{dim})\right|^2}{\left(4\pi\rho^0 (v_{0L})^2\right)^2} \left(\frac{4P_0(\omega)}{\omega}\right)^2 \delta S(\omega,\Theta) \delta S^*(\omega,\Theta) \tag{2.93}$$

where U_L and U_L^0 are respectively the displacement amplitudes of incident waves in both simulations. The amplitude of scattered signals $\delta S(\omega,\Theta)$ is calculated as integration over the boundary instead of the volume for the sake of numerical effectiveness:

$$\delta S(\omega,\Theta)=\frac{-i\omega}{4P_0(\omega)}\left(\left(\boldsymbol{T},\boldsymbol{u}^{0;2\to1}(\boldsymbol{x})\right)_{\Sigma_1}-\left(\boldsymbol{T}^0,\boldsymbol{u}^{1\to2}(\boldsymbol{x})\right)_{\Sigma_2}\right) \tag{2.94}$$

with the stress vectors $\boldsymbol{T}=\boldsymbol{\sigma}^{1\to2}\cdot\boldsymbol{n}$ on Σ_1 and $\boldsymbol{T}^0=\boldsymbol{\sigma}^{0;1\to2}\cdot\boldsymbol{n}$ on Σ_2 and the displacements $\boldsymbol{u}^{1\to2}$ on Σ_2 and $\boldsymbol{u}^{0;2\to1}$ on Σ_1 given by both simulations.

Finally performing FE simulations on the samples with different distributions Θ, the scattering coefficient of the polycrystalline medium is estimated in the following way:

$$\eta(\omega,\boldsymbol{e}_{scat})=\langle\eta(\omega,\boldsymbol{e}_{scat},\Theta)\rangle \tag{2.95}$$

For real experimental or numerical tests in a general case, it is difficult to estimate V_{pc} the volume of grains involved in the scattering. Two limits of V_{pc} can be defined:

A lower limit V_{pcMin} is the volume of the "straight beam" connecting the two surfaces Σ_1 and Σ_2 and it can be shown that a good estimate of V_{pcMin} reads as:

$$V_{pcMin}\approx\frac{1}{2}\left(\left|\Sigma_1\right|+\left|\Sigma_2\right|\right)min\left(v_{0L}t_f,d_{\Sigma_1\Sigma_2}\right) \tag{2.96}$$

with $\left|\Sigma_m\right|$ the area of Σ_1 ($m=1,2$), t_f the total observation time and $d_{\Sigma_1\Sigma_2}$ the distance between the centers of Σ_1 and Σ_2.

An upper limit V_{pcMax} is the volume of all grains crossed by the waves propagating from Σ_1 to Σ_2 for $t\le t_f$. In the case where the geometry of Ω is convex, a good estimate of V_{pcMax} is:

$$V_{pcMax}\approx V_{pcMin}+Vol\left(\Omega\cap\mathrm{Ellip}\left(\Sigma_1,\Sigma_2,t_f\right)\right) \tag{2.97}$$

where $\mathrm{Ellip}(\Sigma_1,\Sigma_2,t_f)$ denotes an ellipsoid with two equal semi-diameters and with the centers of Σ_1 and Σ_2 as the two foci on the third principal axis, whose length is equal to $v_{0L}t_f$. In the particular case of the measurement of the backscattering coefficient, Σ_1 and Σ_2 are completely superimposed, the calculation of V_{pcMin} does not change, while for V_{pcMax}, $\mathrm{Ellip}(\Sigma_1,\Sigma_2,t_f)$ becomes a sphere with the center of Σ_1 as its center and $v_{0L}t_f$ as diameter.

Then to compare numerical calculation and the theoretical estimation of the scattering coefficient, we propose to compare ηV_{pc} instead of η. That means the following numerical output:

$$\left(\eta(\omega,\boldsymbol{e}_{scat})V_{pc}\right)_{num}=\frac{1}{(U_L^0)^2(U_L)^2}\frac{\left|\chi(k_{0L},N_{dim})\right|^2}{\left(4\pi\rho^0(v_{0L})^2\right)^2}\left(\frac{4P_0(\omega)}{\omega}\right)^2\langle\delta S(\omega)\delta S^*(\omega)\rangle \tag{2.98}$$

is compared to the two theoretical lower and upper limits $\eta(\omega,\boldsymbol{e}_{scat})V_{pcMin}$ and $\eta(\omega,\boldsymbol{e}_{scat})V_{pcMax}$.

It is important to note that the proposed numerical procedure measures the actual reciprocity gap. Multiple scattering effects, if exist, are contained within the numerically calculated scattering coefficient. Therefore the numerical procedure breaks through the limitations of the use of the Born approximation and the single-scattering assumption made in the theoretical evaluation. It has the ability to simulate precisely the time-domain noise signals of elastic waves propagating in polycrystalline materials including complex physical mechanisms, such as multiple scattering and attenuation. Thus it has wider generality and higher accuracy than the analytical evaluation and can be applicable to complex media with strong scattering due to high degree of anisotropy, crystallographically textured microstructures or multi-phase microstructures, etc. Furthermore, the effectiveness of the procedure based on the reciprocity theorem is obvious, since it is much easier to record and integrate displacement and stress fields at the boundary rather than in the volume. This approach is versatile since the scattering coefficient in any given direction can be evaluated by only changing the position of the receivers.

2.2.4.3 2D and 3D analytical formulas for ultrasonic backscattering coefficient

In this section, we recall the analytical formulas of the backscattering coefficient for a single-phase, untextured and equiaxed polycrystalline medium without density variation in the 3D case and develop it in the 2D case by applying the theoretical results previously presented. For ease of analysis, it is assumed that the wave vector of the incident wave is in the direction $\boldsymbol{e}_{scat} = -\boldsymbol{e}_2$. When the backscattering is considered, we have $\boldsymbol{e}_{scat} = -\boldsymbol{e}_{inc}$. As only the longitudinal-to-longitudinal scattering is considered, the incident wave is assumed to be a longitudinal wave. The longitudinal-to-longitudinal backscattering coefficient is simply denoted as $\eta(\omega)$.

By substituting the two-point spatial correlation function expressed as in (2.23), an exponential function depending on the distance between the two points $r = |\boldsymbol{x} - \boldsymbol{x}'|$, into (2.89) or (2.90) and by applying the following change of variables:

$$\boldsymbol{s} = (\boldsymbol{x} + \boldsymbol{x}')/2,\ \boldsymbol{r} = \boldsymbol{x} - \boldsymbol{x}' \tag{2.99}$$

the following equation is straightforward:

$$\eta(\omega) = \frac{\left|\chi(k_{0L}, N_{dim})\right|^2}{\left(4\pi\rho^0 (v_{0L})^2\right)^2} \left(k_{0L}\right)^4 \langle \delta C_{2222} \delta C_{2222} \rangle \int_{\mathrm{R}} \exp(ik_{0L}\boldsymbol{r}\cdot\boldsymbol{e}_2 - \frac{2r}{\overline{d}}) d\boldsymbol{r} \tag{2.100}$$

Then considering the integration form (2.100) in the spherical coordinate and the cylindrical coordinate systems respectively for 3D and 2D cases, the analytical formulas for the longitudinal-to-longitudinal backscattering coefficient are obtained:

$$\eta^{3D}(\omega) = \frac{\langle \delta C_{2222} \delta C_{2222} \rangle}{\left(4\pi\rho^0 (v_{0L})^2\right)^2} \frac{\pi (x_0)^4}{\left(1 + (x_0)^2\right)^2 \overline{d}} \tag{2.101}$$

$$\eta^{2D}(\omega) = \pi\sqrt{(x_0)^{-2}+1}\,\eta^{3D}(\omega) \tag{2.102}$$

Concerning the correlation function of the elastic stiffness tensor, only $\langle \delta C_{2222} \delta C_{2222} \rangle$ is needed in the present work and is calculated using the first equation of (2.33) for the case of cubic symmetric crystallites.

Particular attention should be paid to the single-scattering assumption and the Born approximation used in the derivation of analytical expressions for the backscattering coefficient. They are expected to be good approximations on the condition that the inhomogeneity degree of polycrystals ξ is much less than unity. This fundamental assumption makes sure that the variation of elastic properties from crystallite to crystallite is small. Furthermore, the formulas of the backscattering coefficient are expected to be valid for the early time portion so that the scattering-induced attenuation is not significant (Han et al. 1997).

Finally 3D and 2D analytical curves of longitudinal-to-longitudinal backscattering coefficient versus frequency $f \in [0,16]$MHz for the polycrystalline material studied in this work are presented for three grain sizes of 80μm , 160μm and 320μm (Fig. 2.8.(a)). It is shown that the larger grains backscatter more energy at low frequency, whereas at high frequency, smaller grains backscatter more energy and the backscattering coefficient of the largest grain becomes constant. The scattering plateau can be attributed to the transition from the stochastic scattering region to the geometric one. Otherwise the comparison between the 3D and the 2D cases shows that the 2D case gives rise to larger backscattering coefficients than the 3D case due to the effect of the multiplier coefficient $\pi\sqrt{(x_0)^{-2}+1}$ and that the asymptotic value in high frequency range for the 2D case is π times the one for the 3D case. Finally as referred to (2.101), the differential backscattering cross section per crystallite ηd is independent of the grain size and a master curve is therefore obtained (Fig. 2.8.(b)).

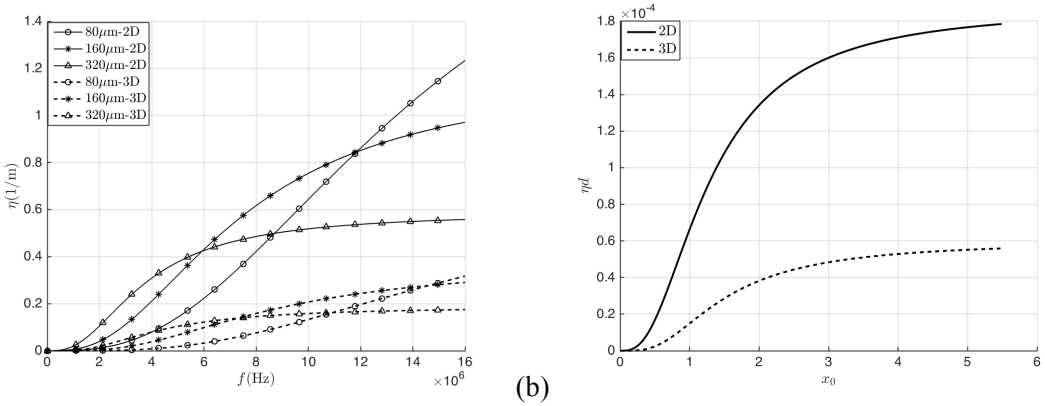

(a) (b)

Fig. 2.8. Analytical results of longitudinal-to-longitudinal backscattering coefficient for different grain sizes in the 3D and 2D cases (a) η vs. f, (b) master curves ηd vs. x_0 .

2.3 Conclusions

Theoretical and numerical approaches to evaluate the ultrasonic wave scattering in polycrystals have been presented in this chapter. More particularly, the following new contributions were proposed:

Firstly, analytical formulas of the longitudinal-to-longitudinal and longitudinal-to-shear wave scattering-induced attenuation for the incident longitudinal wave propagating in a single-phase, untextured polycrystalline microstructure containing equiaxed grains with a cubic symmetry are developed based on the Stanke-Kino unified theory in both 2D and 3D cases. These expressions are formulated based on both the Born approximation and the assumption that the displacement vector $\boldsymbol{U}$ of the quasi-longitudinal wave is parallel to the wave vector $\boldsymbol{k}$. They are good approximations only if the inhomogeneity degree ξ of the medium is much less than *1*. It is demonstrated that the attenuation for the longitudinal wave in the Rayleigh region is determined by the longitudinal-to-shear wave scattering, which is closely linked to the cross section of the scatter. It shows a fourth power dependence on frequency and a third power dependence on grain size in the 3D case and a third power dependence on frequency and a second power dependence on grain size in the 2D space. Whereas the longitudinal-to-shear wave scattering generated by the mode conversion dominates the attenuation in the stochastic region, which is a one-dimensional behavior and is dependent only on the averaged grain dimension in the wave propagation direction. Thus a second power dependence on frequency is observed for both 2D and 3D medium. The Rayleigh-to-stochastic transition region corresponds to the change of scattering mechanism transition, which occurs slightly earlier in the 2D space than that in the 3D model for a given grain size. The geometric region exceeds the limitation of our analytical predictions due to the significant attenuation.

Secondly, considering the equivalence of the reciprocity formulation and the isolated scatter model for the microstructural noise scattering based on weak-scattering approximation, an important coefficient of proportionality is given, which is proved to depend on spatial dimension, frequency, and material properties. The analytical formulas for the backscattering coefficient in 2D space are developed. Compared to the 3D case, it is shown that the Rayleigh-to-stochastic transition occurs earlier, the backscattering coefficient is quantitatively larger in the 2D case. Additionally, the asymptotic value in the geometric region in the 2D space is π times of the one in 3D space.

Thirdly, an original numerical procedure by FE modeling to evaluate the grain-noise scattering in an arbitrary direction based on the reciprocity theorem is proposed. It is applicable to complex media with strong scattering and it can provide a more complete theoretical model to understand complicated physical mechanisms of grain-noise scattering, including multiple scattering and the attenuation.

Chapter 3

Setting of FE model for elastic wave propagation in polycrystalline materials

FE simulations of ultrasonic wave propagation in polycrystalline materials presented in this work are performed by using an in-house software OOFE (Tie et al. 2003, Tie et al. 2010). The elastodynamic equations governing elastic wave propagation are solved in the time domain by an implicit solver based on a time-discontinuous space-time Galerkin method. Only 2D FE simulations are presented in this present work.

In this chapter, setting of FE model for investigation of grain size effects on ultrasonic attenuation and backscattering is first presented. Idealized single-phase, equiaxed and untextured polycrystalline microstructures with different unimodal grain sizes are defined. Unstructured FE meshes are used. Consideration on mesh convergence is given by analyzing effects of two important ratios: the ratio of grain size to mesh size and the ratio of wavelength to mesh size. The choice of methods for averaging elastic moduli to define the effective properties of a polycrystalline medium is discussed. Wavefronts of quasi-longitudinal waves, quasi-shear waves at different moments of wave propagation and time-series signals recorded at receivers are presented. The procedure for numerical quantification of ultrasonic attenuation and backscattering in both time and frequency domains is finally proposed.

3.1 Definition of 2D FE models of ultrasonic wave propagation

The 2D FE models used in the present work to calculate the attenuation and backscattering coefficients are shown in Fig. 3.1. The first one considers the polycrystalline material of interest (the grey part in Fig. 3.1.(a)) embedded in the homogeneous reference material (the white part in Fig. 3.1.(a)). The whole domain is chosen sufficiently large in order to avoid arrival on the receiver of waves reflected by the external lateral boundaries during the time interval of analysis. The second one (Fig. 3.1.(b)) considers the homogeneous reference material. The same FE mesh is used to discretize both heterogeneous and homogeneous reference domains.

The studied polycrystalline materials have an idealized theoretical microstructure with hexagonal grains. It is single phase with a cubic crystal symmetry. Crystallographic orientations of grains defined in terms of the Euler angles $\Theta(\varphi_1,\phi,\varphi_2)$, which define the anisotropic axis with respect to the global Cartesian basis, are randomly distributed by providing the following set up:

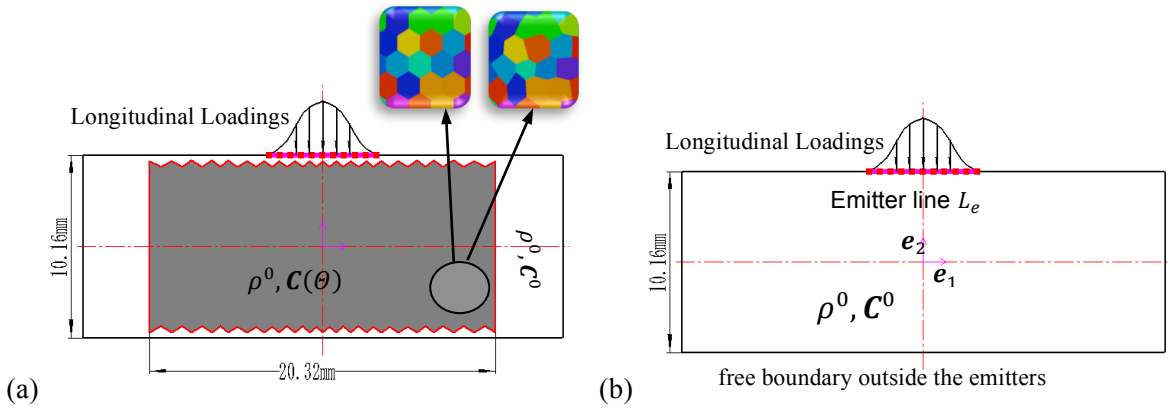

Fig. 3.1. Schematic representation of the 2D domain for FE models of (a) the heterogeneous polycrystalline medium; (b) the homogeneous reference medium.

$$\begin{aligned} \varphi_1 &= random[0,\ 2\pi[\\ \phi &= \mathrm{acos}(random[-1,\ 1]) \\ \varphi_2 &= random[0,\ 2\pi[\end{aligned} \tag{3.1}$$

In this work, the regular hexagonal grains are mainly considered. For a regular hexagonal grain, its grain size is defined as the diameter of its inscribed circle and denoted by H. The equivalent grain size defined as the diameter of the circular grain having the same grain surface is then $d = 1.05H$ FE models for the samples with single-size regular hexagonal grains, with three different grains sizes $H = 80\mu\mathrm{m}$, $160\mu\mathrm{m}$ and $320\mu\mathrm{m}$ are defined. For the three considered grain sizes, the polycrystalline domain is composed of respectively 35630, 8855 and 2125 randomly oriented hexagonal crystallites. For a given grain size, ten different random distributions of crystallographic orientations are considered.

Furthermore, to investigate if there exist numerical artifacts due to the use of the regular hexagonal grains, which results in regularly oriented grain boundaries, ten samples with irregular hexagonal grains, obtained by slight and random perturbation of regular hexagonal grain shape, are considered too. The crystallographic orientation distribution for ten samples with irregular grains are the same as those ten samples with regular grains. The equivalent grain size H for each irregular grain is calculated using the inscribed circle diameter of the hexagonal regular grain having the same grain surface. For one sample with irregular grains, Fig. 3.2. shows in blue the distribution of angles formed by grain boundaries with the horizontal axis and the distribution of grain size. Both distributions for samples composed of regular grains are also shown in Fig. 3.2. with red vertical lines. It reveals that microstructures with irregular hexagonal grains present a Gaussian grain size distribution with the unweighted average equal to the size of regular grain and a standard deviation equal to one. The distribution of the orientations of irregular grain boundaries is the sum of three Gaussian distributions with mean value respectively equal to the three orientations -90°, -30° and 30° of regular grain boundaries. Numerical results on these samples allow ruling out any suspicion of possible artifact due to the use of regular hexagonal grains for the numerical simulations (Section 4.1.3).

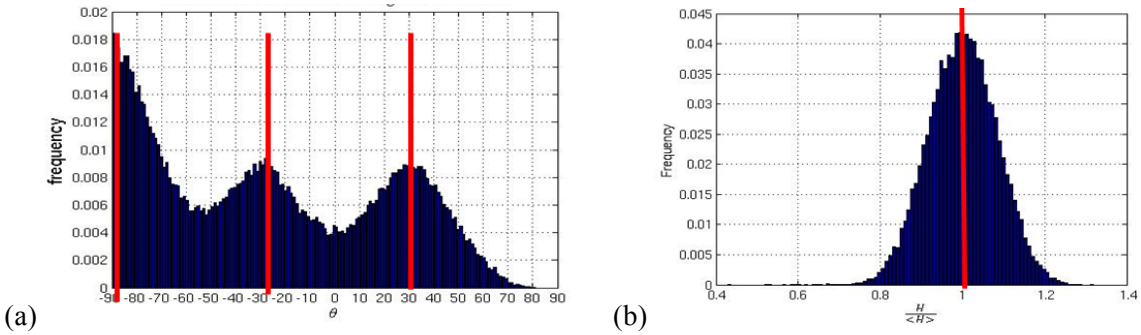

Fig. 3.2. Distributions of (a) grain boundary orientations w.r.t. the horizontal axis and (b) grain sizes: Blue Gaussian type distributions for microstructures with irregular hexagonal grains with $\langle H \rangle$=80μm ; Red vertical lines for microstructures with regular hexagonal grains with H=80μm.

Concerning the external loadings and the data recording, an emitter line L_e of 2.8mm length on the external top boundary of the studied domain is defined (Fig. 3.1.). Twenty-two uniformly distributed points are defined on L_e and serve as emitters and receivers. Ultrasonic waves are generated by applying a pressure loading $p(x,t)\boldsymbol{e}_2$ on L_e. For a given x, $p(x,t)\boldsymbol{e}_2$ is the sum of two Ricker signals varying in time within a period T_r, whose central peak frequency $f_c = 2/T_r$ is respectively equal to 5MHz and 10MHz. Each Ricker signal $ricker(x,t)$ reads as:

$$ricker(x,t) = \begin{cases} A_r(x)\left(1-2\pi^2 f_c^2\left(t-1/f_c\right)^2\right)\exp\left(-\pi^2 f_c^2\left(t-1/f_c\right)^2\right), & \text{for } 0 \le t \le 2/f_c \\ 0, & \text{for } t \ge 2/f_c \end{cases} \tag{3.2}$$

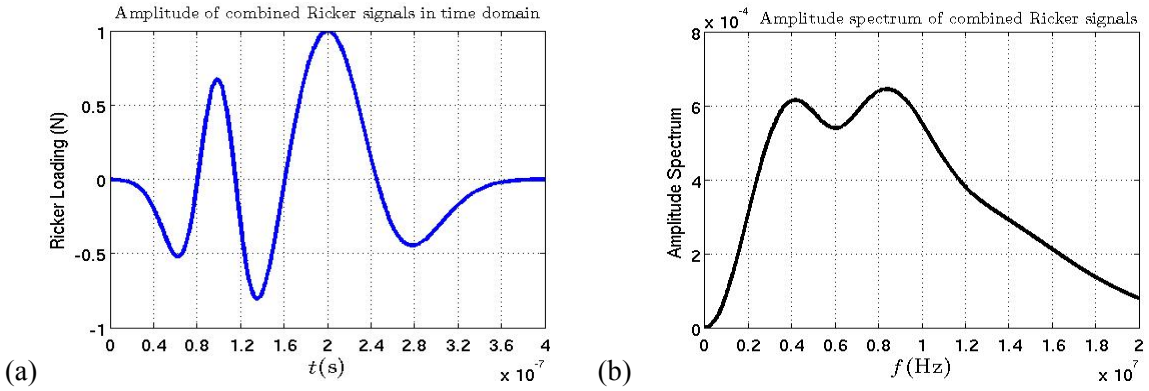

Fig. 3.3. Combined Ricker signal used as the external longitudinal loadings presented in both (a) time and (b) frequency domains

Furthermore in order to reduce effects of shear waves, which would be triggered when discontinuities in boundary conditions occur at the ends of the emitter line, the peak amplitudes $A_r(x)$ of both Ricker signals are chosen to have a Gaussian distribution along the emitter line. Thus the peak amplitudes of input signals smoothly decrease down to zero at the ends of the emitter, which is better suited to the free boundary condition imposed on the other side. Fig. 3.3. presents the external pressure loading used in the present work in both time and frequency domains.

Unstructured FE meshes using both triangular and quadrilateral finite elements have been used in the numerical simulations without significant differences. Hence only simulations using quadrilateral elements are presented here. An example of FE mesh of microstructures with the grain size of 320μm is presented in Fig. 3.4. and shows the great flexibility offered by the FEM to exactly model the grain boundaries.

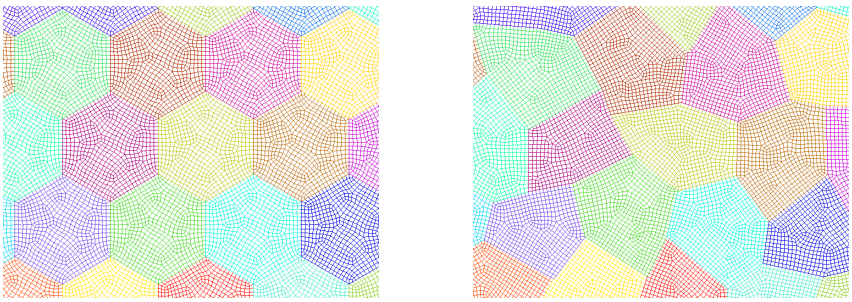

Fig. 3.4. FE meshes of microstructures composed of regular or irregular hexagonal grains of size 320μm .

3.2 Mesh convergence analysis

In order to account for the impedance variations between two adjacent grains and have a good representation of wave front, a sufficient number of elements included in one grain and in the shortest wavelength of interest is essential for the quality of numerical simulations (Shahjahan et al. 2014, Van Pamel et al. 2015). However, the computational cost increases greatly when the mesh becomes more

refined. To control the quality and optimize the efficiency, the mesh convergence analysis is of great importance.

For the mesh convergence analysis presented in this Section, FE models with all the three grain sizes of 80μm, 160μm and 320μm are used but they are only of half sizes of those described in Fig. 3.1 in order to reduce the computational cost. Different ratios of grain size to element size d/h are considered. The attenuation convergence is calculated as the measured attenuation α (defined in (3.5)) subtracted from the converged solution α_c obtained from the highest available density mesh, $(\alpha-\alpha_c)/\alpha_c$. The mesh convergence of ultrasonic backscattering is quantified by the following mechanical quantity $\varsigma(f)$:

$$\varsigma(f)=\left(\frac{\frac{1}{M}\sum_{j=1}^{j=M}\left|V_2^b(\boldsymbol{x}_j,f)\right|^2}{\frac{1}{M}\sum_{j=1}^{j=M}\left|V_2^i(\boldsymbol{x}_j,f)\right|^2}\right)^{1/2} \tag{3.3}$$

where the superscripts *b* and *i* denote respectively the backscattered noise and the incident signals and $V_2(\boldsymbol{x}_j,f)$ is the Fourier transform of the velocity component in the direction $\boldsymbol{e}_2$ recorded at the j^{th} probe $\boldsymbol{x}_j$. $\varsigma(f)$ is in fact a frequency-dependent coefficient calculated as the ratio of the rms velocity between the backscattered noise and the incident signals. It is associated to the percentage of the energy loss due to scattering in the backscattered direction. The backscattering mesh convergence is evaluated by $(\varsigma-\varsigma_c)/\varsigma_c$ with the converged solution ς_c obtained by the highest available density mesh of all studied FE models.

Fig. 3.5. and Fig. 3.6. present respectively the attenuation and backscattering mesh convergence for the frequency $f=10$MHz as a function of the number of elements per grain size d/h and a function of the number of elements per wavelength λ/h.

On the one hand, it is seen that for a sample with a smaller grain size, both the attenuation and the backscattering converges more rapidly with respect to the number of elements per grain size d/h (Fig. 3.5.(a) and Fig. 3.6.(a)). Indeed for a given ratio d/h, a larger number of elements per wavelength λ/h is obtained for the sample with a smaller grain size and thus results in less mesh scattering. At $f=10$MHz and for $d/h=10$, only the grain size of 80μm has converged for the threshold of 1%, which agrees with the results obtained by Van Pamel et al. (Van Pamel et al. 2015) and Shahjahan et al. (Shahjahan et al. 2014). Otherwise it is worth to remark that the errors for the grain size of 320μm are significantly higher than the other two grain sizes since this grain size is comparable to the studied wavelengths.

On the other hand, a sample with a smaller grain size converge less rapidly with respect to the number of elements per wavelength λ/h (Fig. 3.5 (b) and Fig. 3.6 (b)), because there are less elements per grain size for a given ratio λ/h. Our analysis concludes that there should be at least 20 elements per wavelength to ensure the beginning of a converging process.

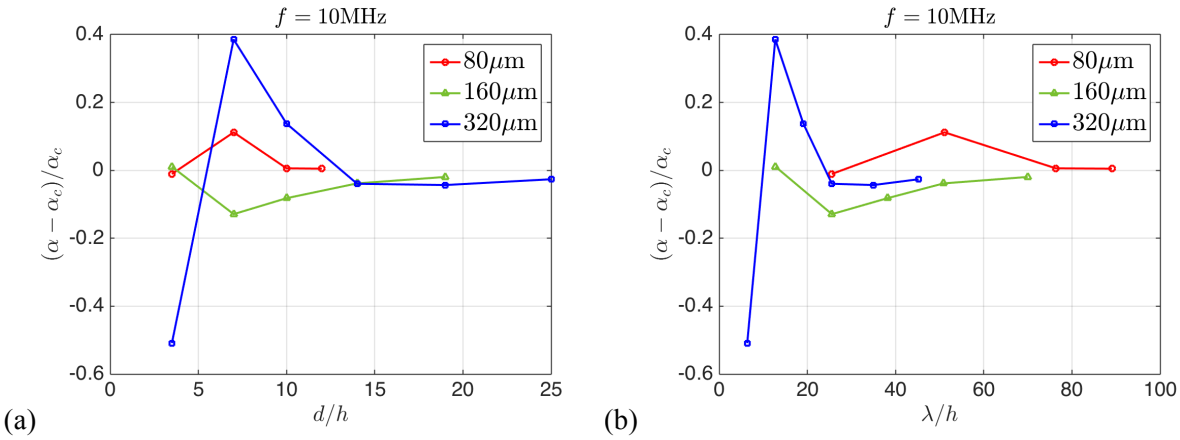

Fig. 3.5. Attenuation mesh convergence $(\alpha-\alpha_c)/\alpha_c$ w.r.t. (a) the number of elements per grain size d/h and (b) the number of elements per wavelength λ/h for three grain sizes for $f=10$MHz.

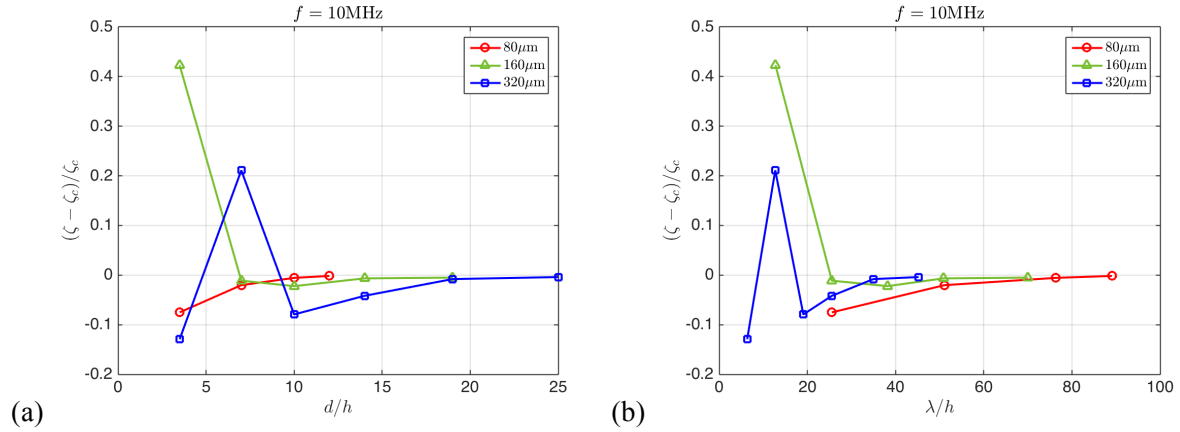

Fig. 3.6. Backscattering mesh convergence $(\varsigma-\varsigma_c)/\varsigma_c$ w.r.t. (a) the number of elements per grain size d/h and (b) the number of elements per wavelength λ/h for three grain sizes for $f=10$MHz.

Fig. 3.7. presents the attenuation and backscattering mesh convergence as a function of the number of elements per grain size d/h at six different frequencies for each of the three grain sizes. For a given ratio of d/h, it is observed that the lower the frequency is, the more rapid the convergence is because of a larger number of elements per wavelength λ/h.

The numerical simulations about grain size effects on ultrasonic wave propagation are performed using the FE meshes with $d/h=7$, 14 and 25 respectively for the three grain sizes of 80μm, 160μm and 320μm. Therefore according to our mesh convergence analysis, the attenuation coefficient is converged to at least 3% at all frequencies for the two larger grain sizes 160μm and 320μm (Fig. 3.7.(b) and (c)). Particular attention should be paid to the calculation error of the attenuation coefficient for the sample with the grain size of 80μm, which increases quickly with frequency and reaches to 23% at the highest frequency $f=16$MHz (Fig. 3.7. (a)). The backscattering coefficient is converged at least for the threshold of 7% at all frequencies and for all three grain sizes (Fig. 3.7.).

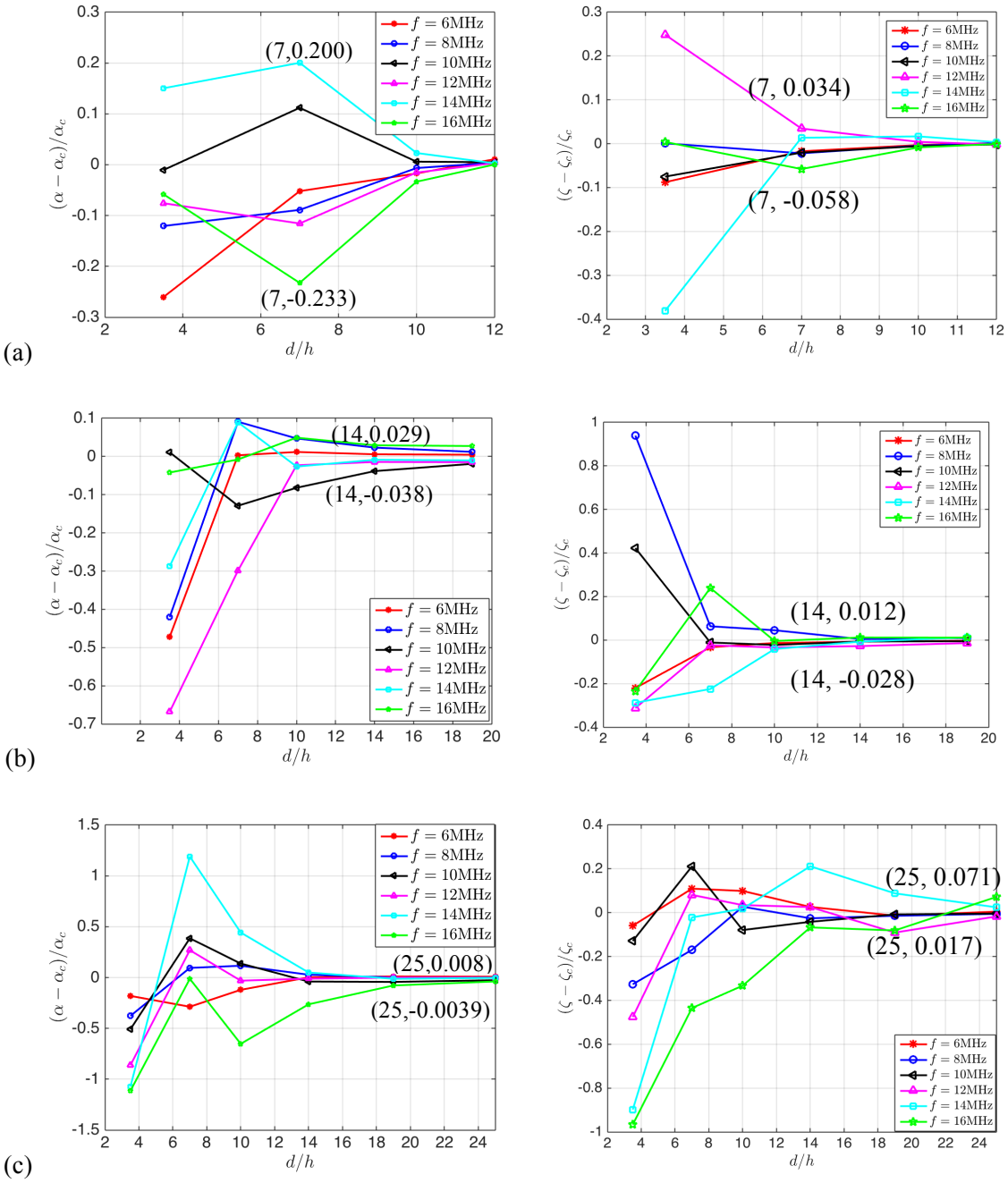

Fig. 3.7. Attenuation mesh convergence $(\alpha-\alpha_c)/\alpha_c$ (left) and backscattering mesh convergence $(\varsigma-\varsigma_c)/\varsigma_c$ (right) w.r.t. the number of elements per grain size d/h at six different frequencies for the grain sizes of (a) 80μm, (b) 160μm and (c) 320μm; The number of elements per grain size d/h of the FE meshes used for the numerical analysis presented in the Section 4 and their precisions are indicated for each grain size.

Limited by the ratio of wavelength to mesh size, the quality of FE simulations can be deteriorated in the frequency range $f>16$MHz. Therefore the valid frequency domain of our numerical simulations presented herein is no more than 16MHz. It can be concluded that the FE models used

herein are appropriately defined and adequate convergence is achieved in the measurement of amplitude attenuation and noise levels.

3.3 Ultrasonic phase velocity in polycrystals

In this section, different ways to calculate effective elastic properties and longitudinal wave phase velocities of the studied polycrystalline material are considered. Numerically estimated phase velocity is compared with the theoretical effective phase velocities. It allows determining which effective elastic tensor should be used as equivalent reference medium, and on the other hand validating our FE models in the term of quality of estimating the arrival time of waves.

Firstly three averages of elastic stiffness tensor classically defined by static homogenization studies to get effective elastic properties are considered. The Voigt average results in an upper bound of effective elastic stiffness tensors under the assumption of uniform strain, *i.e.* $\langle \boldsymbol{C}(\boldsymbol{x}) : \boldsymbol{\varepsilon}(\boldsymbol{x}) \rangle = \langle \boldsymbol{C}(\boldsymbol{x}) \rangle : \boldsymbol{\varepsilon}^0$, so $\langle \boldsymbol{C}(\boldsymbol{x}) \rangle^{\text{Voigt}} = \langle \boldsymbol{C}(\boldsymbol{x}) \rangle$. The Reuss average results in a lower bound by assuming a uniform stress state, *i.e.* $\langle \boldsymbol{C}^{-1}(\boldsymbol{x}) : \boldsymbol{\sigma}(\boldsymbol{x}) \rangle = \langle \boldsymbol{C}^{-1}(\boldsymbol{x}) \rangle : \boldsymbol{\sigma}^0$, so $\langle \boldsymbol{C}(\boldsymbol{x}) \rangle^{\text{Reuss}} = \langle \boldsymbol{C}^{-1}(\boldsymbol{x}) \rangle^{-1}$. A self-consistent (SC) average (Kube et al. 2015) gives an estimate between the Voigt and Reuss bounds, by calculating equivalent elastic properties when either the elastic stiffness tensor $\boldsymbol{C}(\boldsymbol{x})$ or the compliance tensor $\boldsymbol{C}^{-1}(\boldsymbol{x})$ is averaged over all possible orientations.

For a polycrystalline sample containing 2125 grains of the grain size $H = 320\mu\text{m}$, the effective elastic properties of the three different averages and the corresponding phase velocities $v_{0L} = \sqrt{\langle C_{2222} \rangle / \rho^0}$ of longitudinal waves propagating in the direction $\boldsymbol{e}_2$ are listed in Table 3.1. The phase velocities are somewhat different: Those given by the SC and Reuss averages are about 1.3% and 2.8% smaller than the one given by the Voigt average.

Secondly we can also calculate the effective longitudinal wave phase velocities as the Voigt or Reuss averages of the longitudinal wave phase velocities of all grains. Indeed, pure longitudinal and pure shear wave do not exist any longer in anisotropic materials, which means that the longitudinal wave modes are generally neither parallel nor perpendicular to the longitudinal wave vector. For a grain with a known orientation Θ, the longitudinal wave phase velocity $v_{qL}(\Theta)$ in the direction $\boldsymbol{e}_2$ can be determined by the largest eigenvalue of the acoustic tensor $\boldsymbol{e}_2 \cdot \boldsymbol{\Gamma} \cdot \boldsymbol{e}_2$. With the assumption of uniform propagation time in each grain, the Voigt averaged phase velocity is estimated by $\langle v_{qL}(\Theta) \rangle^{\text{Voigt}} = \langle v_{qL}(\Theta) \rangle$. On the other hand, taking the hypothesis of uniform chord length along the wave propagation direction in each grain, the Reuss averaged phase velocity is given by $\langle v_{qL}(\Theta) \rangle^{\text{Reuss}} = \langle 1 / v_{qL}(\Theta) \rangle^{-1}$. These two averages are also listed in Table 3.1. We remark that $\langle v_{qL}(\Theta) \rangle^{\text{Voigt}}$ and $\langle v_{qL}(\Theta) \rangle^{\text{Reuss}}$ are only less than 0.2% larger than the phase velocity corresponding to $\langle \boldsymbol{C}(\boldsymbol{x}) \rangle^{\text{Voigt}}$.

Properties		v_{0L} (m/s)	Elastic Constants		
			$\langle C_{2222}\rangle$ (GPa)	$\langle C_{1122}\rangle$ (GPa)	$\langle C_{2323}\rangle$ (GPa)
$v_{0L}=\sqrt{\langle C_{2222}\rangle^{\mathrm{av}}/\rho^0}$	av = Voigt	5878	153.0	100.0	26.5
	av = SC	5800	149.0	102	23.9
	av = Reuss	5714	144.6	104.6	20.0
$v_{0L}=\langle v_{qL}(\Theta)\rangle^{\mathrm{av}}$	av =Voigt	5889	/	/	/
	av = Reuss	5884	/	/	/

Table 3.1. Effective elastic properties and phase velocities of longitudinal waves of a polycrystalline sample containing 2125 grains of size 320μm

The numerical evaluation of phase velocities is based on a spectral autocorrelation method with numerical data recorded at 11 inner probes placed 2mm below the emitter-receiver line L_e. Fig. 3.8. shows the comparison between numerical and analytical estimates of phase velocities of the longitudinal wave in the same polycrystalline sample containing 2125 grains of size 320μm. The numerical result is consistent with three theoretical predictions given by $\sqrt{\langle C_{2222}\rangle^{\mathrm{Voigt}}/\rho^0}$, $\langle v_{qL}(\Theta)\rangle^{\mathrm{Voigt}}$ and $\langle v_{qL}(\Theta)\rangle^{\mathrm{Reuss}}$. This confirms the relevancy of the classical choice of using the Voigt average to determine the equivalent homogenized elastic tensor and wave velocities in polycrystalline materials with randomly oriented grains. The Voigt average stiffness tensor is given in Table 2.1.

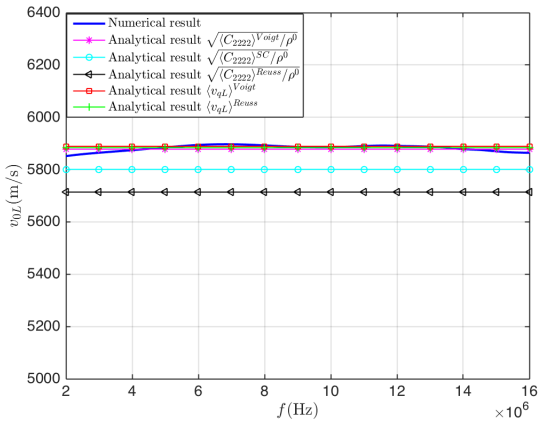

Fig. 3.8. Comparison between numerical and theoretical estimates of phase velocities of the longitudinal wave in a polycrystalline sample containing 2125 grains of size 320μm.

3.4 Post-processing of numerical ultrasonic data

FE modeling is able to simulate the time-series ultrasonic wave signals of any point of interest, including the complex physics phenomena such as multiple-scattering as well as the amplitude attenuation. Two kinds of post-processing of FE data are used here: Helmholtz's decomposition of displacement fields and calculation of the attenuation and backscattering coefficients.

3.4.1 Helmholtz's decomposition of displacement fields

The first kind of post-processing of FE data is based on the Helmholtz's decomposition: Displacement fields are decomposed into two vector fields, the one curl-free and the other divergence-free. In the case of isotropic elastic wave analysis, the former is referred to as the longitudinal wave component and the latter as the shear wave component. Therefore for any wave displacement field $\boldsymbol{u}$, its divergence $\operatorname{div}\boldsymbol{u}$ displays longitudinal (or quasi-longitudinal in anisotropic media) wavefronts and its curl $\mathbf{rot}\,\boldsymbol{u}$ displays shear (or quasi-shear in anisotropic media) wavefronts. In the general case of anisotropic elasticity, $\operatorname{div}\boldsymbol{u}$ vanishes no longer on the quasi-shear wavefronts and $\mathbf{rot}\,\boldsymbol{u}$ vanishes no longer on the quasi-longitudinal wavefronts. Effectively, $\operatorname{div}\boldsymbol{u}$ of the quasi-shear wave and $\mathbf{rot}\,\boldsymbol{u}$ of the quasi-longitudinal wave increase with the anisotropy degree of the medium. Therefore, for a polycrystalline medium with a low anisotropy degree, we can keep using $\operatorname{div}\boldsymbol{u}$ and $\mathbf{rot}\,\boldsymbol{u}$ to approximately display quasi-longitudinal wavefronts and quasi-shear wavefronts.

As an example, Fig. 3.9. shows wavefronts of quasi-longitudinal waves and quasi-shear waves in a polycrystalline sample with the grain size $H = 80\mu\text{m}$ at three different moments. We observe a principal quasi-longitudinal wavefront ($\operatorname{div}\boldsymbol{u}$ predominant) propagating in the direction $-\boldsymbol{e}_2$ at first and then in the opposite direction after being reflected by the bottom of the sample. Behind the principal quasi-longitudinal wavefront, scattered noise in terms of $\operatorname{div}\boldsymbol{u}$ is easily recognized. Fig. 3.9. shows also two principal quasi-shear wavefronts ($\left|\mathbf{rot}\,\boldsymbol{u}\right|$ predominant). The faster one propagates together with the principal quasi-longitudinal wavefront because $\mathbf{rot}\,\boldsymbol{u}$ vanish no longer on the quasi-longitudinal wave fronts, but also due to the conversion from quasi-longitudinal waves to quasi-shear waves every time when quasi-longitudinal waves encounter a grain boundary. The slower one propagates with the velocity of quasi-shear waves, nearly half of the velocity of quasi-longitudinal waves. It is obvious that the quasi-shear wave modes seem to be more sensitive to grain boundaries than the quasi-longitudinal wave modes and result in high-level noises in terms of $\left|\mathbf{rot}\,\boldsymbol{u}\right|$.

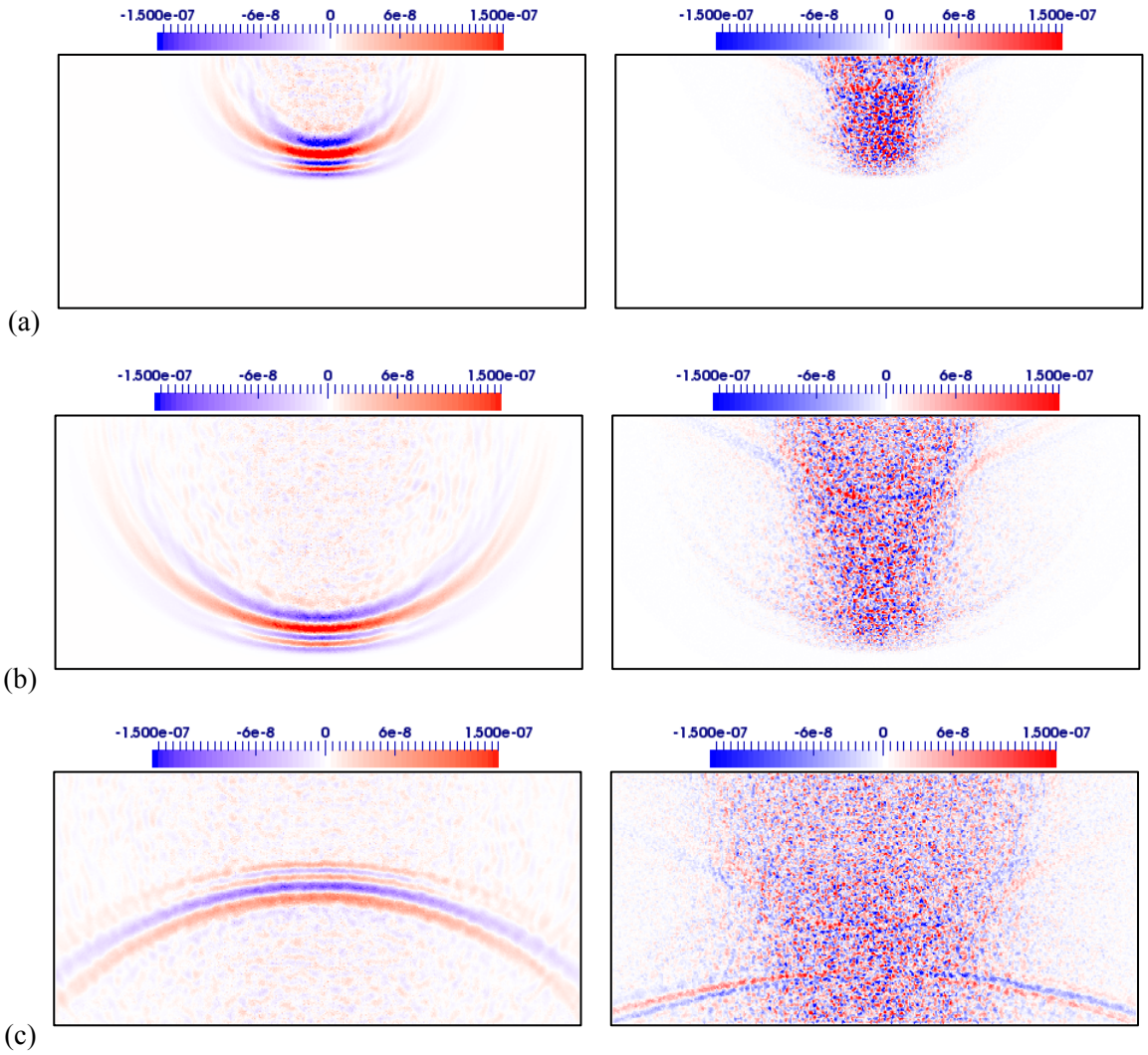

Fig. 3.9. Longitudinal (left) and shear (right) wave propagation in a polycrystalline sample with grain size of 80μm at different moments (a) $t = 0.84\mu$s , (b) $t = 1.64\mu$s and (c) $t = 2.84\mu$s .

3.4.2 Numerical calculation of ultrasonic attenuation coefficients

The post-processing for the calculation of the attenuation coefficients is conducted in both time and frequency domains. Since only the attenuation for the longitudinal wave is of interest, the velocity components v_2 in the direction $\boldsymbol{e}_2$ recorded at the 22 receivers on the emitter-receiver line L_e are used.

As an example, Fig. 3.10. illustrates the normalized velocities $v_2/max(v_2)$ observed at the 10^{th} receiver located at the middle of L_e for a polycrystalline sample with grain size of 80μm (the red line) and for the homogeneous reference medium (the black line). The first and second peaks on both curves correspond to the incident signals and the echo signals reflected by the bottom side of the sample. For the polycrystalline sample, perturbations of much smaller amplitude than incident and echo signals are in fact backscattered noise signals, which are absent in the reference case.

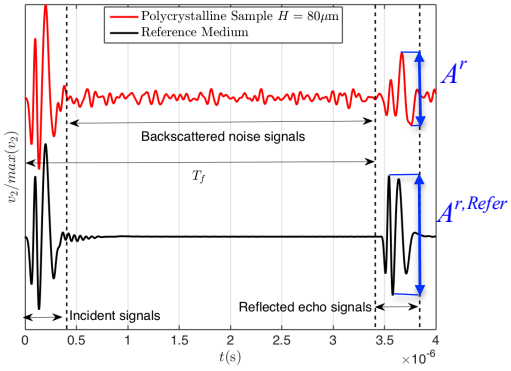

Fig. 3.10. Normalized velocity in $\boldsymbol{e}_2$ direction recorded at the 10th receiver in both polycrystalline (upper curve) and reference media (lower curve)

For a non-plane wave propagating in the studied heterogeneous medium, the amplitude attenuation of elastic wave recorded by FE simulations is decomposed into two parts: the scattering-induced attenuation and the attenuation caused by the geometrical spreading of wavefront. The latter is only associated with the sample geometry and can be measured within the equivalent homogeneous polycrystalline sample in the absence of scattering. Herein, to eliminate the attenuation due to the geometrical spreading of wavefront, comparison of reflected echo signals between the studied medium and the equivalent homogeneous medium is made for quantification of the scattering-induced attenuation in both time and frequency domains.

3.4.2.1 Calculation in the time domain

The temporal attenuation level is usually estimated by the peak-to-peak amplitude ratio of the time domain reflected echo signals to the incident signals. The attenuation per unit length, expressed in the unit "dB/mm" is usually expressed as (Thebault 2009, Tie 2010):

$$\alpha = -\frac{5}{D}\ln\left(\frac{\sum_{j=1}^{j=M} A^r(\boldsymbol{x}_j)}{\sum_{j=1}^{j=M} A^{r;Refer}(\boldsymbol{x}_j)}\right) \tag{3.4}$$

where M is the total number of the receiver probes, the superscripts r and *Refer* represent respectively the reflected echoes and the homogeneous reference material, $A^r(\boldsymbol{x}_j)$ (as shown in Fig. 3.10.) is the peak-to-peak amplitude of velocity at the receiver $\boldsymbol{x}_j$ in the averaged propagation direction for reflected echo signals. D is the wave propagation distance just before the arrival of reflected echoes at the receivers.

3.4.2.2 Calculation in the frequency domain

Discrete Fourier Transform (DFT) is used to decompose the time-series signals into the frequency domain. The ultrasonic attenuation for a given frequency f can be measured by (Thebault 2009, Tie 2010):

$$\alpha(f) = -\frac{10}{D}\ln\left(\frac{\sum_{j=1}^{j=M}\left|V^{r}(\boldsymbol{x}_j,f)\right|^2}{\sum_{j=1}^{j=M}\left|V^{r;Refer}(\boldsymbol{x}_j,f)\right|^2}\right)^{1/2} \tag{3.5}$$

where $V^r(\boldsymbol{x}_j,f)$ is the amplitude spectrum of the time-series reflected echo signals in the wave propagation direction recorded at the j^{th} probe $\boldsymbol{x}_j$ by DFT. The constant 10 is for the unit conversion from Neper (Np) to decibel (dB). It is possible to measure the amplitude attenuation by the displacement or the velocity of several receivers. The choice of the velocity is privileged because the quantity considered here $\sum_j\left|V_j^r(f)\right|^2$ is proportional to the kinetic energy. Using the virial theorem, it is recognized that the total energy density is equal, on suitable temporal or spatial average, to twice the kinetic energy density (Weaver 1990). Thus, $\alpha(f)$ is associated to a percentage of the total energy loss due to scattering.

3.4.3 Numerical calculation of ultrasonic backscattering coefficients

The noise signals during a time period T_f (Fig. 3.10.) are considered for numerical calculation of ultrasonic backscattering coefficients in both time and frequency domains, where T_f is the arrival time of the reflected echoes at the receivers.

3.4.3.1 Calculation in the time domain

A broadband time-series noise signal can be decomposed into a number of discrete frequencies, and it is of more interest to quantify the contribution of a given frequency f to the temporal backscattering level. For a given frequency f, the standard deviation of noise levels is defined as the rms positional average of the difference between the observed noise signal and the positional averaged noise level (Margetan et al. 1994):

$$n_{rms}(t,f) = \left(\frac{1}{10\times M}\sum_{j=1}^{10\times M}\left(v_2^b(\boldsymbol{x}_j,t,f) - b(t,f)\right)^2\right)^{1/2} \tag{3.6}$$

with

$$b(t,f) = \frac{1}{10\times M}\sum_{j=1}^{10\times M} v_2^b(\boldsymbol{x}_j,t,f) \tag{3.7}$$

where $10\times M$ means the average is taken over all receivers and over all the ten samples, so we have in fact 220 measures. $v_2^b(\boldsymbol{x}_j,t,f)$ is calculated by applying a frequency filtering, corresponding to the frequency f, to the velocity component $v_2^b(\boldsymbol{x}_j,t)$ in $\boldsymbol{e}_2$ direction of the noise signal recorded at the j^{th} receiver $\boldsymbol{x}_j$ (Ram 1988). The mean value $b(t,f)$ would be zero if the total number of measures, equal

to $10\times M$ in the present work, is sufficiently large. To eliminate the dependence of the noise level on the incident power, the normalized rms noise level $N_{rms}(t,f)$ at the moment t for a given frequency f is defined (Margetan et al. 1994):

$$N_{rms}(t,f)=n_{rms}(t,f)\big/E_{max}(f) \tag{3.8}$$

where E_{max} is taken equal to the half of the peak-to-peak amplitude of the incident signals for the frequency f.

3.4.3.2 Calculation in the frequency domain

As discussed in Section 2.2.4.2, the numerical calculation of ultrasonic backscattering coefficients in the frequency domain is performed by (2.98). Within the framework of the reciprocity theorem, both the prescribed external longitudinal loadings and the velocity components v_2 in the direction $\boldsymbol{e}_2$ recorded at the 22 receivers on the emitter-receiver line L_e are used. The comparison between the theoretical and the numerical calculations requires the volume of the involved polycrystalline microstructure to be defined. A minimum limit and a maximum limit, V_{pcMin} and V_{pcMax}, are proposed in equations (2.96) and (2.97). In the 2D case, these are in fact surface areas, S_{pcMin} and S_{pcMax}. According to (2.96) and (2.97), S_{pcMin} and S_{pcMax} respectively correspond to the pink rectangular area and the green semi-circular area shown in Fig. 3.11., with the arrow pointing to the receivers representing the propagation direction of the scattered wave and the other arrow representing the propagation direction of the incident wave. Comparing Fig. 3.9.(b) and Fig. 3.11., it is interesting to point out that the minimum and maximum limits, S_{pcMin} and S_{pcMax}, more likely correspond to the active grain volumes of respectively longitudinal-to-shear wave scattering and longitudinal-to-longitudinal wave scattering.

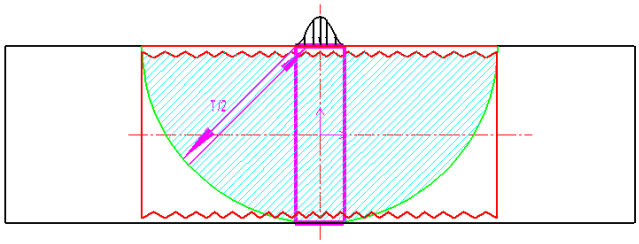

Fig. 3.11. Minimum and maximum limits S_{pcMin} and S_{pcMax} of polycrystalline surface in which backscattering occurs during the analysis period T_f.

3.5 Conclusions

In this chapter, FE models are first defined for a single-phase, untextured polycrystal with one-size regular hexagonal grains of cubic symmetry. The microstructure comprising irregular hexagonal grains with a normal grain size distribution is then considered. Several grain sizes and different random spatial distributions of crystallographic orientation for each size are considered. Mesh convergence analysis is carried out and it is found that at least 10 elements per grain size and 20

elements per wavelength are necessary to guarantee the calculation convergence. Furthermore, it has been shown that the numerical measured phase velocity of the longitudinal wave is coherent with the one measured by the analytical approach using the Voigt average to determine the equivalent homogenized elastic tensor for randomly-oriented medium. Concerning the post-processing of FE data, wavefronts of quasi-longitudinal waves and quasi-shear waves at different moments are presented. The longitudinal and shear scattered noise waves are respectively observed, with the latter generated by the longitudinal-to-shear wave mode conversion. Numerical procedures to calculate ultrasonic attenuation and backscattering coefficients in both time and frequency domains are finally proposed.

Chapter 4
Numerical results and discussions

Polycrystals are composed of anisotropic grains and each grain has its own various crystallographic orientation, shape and dimension. The grain-to-grain variation of crystallographic and morphological characteristics and the anisotropy degree of each crystallite determine the inhomogeneity degree of the medium at the scale of polycrystalline microstructure, as well as its macroscopic properties such as the crystallographic texture. They accordingly rule ultrasonic scattering phenomena at grain boundaries, thereby it is believed that the polycrystalline microstructure can be characterized by inversion of data of the scattering-induced attenuation and scattered noise signals.

In this chapter, grain size effects on the ultrasonic wave attenuation and backscattered noises in both unimodal and bimodal polycrystals are numerically quantified by using 2D FE modeling. Firstly, single-phase, untextured polycrystals composed of equiaxed grains with a unimodal size distribution are investigated. Comparisons between the 2D theoretical predictions and the numerical measurements for ultrasonic attenuation and backscattering coefficients are conducted to validate the numerical evaluation procedure proposed in Chapter 2. Further considerations on crystallographic orientation distribution effects and grain shape effects are made and as an original result, effects of the Born approximation on the theoretical prediction of the backscattering coefficient are numerically evaluated. Then, ultrasonic wave scattering is simulated in single-phase, untextured polycrystals composed of equiaxed grains with bimodal grain sizes, for which no theoretical model exists. Effects of several microstructural parameters on ultrasonic wave attenuation and backscattered noises are considered: the volume fraction ratio between the smaller and the larger grains, the location distribution of the larger grains including random and isolated distributions, crystal clusters of the larger grains in the matrix of the smaller grains and banded microstructures. Theoretical analysis concerning effects of the spatial correlation function is further conducted to establish a quantitative relationship of ultrasonic attenuation and backscattering between the unimodal and bimodal microstructures.

4.1 Ultrasonic wave scattering in polycrystals with unimodal grain size

Single-phase and untextured polycrystals comprising equiaxial grains of cubic-symmetry with a unimodal grain size distribution are regarded as a classical case in the theoretical investigation of ultrasonic wave scattering (Stanke et al. 1984, Weaver 1990, Rose 1992). This relatively simple microstructure is first considered in our FE modeling. Different grain sizes are studied and for each grain size, polycrystals with single-size regular hexagonal grains and irregular hexagonal grains of normal size distribution are considered (see Section 3.1). Numerical evaluation for grain size effects on ultrasonic attenuation and backscattering coefficients are subsequently presented, which are further compared with analytical predictions to validate the proposed numerical evaluation approaches. Effects of the multiple scattering-induced attenuation on the quantification of the backscattering coefficient are evaluated, to gain an insight into the validity range of the Born approximation.

Even if the number of grains is enough to obtain an isotropic material (no crystallographic texture), the grain boundary misorientation distribution can be very different between two different polycrustalline microstructures. Since the wave attenuation and the backscattering are very sensitive to the grain boundary misorientation distribution, and in order to keep the sample size small enough, it is chosen to average the simulations on ten different samples with the same set of crystallographic orientations, but with different spatial distributions of them. Our numerical results presented in the present chapter show that this choice seems to give sufficient statistics of the grain boundary misorientation distribution for measuring the attenuation, but not enough for evaluating backscattered noises.

4.1.1 Numerical evaluation of grain size effects on ultrasonic attenuation

Numerical simulations in rectangular polycrystalline samples of dimension $10.16\text{mm}\times 20.32\text{mm}$ (Fig. 3.1.) with three grain sizes of $80\mu\text{m}$, $160\mu\text{m}$ and $320\mu\text{m}$ are first carried out. Considering the ratios of the three grain sizes to involved wavelengths ranging from $375\mu\text{m}$ to $3000\mu\text{m}$ (the correponding frequency range is between 2-16MHz defined by the external loading presented in Section 3.1), scattering behaviors in the stochastic scattering region and the Rayleigh-to-stochastic transition region are supposed to be observed. Otherwise, to further include the Rayleigh scattering region, a smaller grain size of $20\mu\text{m}$ is considered with ratios of grain size to wavelengths x_0 less than 0.35. Comparison of the ultrasonic attenuation coefficients for four grain sizes between the numerical results and the 2D analytical predictions developed in Section 2.1.3 is further discussed.

However, limited by the ratio of grain size to element size d/h and the enormous quantity of crystallites (about 570,000 grains), the computational cost is considerably increased for the grain size of $20\mu\text{m}$. Thus, a sample with reduced dimensions $5.08\text{mm}\times 10.16\text{mm}$ is used. It is composed of about 142,000 grains, which are enough for a good representation of an untextured polycrystalline medium. Nevertheless some cautions must be taken in analyzing results obtained in the reduced sample. Firstly,

as the dimension of sample is reduced, accordingly the total time interval of analysis is reduced, leading to reduced sampling rate in frequency domain. Therefore, contrary to the unreduced sample for which the lowest frequency of confidence is equal to 2MHz, it is equal to 4.5MHz for the reduced sample used for the grain size of $20\mu\text{m}$. Secondly, as discussed in Section 3.2, numerical calculations of ultrasonic attenuation and backscattering converge at a smaller number of d/h for a sample with a smaller grain size. In the present work, the ratio d/h is set to be 3.5 for the grain size of $20\mu\text{m}$ ($d/h = 7, 14, 25$ for the grain sizes of $80\mu\text{m}$, $160\mu\text{m}$ and $320\mu\text{m}$, respectively), and the calculation converges for an acceptable threshold of 5.5%. Finally, we note that only two samples with distinct spatial distributions of crystallographic orientations are considered for this grain size since the calculation is more time-consuming.

4.1.1.1 Grain size effect

Numerical estimations for the ultrasonic attenuation coefficient of the longitudinal wave are presented successively in the frequency domain and in the time domain in this part.

The numerically measured attenuation coefficients in time domain for four different grain sizes are shown in Table 4.1.. It is seen that the attenuation increases with the grain size from $20\mu\text{m}$ to $160\mu\text{m}$. It is coherent with the analytically predicted variation tendency of attenuation with grain size in the Rayleigh domain (2.28). Whereas the attenuation of the largest grain size $320\mu\text{m}$ is inbetween that of the grain size $80\mu\text{m}$ and $160\mu\text{m}$. In fact, the analysis in the time and frequency domains is correlated. A broadband time signal can be decomposed into a number of discrete frequencies, and the contribution of each frequency to the temporal attenuation level can be quantified by the Fourier analysis (Fig. 4.1.). Referring to Fig. 4.1., at frequencies $f > 6\text{MHz}$, the attenuation coefficient for the grain size of $320\mu\text{m}$ is quantitatively smaller than that of grain size of $160\mu\text{m}$. It is coherent with the comparison of numerically measured attenuation level between the two grain sizes in the time domain.

Grain size	$20\mu\text{m}$	$80\mu\text{m}$	$160\mu\text{m}$	$320\mu\text{m}$
α (dB/mm)	0.028	0.118	0.222	0.141

Table 4.1. Ultrasonic attenuation in time domain for polycrystalline titanium with different grain sizes

Numerical measures of the longitudinal wave attenuation as a function of frequency for the four different grains sizes are shown in Fig. 4.1.. For each grain size, it is measured by the average response over different samples. For a given grain size, the attenuation coefficient increases as frequency then gradually becomes insensitive to high frequencies, fluctuating around a steady level in high frequency region. Both the increase rate of attenuation as frequency and the transition frequency to the plateau are dependent on the grain size. It is observed that the larger the grain size, the earlier the transition to the plateau. Specifically, the attenuation of sample with the largest grain size is insensitive to frequency in the region $8\text{-}16\text{MHz}$ and shows lower attenuated energy than the grain sizes

of 80μm and 160μm. Particularly, in the whole frequency region of interest, the attenuation in the microstructure with grain size of 20μm increases continuously and keeps the lowest level among these four grain sizes. The transition point to a plateau is not observed. These evolutions with frequency make difficult a simple comparison between different grain sizes. It is noted that the attenuation increases with the increasing grain size in low frequency region 2-6MHz, and on the contrary, the attenuation decreases as the increase of grain size from 80μm to 320μm in the high frequency region 13-16MHz.

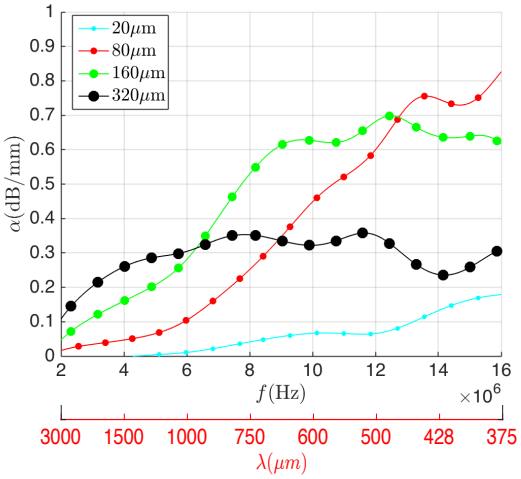

Fig. 4.1. Numerical estimations of the attenuation coefficient versus frequency for a longitudinal wave in polycrystalline titanium with four different grain sizes

Numerical estimations of normalized attenuation coefficient per crystallite versus normalized frequency for a longitudinal wave in polycrystalline titanium with four different grain sizes using both linear and logarithmic scales are presented in Fig. 4.2.. As predicted theoretically in (2.28) and (2.29), these master curves are supposed to be independent of grain size $\bar{d}$.

Fig. 4.2.(a) shows that the numerical estimations of $\alpha\bar{d}$ as a function of x_0 for four different grain sizes are roughly superimposed. It is noticed that the attenuation per crystallite increases with normalized frequency x_0 at low frequencies where $x_0 < 2$. Furthermore, the attenuation per crystallite reaches a plateau with oscillations at high frequencies where $x_0 > 2$, which is not consistent with the analytical prediction as shown in Fig. 4.2.(b).

With regard to the comparison between the 2D analytical prediction deduced from the Stanke-Kino model (Section 2.1.3) and the numerical results for the four grain sizes, the overlaps of the latter are in good agreement with the analytical master curve, at least up to frequency $\log_{10}(x_0) < 0.3$ ($x_0 < 2$) (Fig. 4.2.(b)). A third power law dependence on frequency characterizing the Rayleigh scattering region is confirmed for $\log_{10}(x_0) < -0.5$ ($x_0 < 0.3$). For intermediate frequencies $-0.5 < \log_{10}(x_0) < 0.3$ ($0.3 < x_0 < 2$), transition from the Rayleigh scattering region to stochastic scattering region is also confirmed by the numerical results, however within a shorter frequency interval. Indeed the Rayleigh-

to-stochastic transition is characterized by two successive humps on the theoretical curve, only the first concave hump is recovered by the numerical results. Afterwards, instead of obtaining close to the first power law (see Fig. 2.4.) characterizing the second convex hump of the Rayleigh-to-stochastic transition as analytically predicted, a plateau with slight oscillations is observed for high frequencies $0.3 < \log_{10}(x_0) < 0.74$ ($2 < x_0 < 5.5$).

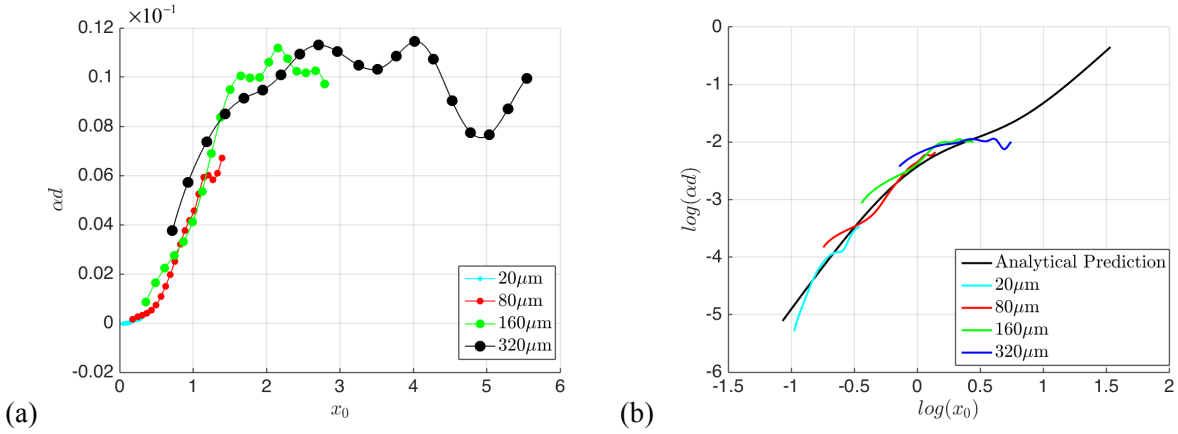

Fig. 4.2. Numerical estimations for normalized attenuation coefficient per crystallite versus normalized frequency for a longitudinal wave in polycrystalline titanium with four different grain sizes: (a) $\alpha\bar{d}$ as a function of x_0, (b) $\log_{10}(\alpha\bar{d})$ as a function of $\log_{10}(x_0)$, compared to the 2D analytical result plotted in Fig. 2.3.

Several points concerning the comparison between the numerical curves and the analytical prediction are interesting to discuss. Firstly, numerically measured attenuation coefficients for all the four grain sizes deviate slightly from the analytical prediction at the beginning of each curve, *i.e.* at the beginning of the confident range of frequencies that we have defined. Future analyzes are necessary to understand this slight deviation. Secondly, a plateau instead of a first power dependence on the normalized frequency for high frequencies $0.3 < \log_{10}(x_0) < 0.74$ is obtained by numerical measurement. We note that for this frequency range, only samples with the grain size of 320μm contribute to the numerical curve and they have much less grains than the samples with the grain sizes of 80μm and 160μm. As there are supposed to be more significant dispersions of ultrasonic attenuation between samples with a smaller quantity of grains, more samples with the grain size of 320μm or a proportional increase in the size of samples according to the increase in the grain size may be necessary to consider. Furthermore, the longitudinal-to-longitudinal scattering part of ultrasonic attenuation is less well simulated than the longtidinal-to-shear scattering part, since wavelength of the longitudinal wave is larger than that of the shear wave for a given frequency. The plateau numerically obtained for high frequencies $0.3 < \log_{10}(x_0) < 0.74$ seems to be coherent with that of the longitudinal-to-shear scattering part as analytically predicted in Fig. 2.3.. Future work is required to fully understand the plateau for high frequencies $0.3 < \log_{10}(x_0) < 0.74$.

4.1.1.2 Crystallographic orientation distribution effect

Dispersions of numerical measurement of ultrasonic attenuation between different samples with the same set of crystal orientations, but with different spatial distribution of these grain orientations are studied. Only three grain sizes of 80μm, 160μm and 320μm are analyzed. To study the dispersions, the averaged numerical results, and the minimum and maximum limits among all the samples are plotted (Fig. 4.3.).

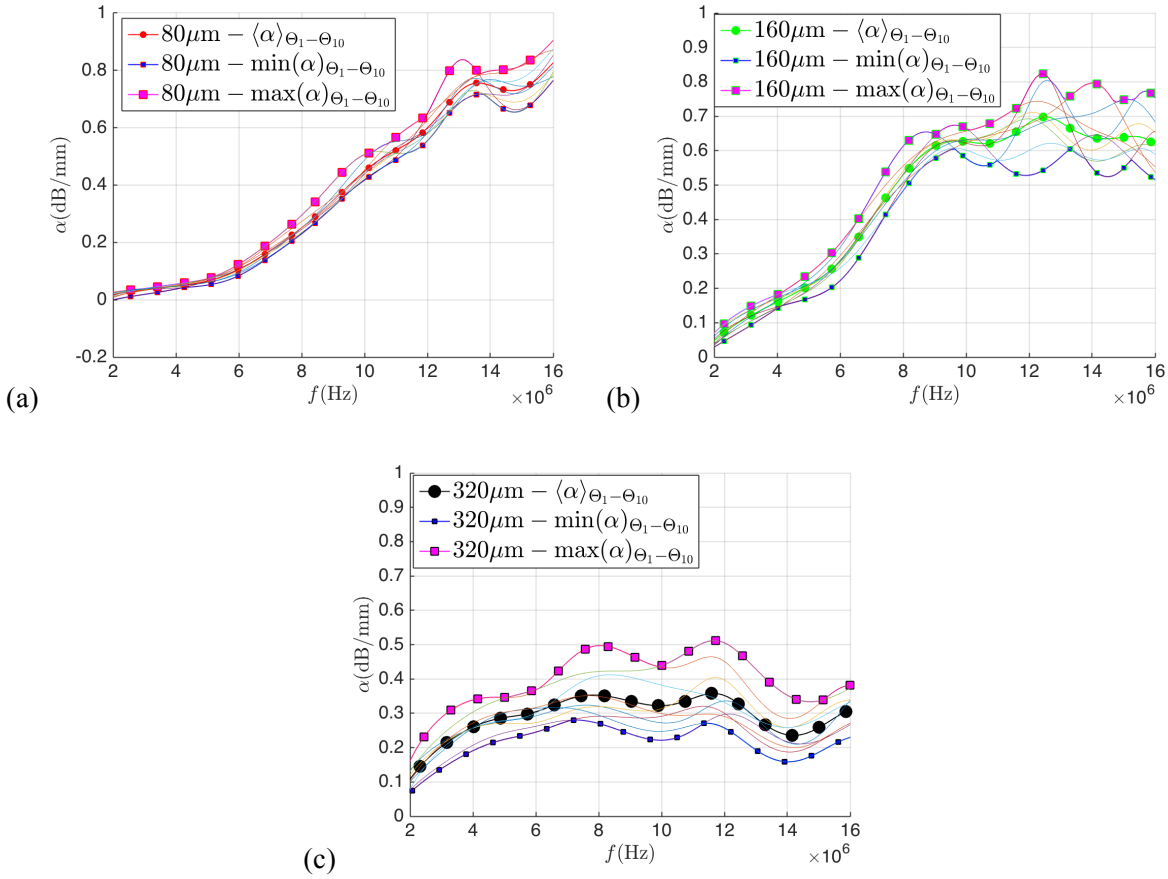

Fig. 4.3. Discrepancies of the numerical measure of attenuation coefficient from the averaged magnitude between different samples with grain sizes of (a) 80μm, (b) 160μm and (c) 320μm. $\langle\alpha\rangle_{\Theta1-\Theta10}$, min$(\alpha)_{\Theta1-\Theta10}$ and max$(\alpha)_{\Theta1-\Theta10}$ denote respectively the averaged numerical result, the minimum and maximum bounds of ten samples.

Two interesting phenomena are noticed: Firstly, it is noted that the dispersion level between samples for a given grain size increases as the increase of frequency. Secondly, the dispersion level between samples seems to depend on grain size for a given frequency: The larger the grain size, the larger the dispersions between samples. A preliminary qualitive analysis is given here. Basically, the effectiveness of scattering at each grain boundary is controlled by the misorientation between two adjacent crystallites. The attenuation level is assumed as the averaged amplitude decay of the incident wave at all the grain boundaries through which ultrasonic waves propagate. For a sample with a given

finite volume, the larger the grain size, the smaller the number of grain boundaries. Accordingly, the dispersion level of attenuation between samples decreases with the number of grain boundaries. We recall that there are respectively 35630, 8855 and 2125 grains considered in the studied domain with the three grain sizes of 80μm, 160μm and 320μm, and at least about 4900, 1200 and 300 grains are respectively involved with the assumption of a plane ultrasound beam.

4.1.2 Numerical evaluation of grain size effects on ultrasonic backscattering

Numerical evaluation of grain size effects on ultrasonic backscattered noise levels is firstly presented. As with the attenuation analysis, four grain sizes of 20μm, 80μm, 160μm and 320μm are studied. Comparison between the numerical estimations and the 2D theoretical prediction (Section 2.2.4.3) is conducted. Then, analysis of influence of crystallographic orientation distribution and grain shape on the evaluation of ultrasonic backscattering is conducted. Effects of the use of the Born approximation on the theoretical prediction of the backscattering coefficient are finally quantified.

4.1.2.1 Grain size effect

Backscattered noises recorded during the time interval [0, T_f] as indicated in Fig. 3.10. are analyzed. Numerical measures of the backscattering coefficient are firstly considered in the frequency domain using the numerical approach defined in Section 2.2.4.2. Then, backscattered noise levels are also estimated and analyzed in time domain.

Numerical estimates of the averaged backscattering coefficient of different samples for four grain sizes are shown in Fig. 4.4.. The backscattering coefficient increases with frequency whatever the grain size. In low frequency region, the larger the grain size, the more important the backscattered noise level. While in high frequency region, the backscattered noise levels are seen to decrease with grain size except for the smallest grain size. Moreover in high frequency region, the backscattering coefficient in

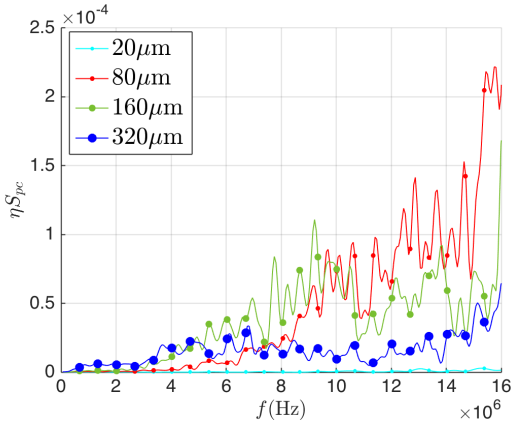

Fig. 4.4. Averaged backscattering coefficient of ten samples numerically estimated as a function of frequency for polycrystalline titanium with four grain sizes of 20μm, 80μm, 160μm and 320μm.

the sample with the largest grains, *i.e.* 320μm becomes nearly constant while the backscattering coefficients of the samples with grain sizes of 80μm and 160μm keep increasing with frequency. The sample with the smallest grain size of 20μm shows a very low level of backscattering coefficient with respect to the other three grain sizes.

Otherwise, Fig. 4.5. compares the master curves obtained theoretically and numerically, *i.e.* the previously compared curves are plotted again in terms of the backscattering coefficient per crystallite $(\eta d)S_{pc}$ and the normalized frequency x_0. The two master curves numerically calculated for the grain sizes of 20μm, 80μm and 160μm are well superimposed in the low frequency range ($x_0 < 0.4$) and are consistent with the lower bound of theoretical prediction $(\eta d)S_{pcMin}$. Then they rapidly increase with a slight fluctuation, keep being more or less superimposed and are bounded by the lower and upper theoretical bounds. Finally in the high frequency range ($x_0 > 2$) the two numerically calculated master curves for the grain sizes of 160μm and 320μm gradually decrease and tend to a constant level defined by the lower theoretical bound $(\eta d)S_{pcMin}$ rather than the upper bound $(\eta d)S_{pcMax}$. This phenomenon is not yet well understood. However we believe that the relatively high degree of anisotropy of the studied material may be a reason as the use of the Born approximation should be no more relevant (see Section 4.1.2.3).

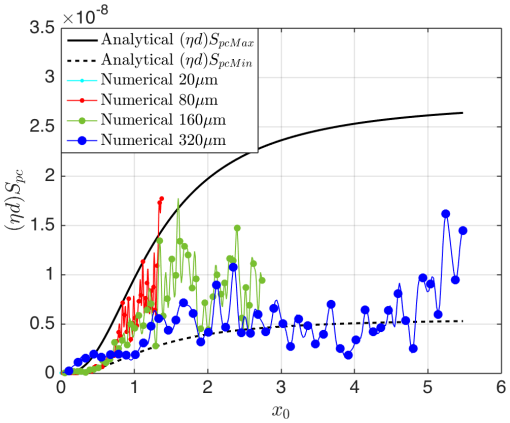

Fig. 4.5. Comparisons in the frequency domain between theoretical and numerical estimates of backscattering coefficient per crystallite as a function of the normalized frequency x_0.

It is of interest to exhibit the variation ranges of the backscattering coefficients between samples. Three curves of maximum values, mean values and minimum values of the backscattering coefficient for ten samples of each grain size are plotted respectively in dash-dotted, solid and dotted lines in Fig. 4.6.. Circle markers are used on the curves of the mean values. The analytical predictions with ηS_{pcMin} and ηS_{pcMax} are plotted in solid and dash lines. For the grain sizes of 80μm, 160μm and 320μm, the averaged response obtained by the numerical simulations fluctuates between the two analytical bounds ηS_{pcMin} and ηS_{pcMax}, its variation tendency with the frequency is consistent with the analytical prediction. Significant gaps between the curves of maximum values and minimum values of the backscattering coefficient for the studied samples are obtained. More particularly, the maximum

values of backscattering coefficient obtained by different samples are larger than the theoretical upper bound ηS_{pcMax} in high frequency range. This point could result from a limited number of grain boundaries with significant dispersions of misorientations in a given sample, which will be further discussed in Section 4.1.2.2. Particularly, for the smallest grain size of 20μm, only two samples are carried out. Small dispersions between these two samples are observed, and the mean backscattering level remains comparable to the analytical lower bound ηS_{pcMin} for most of frequencies, but this is not statistically significant. So emphasis is given to the other three grain sizes in the following discussions.

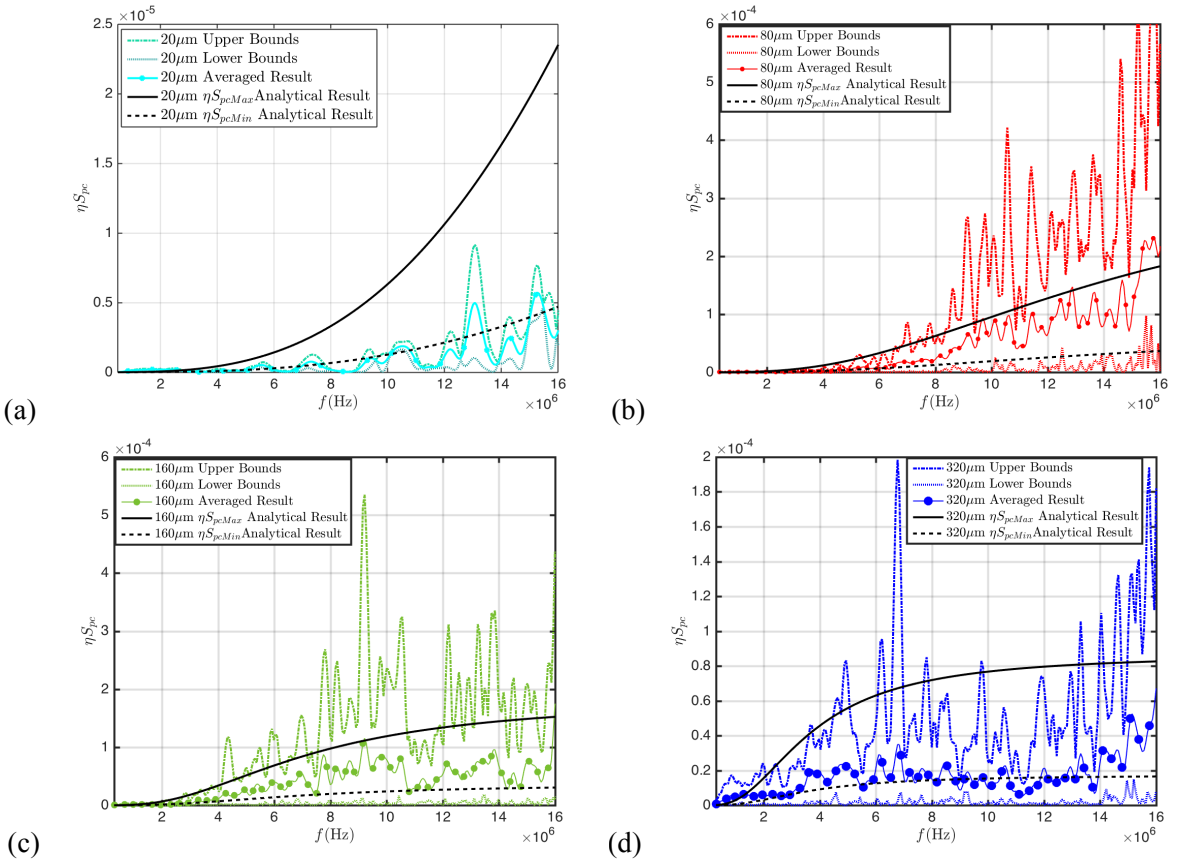

Fig. 4.6. Comparisons in the frequency domain between theoretical and numerical estimates of backscattering coefficients for four grain sizes (a) 20μm, (b) 80μm, (c) 160μm and (d) 320μm.

Numerical measures of grain size effects on the backscattered noise levels in the time domain are conducted using the approach proposed in Section 3.4.3.1. Fig. 4.7. presents, for the three grain sizes of 80μm, 160μm and 320μm, the normalized rms noise level at the two central frequencies 5MHz and 10MHz defined by the two incident Ricker signals. It is observed that for both frequencies the maximum noise level occurs at around $t = 0.8\mu$s, which corresponds to a depth of about 2.3mm below the emitter/receiver line L_e in the studied domain. Considering that the incident signal with normal distributed amplitude is imposed on L_e (Fig. 3.3.), probably it is inferred from this maximum noise level that the amplitude of the plane wave becomes more and more in phase arriving at the depth of about 2.3mm. Afterwards the noise level decreases probably because the attenuation gradually

increases with increasing propagation distance. The highest noise level is given by the grain size of 160μm for $f=5$MHz and by the grain size of 80μm for $f=10$MHz, and on the other hand, the grain size of 320μm gives the lowest noise level for $f=10$MHz. They are qualitatively in good agreement with the previous numerical measurement in the frequency domain (Fig. 4.4.), except for the indistinguishable noise level in the time domain for the grain sizes of 80μm and 320μm at $f=5$MHz. However, by comparison with the theoretical results (Fig. 2.8.), the theoretical curve for the grain size of 160μm is still above the one for the grain size of 80μm at $f=10$MHz, while in Fig. 4.7.(b)) the numerical simulation gives a noise level for the grain size of 160μm lower than the one for the grain size of 80μm. It seems that the transition from the stochastic region to the geometric scattering region numerically occurs earlier than the theoretical prediction.

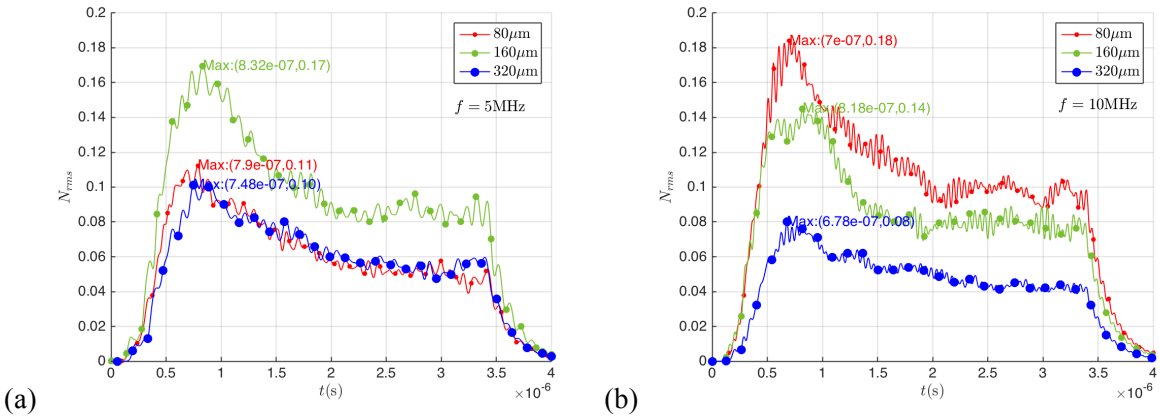

Fig. 4.7. Normalized rms noise level in the time domain for three grain sizes at the central frequencies (a) $f=5$MHz, and (b) $f=10$MHz.

4.1.2.2 Crystallographic orientation distribution effect

Dispersions of backscattering between samples with a same set of crystallographic orientations, but different spatial distributions of these grain orientations are analyzed in this section. Fig. 4.8. presents, in the case of the grain size of 80μm, large variations between the numerically calculated backscattering coefficient for three different samples. In fact the backscattering coefficient in the frequency domain for each sample fluctuates greatly up and down with erratically placed peaks and at some frequencies the backscattering coefficient can be very low and approach zero (Fig. 4.8.(a)). Numerical evaluations of the backscattering coefficient for one sample, then by averaging over five and ten samples are compared in Fig. 4.8.(b). Increasing the number of samples can obviously smooth out fluctuations and improve the comparison between theoretical and numerical evaluations.

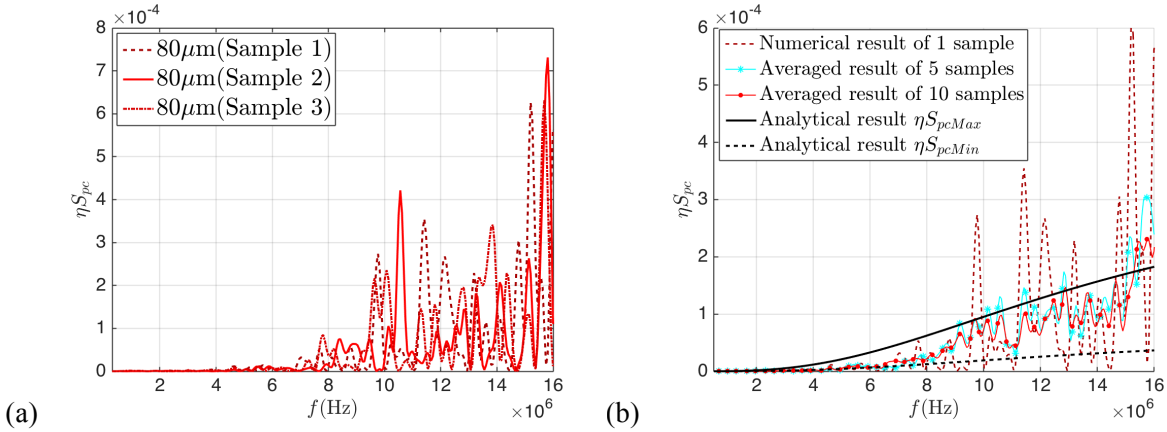

Fig. 4.8. Backscattering coefficient in the frequency domain for the grain size of $80\mu\text{m}$: (a) Variations between three samples; (b) Influence of the number of samples on the averaged backscattering coefficient.

To provide some insight into the fluctuations of the backscattering coefficient with frequency, we consider in the following a group of seven adjacent grains of $80\mu\text{m}$, denoted Ξ and embedded in the homogeneous reference medium (Fig. 4.9.(a)). The seven grains are numbered as indicated in Fig. 4.9.(a) and the centroid of the first grain coincides with the origin of the whole measurement system (Fig. 2.7.). Each grain has a randomly defined crystallographic orientation θ and the phase velocity deviations $\Delta v_{qL}(\theta) = (v_{qL}(\theta) - v_{0L})/v_{0L}$ from the reference medium along the $\boldsymbol{e}_2$ direction for the longitudinal wave are respectively equal to -0.06%, +5.3%, -4.1%, -0.8%, +0.5%, +1.7%, +4.5%. According to the theoretical principle of the isolated scatterer model, eight numerical simulations are performed: One simulation with all seven grains involved and seven contrast simulations each of which has only one grain involved without changing its location.

To illustrate the numerical results, Fig. 4.9. presents the time domain response recorded at the 10th receiver and the backscattering coefficient in the frequency domain for three grains: 2$^{\text{th}}$, 3$^{\text{th}}$ and 6$^{\text{th}}$ (η instead of ηS_{pc} is plotted versus f since S_{pc} is the area of one grain in the case of the isolated scatterer). In the time domain, two primary noise signals scattered by a single grain are observed, which correspond respectively to the longitudinal-to-longitudinal wave scattering and longitudinal-to-shear wave scattering. It seems that a larger velocity deviation $\left|\Delta v_{qL}(\theta)\right|$ results in higher levels of backscattered noise signals in both time and frequency domains. Moreover with equal level of velocity deviation, a grain slower than the reference background gives rise to a higher level of noises backwards than a grain faster than the reference background. In the frequency domain, the backscattering coefficient remains oscillating but with very small amplitudes and increases with frequency on the whole. There is no more backscattering level falling down to zero.

It is shown that the analytical prediction is quantitatively comparable to the backscattering level of an isolated grain with about 1.7% velocity variation from the isotropic reference medium, and significantly smaller than the one with a large magnitude of phase velocity variation $\left|\Delta v_{qL}(g^I)\right|$ (Fig.

4.9.(b)). In fact, the use of the single-scattering approximation and the Born approximation confines the validity of the analytical prediction to slight variation of elastic properties from the equivalent homogeneous medium.

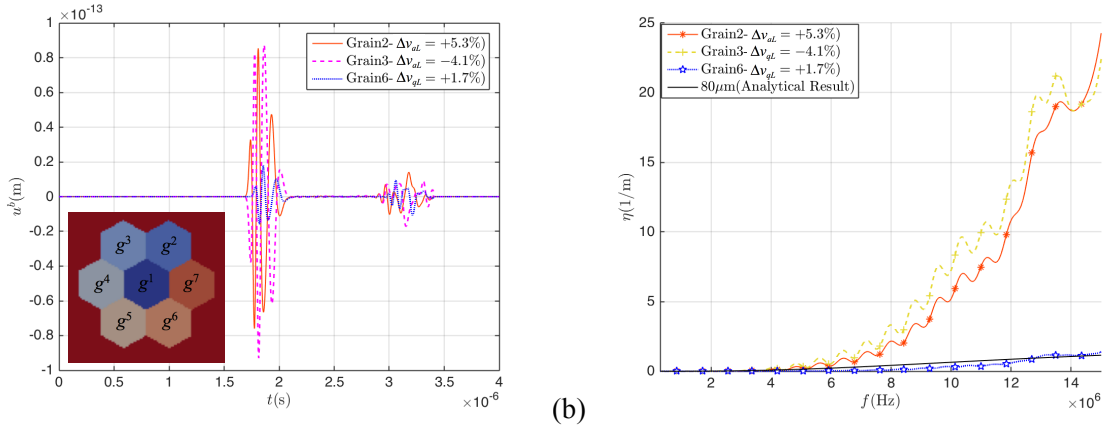

(a) (b)

Fig. 4.9. (a) Time-series scattered noise signals at the 10th receiver and (b) frequency dependence of the backscattering coefficient for three isolated grains within a homogeneous isotropic medium, with the phase velocity deviations Δv_{qL} from the reference medium along the $\boldsymbol{e}_2$ direction for the longitudinal wave being respectively equal to +5.3%, -4.1%, and +1.7%.

Based on the independent scattering approximation using the isolated scatterer model, individual contributions of each grain to the backscattered noise signals are added incoherently $\sum_{l=1}^{l=7} u_2^b(\boldsymbol{x}_{10}, t, g^l)$. Fig. 4.10.(a) compares this sum to $u_2^b(\boldsymbol{x}_{10}, t, \Xi)$, which is the backscattered displacement fields in the $\boldsymbol{e}_2$ direction recorded at the 10th receiver $\boldsymbol{x}_{10}$ for the medium Ξ with all seven grains involved. Insignificant differences between them are observed, which are in fact the part due to the multiple scattering.

Otherwise in the frequency domain, two alternative approaches are proposed to numerically evaluate the backscattering coefficient of the medium Ξ. The first one is directly calculated using the numerical simulation involving all the seven grains as $\eta(\omega, \Xi) = (\beta/V_\Xi)\delta S(\omega, \Xi)\delta S^*(\omega, \Xi)$ (referring to (2.93) with "$\Theta = \Xi$" specifically denoting the crystallographic orientation distribution of the medium). Ξ). The second one is estimated by averaging over the independent contributions of each grain $(\beta/V_g)\langle \delta S(\omega, g^l)\delta S^*(\omega, g^l)\rangle$ (referring to (2.93) and (2.95) with "$\Theta = g^l$" particularly representing the crystallographic orientation of the l^{th} grain g^l belonging to Ξ), which is exactly the application of the independent scattering approximation. Significant differences are then observed between the measured backscattering by these two methods and also with the analytical prediction (Fig. 4.10.(b)).

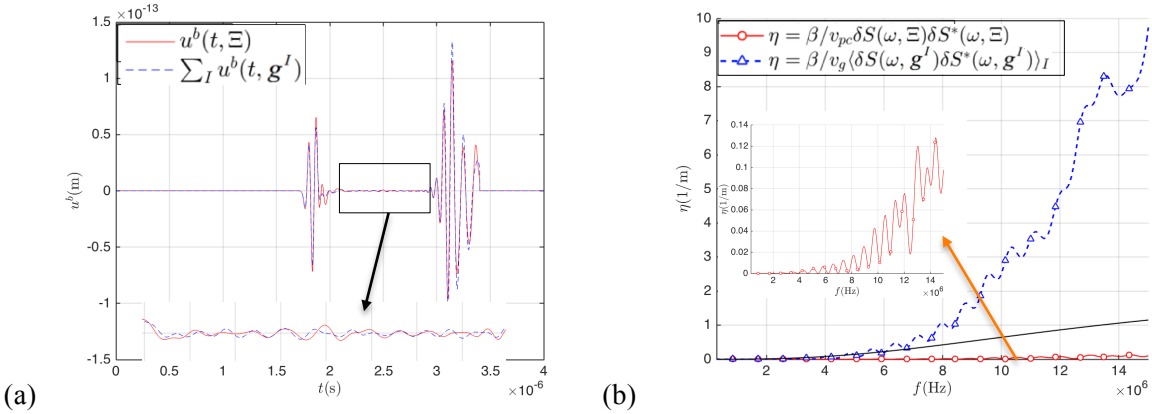

Fig. 4.10. Analysis of the independent scattering approximation. (a) Comparison of time domain signals between the medium Ξ with all seven grains involved, $u_2^b(\boldsymbol{x}_{10},t,\Xi)$, and the incoherent addition of the medium with isolated grains, $\sum_{I=1}^{I=7}u_2^b(\boldsymbol{x}_{10},t,g^I)$ for the backscattered displacement field in the $\boldsymbol{e}_2$ direction recorded at the 10th receiver $\boldsymbol{x}_{10}$ and at the moment t; (b) Comparison of backscattering coefficients calculated using the reciprocity theorem by $\eta(\omega,\Xi)=(\beta(\omega)/V_\Xi)\delta S(\omega,\Xi)\delta S^*(\omega,\Xi)$, and calculated using the single scattering approximation by $\langle\delta S(\omega,g^I)\delta S^*(\omega,g^I)\rangle/V_g$.

To explain those differences, the following estimation of $\delta S(\omega,\Xi)\delta S^*(\omega,\Xi)$ in the frequency domain is written based on the assumption that the scattered noise signal $\boldsymbol{u}^b(\boldsymbol{x}_j,t,\Xi)$ recorded at j^{th} receiver is the sum of the contribution of each individual grain $\boldsymbol{u}^b(\boldsymbol{x}_j,t,g^I)$:

$$\begin{aligned}\delta S(\omega,\Xi)\delta S^*(\omega,\Xi)&=\Big(\sum\nolimits_i\boldsymbol{T}(\boldsymbol{x}_i,\omega)\cdot\sum\nolimits_I\boldsymbol{u}^b(\boldsymbol{x}_i,\omega,g^I)\Big)\Big(\sum\nolimits_j\boldsymbol{T}(\boldsymbol{x}_j,\omega)\cdot\sum\nolimits_J\boldsymbol{u}^b(\boldsymbol{x}_j,\omega,g^J)\Big)^*(\Delta x)^2\\&=\sum\nolimits_{I=J}\Big(\sum\nolimits_i\boldsymbol{T}(\boldsymbol{x}_i,\omega)\cdot\boldsymbol{u}^b(\boldsymbol{x}_i,\omega,g^I)\Big)\Big(\sum\nolimits_j\boldsymbol{T}(\boldsymbol{x}_j,\omega)\cdot\boldsymbol{u}^b(\boldsymbol{x}_j,\omega,g^J)\Big)^*(\Delta x)^2\\&+\sum\nolimits_{I\neq J}\Big(\sum\nolimits_i\boldsymbol{T}(\boldsymbol{x}_i,\omega)\cdot\boldsymbol{u}^b(\boldsymbol{x}_i,\omega,g^I)\Big)\Big(\sum\nolimits_j\boldsymbol{T}(\boldsymbol{x}_j,\omega)\cdot\boldsymbol{u}^b(\boldsymbol{x}_j,\omega,g^J)\Big)^*(\Delta x)^2\\&=\frac{V_\Xi}{V_g}\langle\delta S(\omega,g^I)\delta S^*(\omega,g^I)\rangle+\sum\nolimits_{I\neq J}\delta S(\omega,g^I)\delta S^*(\omega,g^J)\end{aligned}\tag{4.1}$$

where Δx is the distance between two adjacent receivers. We note that (4.1) is true because the stress vector $\boldsymbol{T}(\boldsymbol{x}_i,\omega)=\boldsymbol{T}^0(\boldsymbol{x}_i,\omega)$ is prescribed on the emitter line and is therefore identical in all the simulations (see (2.94)). Two terms are therefore emphasized in (4.1), an auto-correlation term of each grain and a cross-correlation term between different grains. When the number of grains contributing to noise echo signals tends to infinity, the cross-correlation term tends to zero, according to the assumption that $\langle\delta\boldsymbol{C}^I\otimes\delta\boldsymbol{C}^J\rangle=0$ when $I\neq J$. Thereby the incoherent sum of grain contribution $\langle\delta S(\omega,g^I)\delta S^*(\omega,g^I)\rangle/V_g$ should be a good approximation to $\delta S(\omega,\Xi)\delta S^*(\omega,\Xi)/V_\Xi$, which is far from the case with only seven grains. In the same way, only in the case of a sufficiently large number of grains contributing to the received noise echo signals, the backscattering coefficient estimated by using $\langle\delta S(\omega,g^I)\delta S^*(\omega,g^I)\rangle/V_g$ would be comparable to the analytical prediction. Otherwise the cross-correlation term leads to oscillations due to the alternatively positive and negative phase velocity deviations and results in fluctuations in the backscattering coefficient for a sample, as the volume of

polycrystalline sample travelled by the ultrasonic beam always contains only a limited number of grains.

We believe that the number of grains contributing to the backscattering has a significant influence on the oscillatory levels of the numerically estimated backscattering coefficient. Increasing the number of studied samples should lead to a smoother curve of the backscattering coefficient. Generally Margetan et al. propose to use 100 to 1000 waveforms per analysis, given that the receiver positions are chosen to be as widely spaced as possible to reduce the interactions (Margetan et al. 1994). For the averaged numerical results shown in the paper, with 22 receivers and 10 calculated samples, 220 waveforms have been analyzed.

4.1.2.3 Some discussions on the effect of the use of the Born approximation

By applying the Born approximation in the theoretical analysis, noises scattered by a grain are assumed to propagate to receivers without further perturbations by the microstructure. In the analytical development, this is done by replacing the scattered displacement field by the unperturbed field obtained in the homogeneous reference medium. However, considering the relatively high degree of anisotropy of the material considered in the present work, multiple scattering effects should be important since the noise signals can be scattered again at grain boundaries. One of the effects due to the multiple scattering is that noises signals can be attenuated by their interaction with the microstructure especially in high frequency regions. A more sophisticated modeling, such as the second order Keller approximation within the perturbation theory (Stanke et al. 1984), allows to take into account more appropriately the multiple scattering, however it makes the evaluation of backscattering coefficient more complex. In the following a numerical investigation is proposed to partially correct the incoherence in the backscattering coefficient in high frequency regions observed in Fig. 4.6. between the numerical and analytical evaluations.

Indeed the attenuation due to the multiple scattering is automatically included in our numerical evaluation since the scattered field is entirely solved, which is not the case for the analytical evaluation. Therefore, it would be interesting to quantify the omission of the attenuation effects due to the use of the Born approximation and use it to modify numerical data for a more appropriate comparison between the theoretical prediction and the numerical simulation. This would improve the understanding of the ultrasonic propagation characteristics in polycrystalline materials with high degree of elastic heterogeneity.

To take into account the attenuation effect due to the polycrystalline microstructure in the theoretical analysis presented in Section 2.2.4, it is assumed that the frequency dependent attenuation coefficient $\alpha(\omega)$ is known, and then the unknown scattered displacement field is replaced by the following attenuated incident wave mode:

$$\boldsymbol{u}^{1\to 2}(\boldsymbol{x}) \approx U_L^0 \boldsymbol{e}_{inc} \exp(ik_{0L}\boldsymbol{e}_{inc}\cdot\boldsymbol{x})\exp(-\alpha(\omega)\boldsymbol{e}_{inc}\cdot\boldsymbol{x}) \tag{4.2}$$

The only difference with (2.88) is the term $\exp(-\alpha(\omega)\boldsymbol{e}_{inc}\cdot\boldsymbol{x})$.

Then it is straightforward that (2.90) should be accordingly modified as follows:

$$\begin{aligned}&\eta_{att}(\omega,\boldsymbol{e}_{scat})\left(\frac{\beta}{V_{pc}}\left(\frac{\omega}{4P_0(\omega)}\right)^2(U_L^0)^4(k_{0L})^2\left(\alpha^2+(k_{0L})^2\right)\right)^{-1}\\&=\left(\int_\Omega d\boldsymbol{x}\int_\Omega d\boldsymbol{x}'W(r)\exp\left(-2ik_{0L}\boldsymbol{e}_{scat}\cdot(\boldsymbol{x}-\boldsymbol{x}')\right)\exp(-\alpha(\omega)\boldsymbol{e}_{scat}\cdot(\boldsymbol{x}+\boldsymbol{x}'))\right)\boldsymbol{E}_{scat}:\langle\delta\boldsymbol{C}^g\otimes\delta\boldsymbol{C}^g\rangle:\boldsymbol{E}_{scat}\end{aligned}\tag{4.3}$$

where η_{att} denotes the theoretical backscattering coefficient with introduction of the attenuation effect.

As it is found that we have $k_{0L}\geq 200\alpha$ for the material and in the frequency region of interest considered in the present work, consequently the term $\alpha^2+(k_{0L})^2$ is approximated by $(k_{0L})^2$, finally (2.101) becomes:

$$\eta_{att}(\omega)=\eta(\omega)\left(\frac{1}{V_{pc}}\int_\Omega d\boldsymbol{s}\,\exp(-2\alpha(\omega)\boldsymbol{e}_{scat}\cdot\boldsymbol{s})\right)\tag{4.4}$$

We obtain therefore a frequency dependent correction multiplier related to the attenuation effect due to the multiple scattering:

$$corr(\omega)=\frac{1}{V_{pc}}\int_\Omega d\boldsymbol{s}\,\exp(-2\alpha(\omega)\,\boldsymbol{e}_{scat}\cdot\boldsymbol{s})=\frac{1-\exp(-\alpha(\omega)D)}{\alpha(\omega)D}\tag{4.5}$$

with D the propagation distance.

By numerically estimating $\alpha(\omega)$ in the frequency domain, $corr(\omega)$ can be calculated. Fig. 4.11. shows the attenuation correction factor $corr(\omega)$ as a function of frequency for the three grain sizes. It is noted that for a given medium, $corr(\omega)$ decreases as frequency increases then fluctuates around a steady level in the high frequency region. The fluctuations of $corr(\omega)$ are due to the fluctuations of the numerically calculated attenuation coefficient $\alpha(\omega)$ in the high frequency region. So the effect of attenuation is more important in higher frequency ranges. At low frequencies, this factor decreases with the increase of grain size. By contrast, the sample with the smallest grain size shows the largest attenuation correction factor in the high frequency region.

To evaluate the influence of the attenuation neglected by the Born approximation, the numerical result is modified in the following way and then compared to the theoretical prediction:

$$\eta_{Born}(\omega)=\frac{\eta(\omega)}{corr(\omega)}\tag{4.6}$$

Fig. 4.12. compares the theoretical prediction of the backscattering coefficient to the numerical measurements with or without the Born approximation for the three grain sizes. No significant differences are observed in the low frequency region. However as expected the backscattering coefficient corrected by considering the attenuation is significantly higher than the one obtained without the Born approximation in the high frequency region of $f>10\text{MHz}$ especially for the grain

sizes of 80μm and 160μm. These first results seems to confirm the fact that the Born approximation is acceptable in the Rayleigh scattering region, but in a higher frequency region, the Born approximation does overestimate the backscattering effectiveness of the medium as the wave is more and more significantly attenuated due to multiple scattering

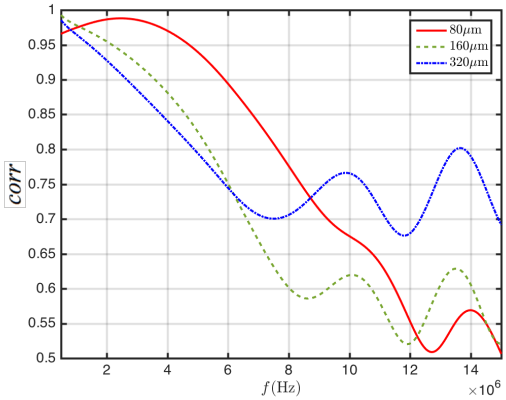

Fig. 4.11. Attenuation correction factor $corr(\omega)$ for three grain sizes

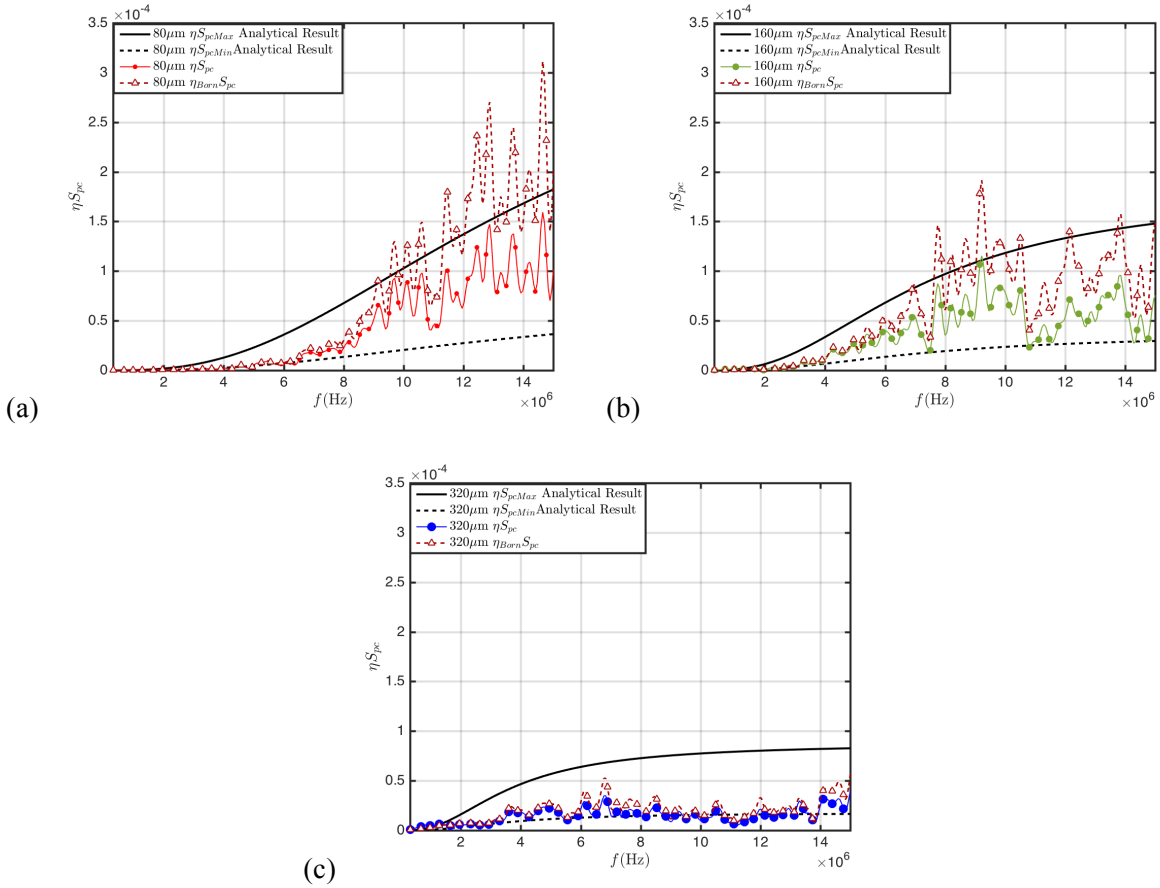

Fig. 4.12. Analysis of the effect of the Born approximation on the numerically measured backscattering coefficient for the grain sizes of (a) 80μm, (b) 160μm and (c) 320μm.

4.1.3 Grain shape effect

To check possible numerical artifacts due to the shape of regular hexagonal grains, FE simulations are performed for the microstructures with irregular hexagonal grains (Section 3.1). Comparisons of the both coefficients of attenuation and of backscattering between the regular and irregular hexagonal grains are shown respectively in Fig. 4.13. and Fig. 4.14. Almost identical amplitude between two cases is observed in the low frequency region, and only slight deviations are found in the high frequency region of $f > 10\text{MHz}$.

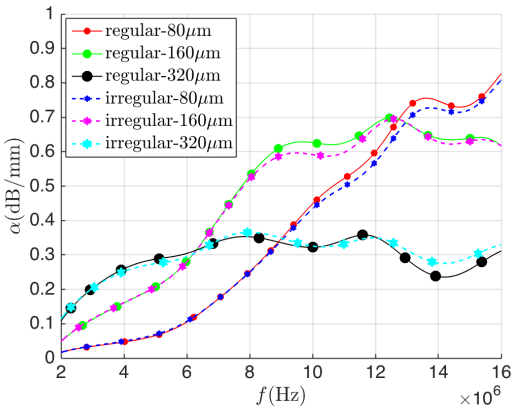

Fig. 4.13. Comparison of the attenuation coefficient between microstructures with regular and irregular hexagonal grains

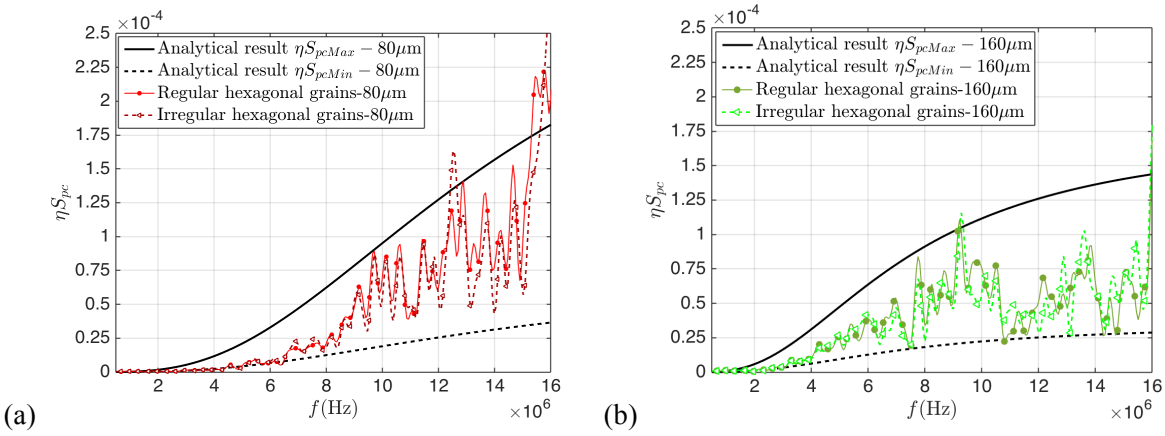

Fig. 4.14. Comparison of the backscattering coefficient between the regular and irregular hexagonal grains of averaged grain sizes (a) 80μm and (b) 160μm.

The very small differences of the attenuation and backscattering coefficient observed between the regular and irregular grains can be explained by considering the spatial correlation function of both types of microstructures. Indeed, differences in the attenuation ((2.37)-(2.39)) and backscattering ((2.89) or (2.90)) coefficients between microstructures containing regular or irregular hexagonal grains with the same randomly-distributed crystallographic orientations are only due to the spatial correlation functions $W(\boldsymbol{r})$, which depends upon the grain size and shape. Under the assumption that the media

are statistically isotropic and ergodic, $W(\boldsymbol{r})$ has a spherical symmetry and depends only on $r=|\boldsymbol{r}|$ the distance between two points. Therefore it is convenient to calculate $W(r)$ in the wave propagation direction, which is the direction $\boldsymbol{e}_2$ in our study. As referred to Stanke (Stanke 1986), an approximation of $W(r)$ can be deduced considering a microstructure composed of a sufficiently large number N of grains in the following way:

$$W_N(r)=\langle\frac{\sum_{I=1}^{N}(c_I-r)^+}{\sum_{I=1}^{N}c_I}\rangle \tag{4.7}$$

Here c_I is the length of a line segment parallel to the propagation direction passing through one grain with its end points falling on the grain boundary, named chord length (Fig. 4.15.), $(\cdot)^+$ is the positive part of $(\cdot)$ and $\langle\cdot\rangle$ represents the spatial average over the whole sample.

For the microstructure with single-size regular hexagonal grains, $W_N(r)$ is independent on N and is therefore simple to calculate. For irregular hexagonal grains, it is possible to obtain the chord lengths in each grain along any line parallel to $\boldsymbol{e}_2$, but the computation amount is huge since a sufficiently large number of grains have to be processed. Thus, an alternative approach is proposed by considering first a regular hexagonal grain having an equivalent area to the irregular hexagonal grain g^I, and then taking the diameter H_I of inscribed circle to this equivalent regular hexagonal grain. Finally, an approximation of $W(r)$ for the medium with irregular hexagonal grains is expressed as:

$$W_N(r)\approx\langle\frac{\sum_{I=1}^{N}(H_I-r)^+}{\sum_{I=1}^{N}H_I}\rangle \tag{4.8}$$

Indeed, under assumption that the media are statistically isotropic and ergodic, (4.8) gives a good estimation of (4.7).

Spatial correlation functions for both microstructures with irregular or regular grains are presented in Fig. 4.16.. It is obvious that the difference in $W(r)$ between both microstructures with regular or irregular grains with the same effective grain size are very small. Hence this study provides an analytical insight into little differences observed in the attenuation and backscattering coefficients between the two microstructures. Two conclusions are drawn here: there is no numerical artifact for calculations with idealized microstructure composed of single-size regular hexagonal grains. Furthermore, slight influence of the geometrical orientation of grain boundaries on the ultrasonic wave scattering is found.

Moreover, they are compared with the spatial correlation function of polycrystals containing random-shaped equiaxed grains with Poisson grain size distribution expressed in an inverse exponential form (2.23). It is noticed that the differences between the regular hexagonal single-size grains and the theoretical model of randomly shaped and equiaxed grains with Poisson distribution are no more than 10%. The maximum difference occurs at the distance equal to the mean grain size 80μm.

It is concluded that the ultrasonic wave scattering level in microstructures containing single-size regular hexagonal grains can give a good representation of the one containing irregular hexagonal grains with a normal size distribution. Further study may be necessary for microstructures containing randomly-shaped grains with a Poisson size distribution, in order to see if it is possible to characterize the grain size distribution by inversion of the ultrasonic attenuation and backscattering.

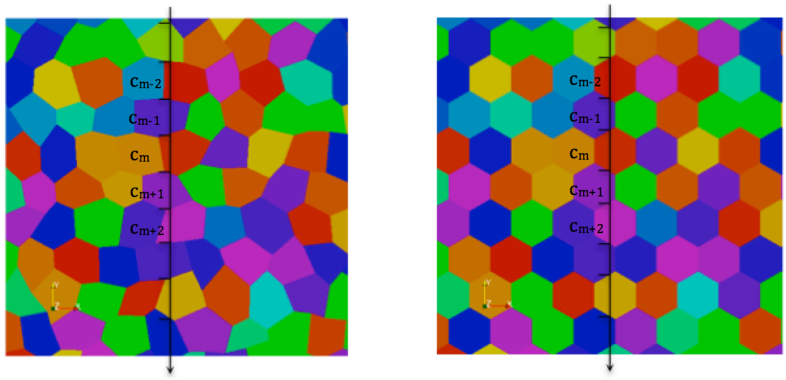

Fig. 4.15. Diagram of spatial correlation function measurement for microstructures with irregular and regular hexagonal grains, c_m denotes the chord length in the grain g^m along the wave propagation direction.

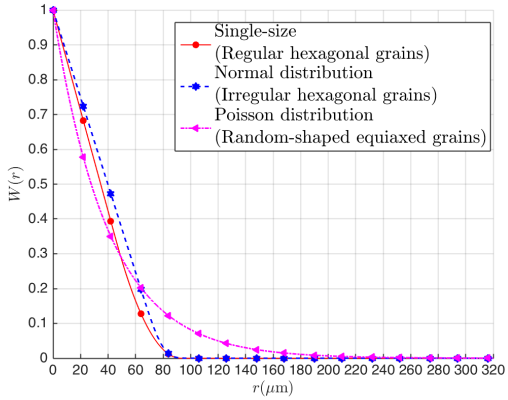

Fig. 4.16. Comparison of the spatial correlation function between microstructures with regular or irregular hexagonal grains.

4.2 Ultrasonic wave scattering in polycrystals with bimodal grain size

Polycrystals with a bimodal grain size distribution are frequently observed during the thermomechanical processing. For example, the heterogeneous grain growth during recrystallization can lead to some exceptionally large grains (e.g. (Garcin et al. 2016)). Another example is a layered microstructure with bands of coarse and fine grains, which frequently occurs in metals processed by rolling or extrusion (e.g. (Zeng et al. 2010)). The equivalent area diameter is usually used to quantify correlation of ultrasonic scattering signals to grain size in the experimental NDE (e.g. (Zeng et al. 2010, Garcin et al. 2016)). Good coherence with the classical unified theory can be found when the spread in

the grain size distribution is small. However, the ultrasonic wave scattering in the bimodal microstructure with high degree of grain size heterogeneity is probably beyond the prediction of the classical theory. To the best of my knowledge, few efforts have been made to analytically investigate the ultrasonic scattering in polycrystals with bimodal grain size distribution. Accordingly, it is of great interest to conduct FE simulations about ultrasonic propagation in microstructures with bimodal grain size. Advantage is highlighted in this case due to the flexibility in modifying the microstructural model and the calculation accuracy.

To gain a preliminary understanding of effects of grain size heterogeneity on the ultrasonic wave scattering, an idealized, single-phase and untextured microstructure with double-size, regular hexagonal grains are considered. It is composed of the smaller grain size of 80μm and the larger grain size of 320μm. 2D FE model and the imposed incident signals are defined as the same as the ones for the unimodal microstructure (Section 3.1). Overall, the following two factors probably affecting ultrasonic wave scattering in such a microstructure are investigated: the volume fraction of the larger grains F_{LG}, the location distribution of the larger grains X_{LG}. We remark that the subscripts "*SG*" and "*LG*" represent respectively the smaller and the larger grains, and for convenience, a bimodal microstructure specifically denotes a single-phase, untextured microstructure with double-size equiaxed grains in the present work.

Firstly, effects of the volume fraction of the larger grain on the ultrasonic wave scattering are investigated, by considering three different values $F_{LG} = 10\%, 45\%, 80\%$. Secondly, different types of location distributions of the larger grains X_{LG} are conducted for $F_{LG} = 45\%$: a random location distribution resulting in $N_{LG} \in [1,\infty]$, an isolated location distribution with $N_{LG} = 1$, forming clusters of the larger grains with random $N_{LG} \in [1,10]$ or with a unique number of $N_{LG} = 10$, and banded microstructures. The variable N_{LG} denotes the number of the larger grains in each cluster. Influence of location distributions of the larger grains on ultrasonic attenuation and backscattering is discussed. Theoretical analysis on effects of the spatial autocorrelation function on ultrasonic attenuation and backscattering in bimodal microstructures is conducted.

4.2.1 Effects of volume fraction of the larger grains

4.2.1.1 Bimodal microstructures with different volume fractions of the larger grains

The bimodal microstructural models in OOFE code are generated in two steps. Firstly, the crystallographic orientations and the coordinates of central points for the smaller grains are input, and the whole microstructure part is filled with the smaller grains. Secondly, information of a given number of crystallographic orientations and of coordinates of randomly selected grain centers are used to create the larger grains. Meanwhile, the smaller grains in the overlapped area with the larger grains are deleted. Bimodal microstructures with three different volume fractions of the larger grains, F_{LG} = 10%, 45%, 80%, are shown in Fig. 4.17., with the larger grains randomly-located in the matrix of the smaller grains.

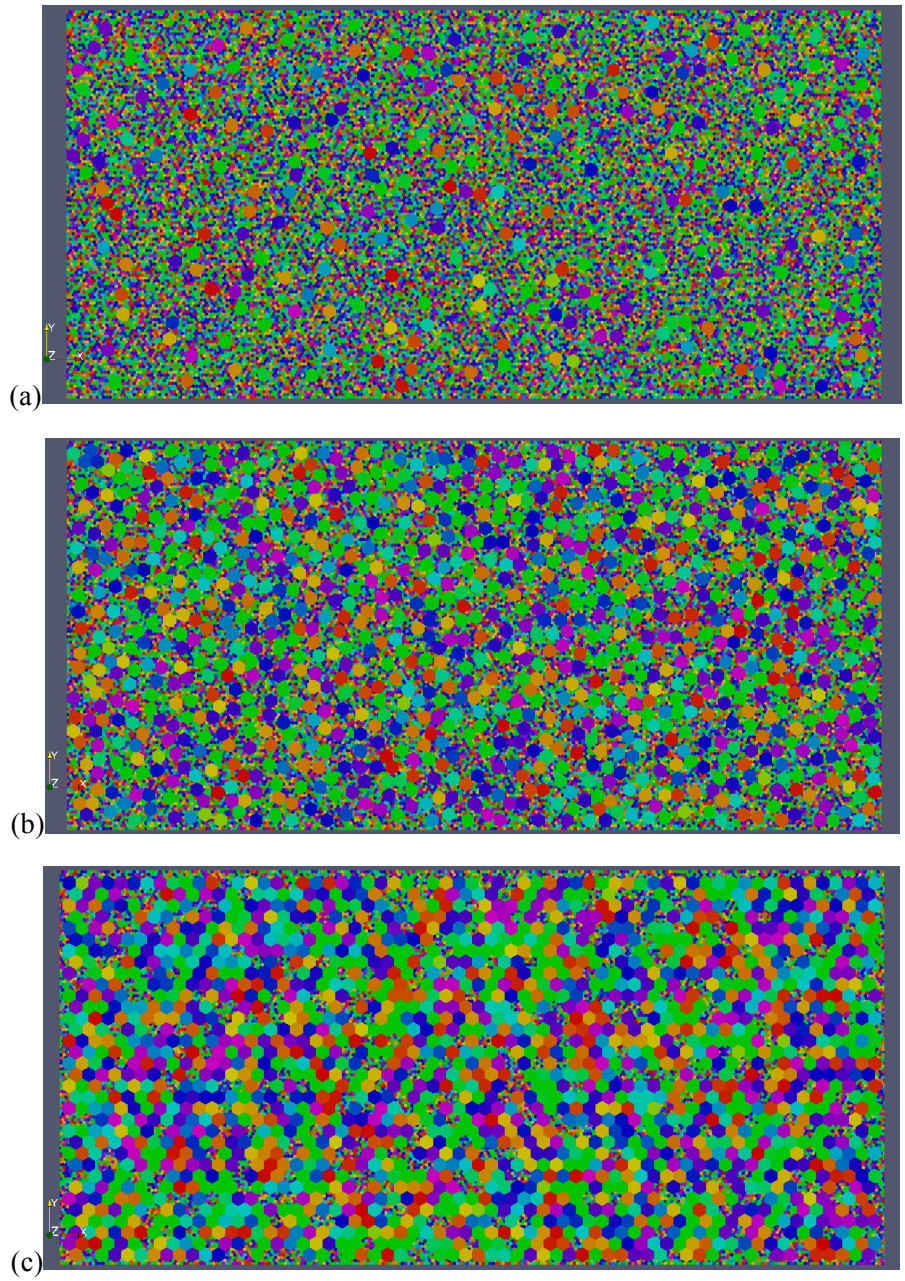

Fig. 4.17. Numerical models of bimodal microstructure composed of grain sizes of 80μm and 320μm, with three volume fractions of the larger grains (a) $F_{LG} = 10\%$, (b) $F_{LG} = 45\%$, (c) $F_{LG} = 80\%$.

A particular point has to be pointed out for the numerical model of bimodal microstructures generated in the present work. Due to the geometrical feature of regular hexagon, the adjacency between the larger and the smaller grains is always accompanied by three semi-hexagons, as shown in Fig. 4.18.. Each of them has half of the area of the smaller grains. The total area of these semi-hexagons is no more than 0.94%, 4.20% and 1.40% of the whole sample area respectively for three distinct volume fractions $F_{LG} = 10\%$, 45%, 80%. Additionally, the attenuation level of each semi-hexagon is about 50% of the attenuation of each small grain since they are both in the Rayleigh region

for most of considered frequencies. Consequently, the influence of these semi-hexagons on the wave scattering can be neglected within the permitted tolerance range.

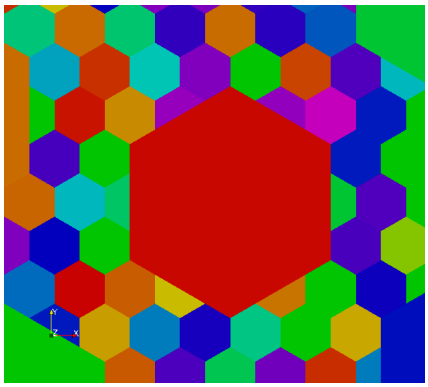

Fig. 4.18. Zoomed view on the adjacency between the larger and the smaller grains in a bimodal microstructure with grain sizes of 80μm and 320μm

4.2.1.2 Effects of volume fraction of the larger grain on ultrasonic attenuation and backscattering

Numerical estimates of the attenuation and backscattering coefficients are respectively presented in Fig. 4.19. and Fig. 4.20. for bimodal microstructures with grain sizes of 80μm and 320μm for three values of F_{LG} = 10%, 45%, 80%. For each case of F_{LG}, the averaged response of ten samples with different spatial distributions of crystallographic orientations for the larger grains is plotted, where spatial distributions of crystallographic orientations for the smaller grains and the grain location distributions remain unchanged. They are compared with the attenuation and backscattering coefficients in the unimodal microstructures with grain sizes of 80μm and 320μm respectively.

It is interesting to notice that both the attenuation and backscattering coefficients of bimodal microstructures are in-between the ones of unimodal microstructures whatever the value of F_{LG}. They pass approximately by the intersection point of curves of the two unimodal media, at the frequency of about 9MHz for the attenuation, and about 8MHz for the backscattering. Specifically, the attenuation and backscattering levels of a bimodal microstructure decreases with the volume fraction of the larger grain size at frequencies lower than the intersection point and this tendency is reversed afterwards. Considering an extremely low fraction of the larger grains, discrepancies of the attenuation and backscattering between the bimodal medium and the unimodal microstructure with the grain size of 80μm are indistinguishable. On the other hand, as the increase of the volume fraction of the larger grains, the attenuation and backscattering of the bimodal microstructure approach gradually to that of the unimodal microstructure with grain size of 320μm.

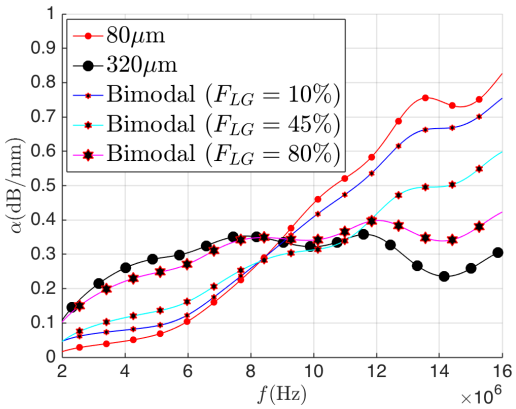

Fig. 4.19. Frequency dependence of attenuation within bimodal microstructures with grain sizes of 80μm and 320μm for three cases of volume fractions of the larger grains F_{LG} = 10%, 45%, 80%.

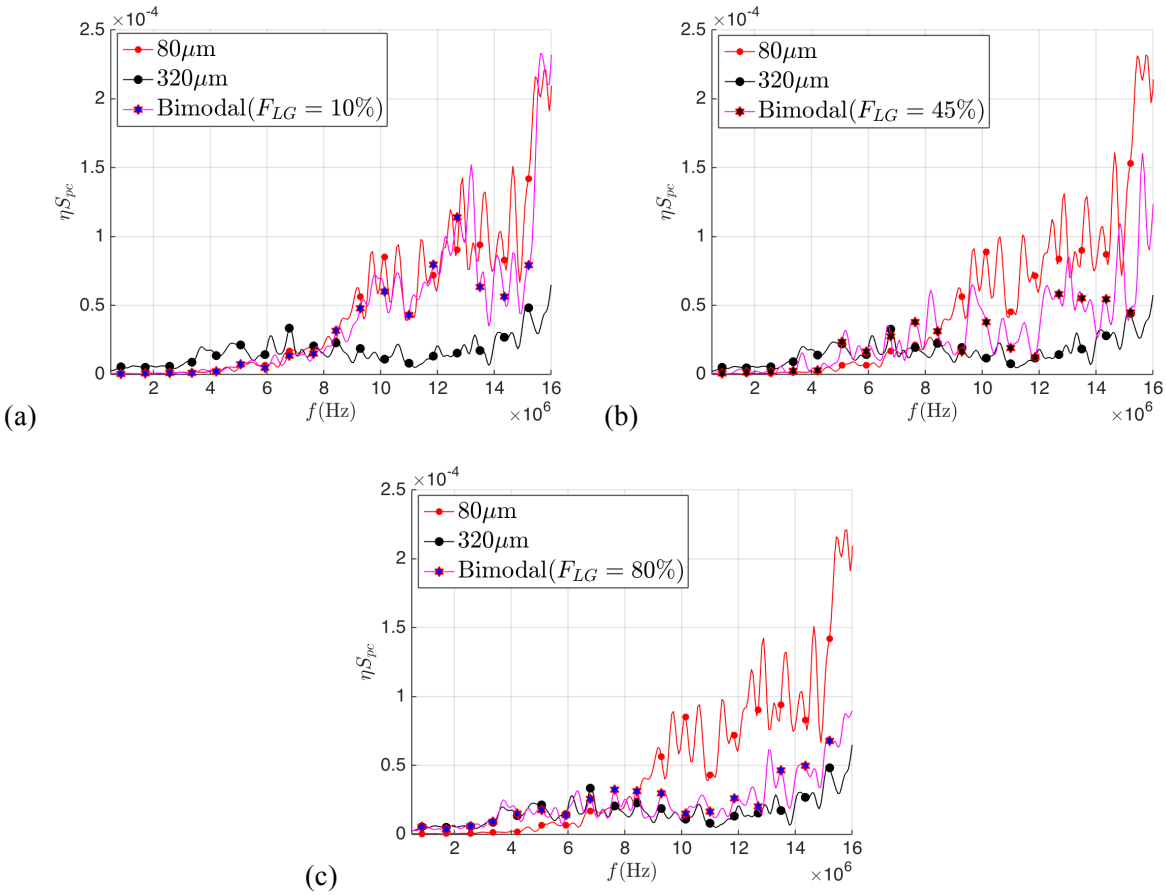

Fig. 4.20. Frequency dependence of the backscattering within the bimodal microstructures with grain sizes of 80μm and 320μm for three cases of volume fractions of the larger grains (a) F_{LG} = 10%, (b) F_{LG} = 45%, (c) F_{LG} = 80%.

4.2.2 Effects of the location distribution of the larger grains

The dimension of the studied polycrystalline sample is restricted by the high computational cost, so there exist for example only 1000 larger grains in the bimodal microstructure with the volume fraction $F_{LG} = 45\%$. The relatively small number of the larger grains in bimodal microstructures considered herein increases greatly the probability of heterogeneous location distribution, making it necessary to consider the influence of the location distribution of the larger grains X_{LG} on ultrasonic wave scattering. In this section, five different types of X_{LG} are considered: a random location distribution with $N_{LG} \in [1,\infty]$, a location distribution with clusters of the larger grains with a random distribution of $N_{LG} \in [1,10]$, a location distribution with clusters containing 10 larger grains $N_{LG} = 10$, an isolated location distribution with $N_{LG} = 1$, and banded microstructures. Several samples with different location distributions of the larger grains for each distribution type are conducted. Dispersions between samples as well as the averaged responses of ultrasonic attenuation and backscattering for different distribution types are discussed in the sole case of $F_{LG} = 45\%$, which corresponds to nearly the maximum volume fraction we can generate with $N_{LG} = 1$ (*i.e.* there is no cluster of the larger grains).

4.2.2.1 Bimodal microstructures with different types of location distributions of the larger grains

Firstly, a random location distribution of the larger grains is regarded as a general case, with individual location of each grain randomly-selected (Fig. 4.21.(a1)). Statistics for six samples with randomly distributed larger grains suggests that about 70% of the larger grains are isolated, and the rest form clusters with $N_{LG} \in [1,4]$ for the volume fraction of $F_{LG} = 45\%$ (Fig. 4.21.(a2)).

Secondly, to model the inhomogeneous grain growth during the recrystallization processing (Garcin et al. 2016), numerical models of bimodal microstructures containing clusters are built. Two particular cases are considered: clusters with a random distribution of $N_{LG} \in [1,10]$ (Fig. 4.21.(b1)) and clusters with a unique number of $N_{LG} = 10$ to display the influence of clusters on the wave scattering to the largest extent (Fig. 4.21.(c)). Frequency distribution of N_{LG} in each cluster for the former case is plotted in Fig. 4.21.(b2), and it is seen that fewer than 5% of large grains are isolated. All the clusters in these two cases are random-shaped and their center points are randomly distributed. The isolated distribution ($N_{LG} = 1$) is considered as a reference case, with all the larger grains isolated in the matrix of the smaller grains (Fig. 4.21.(d)).

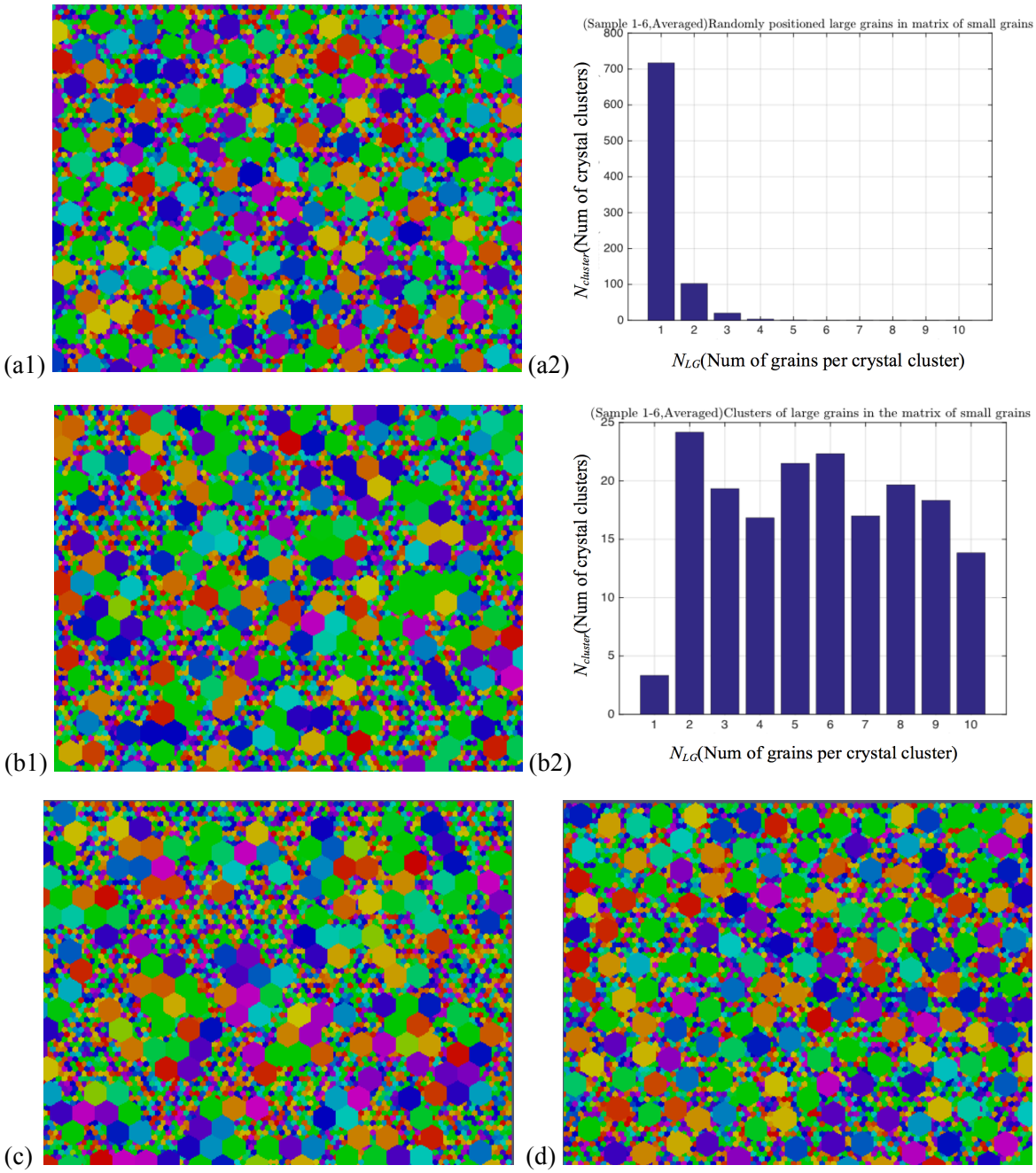

Fig. 4.21. Bimodal microstructures with four different location distributions of the larger grains in the matrix of the smaller grains for $F_{LG} = 45\%$: (a1) a random location distribution and (a2) frequency distribution of N_{LG} for a random location distribution; (b1) forming crystal clusters of the larger grains with $N_{LG} \in [1,10]$ and (b2) frequency distribution of N_{LG} for the case of $N_{LG} \in [1,10]$; (c) forming clusters of the larger grains with a unique number $N_{LG} = 10$; (d) an isolated location distribution with $N_{LG} = 1$; F_{LG} denotes the volume fraction of the larger grain and N_{LG} denotes the number of the larger grains in each cluster.

A layered microstructure with bands of coarse and fine grains through thickness gradients frequently occurs in metals processed by rolling or extrusion, because some grains resist refinement more than others during the thermomechanical processing. These banded microstructures have been observed in the research work on the polycrystalline niobium by Zeng et al. (Zeng et al. 2010) and Hartwig et al. (Hartwig et al. 2007), which can exhibit unacceptably low mechanical strength. However, for the application of NDE, few efforts have been devoted to the study on the effect of banded microstructures on the ultrasonic wave scattering. Zeng et al. applied the single-scattering approximation to a hypothetical banded microstructure, where each layer of a specific thickness has a different grain size and corresponding attenuation. Such an idealized microstructure with bands of the larger and the smaller grain sizes of 80μm and 320μm for the given volume fraction $F_{LG} = 45\%$ is used in our FE simulations. Two-layer, three-layer and four-layer structures are considered (Fig. 4.22.). Unlike the overly simplified analytical model of Zeng et al., the complexes physical mechanism of ultrasonic wave scattering in such idealized microstructure, such as effects of multiple scattering and the long-range correlation between grains, is included in our numerical modeling. The objective is to answer the open question whether such microstructures with bands of different grain sizes can be detected using an ultrasonic wave signals.

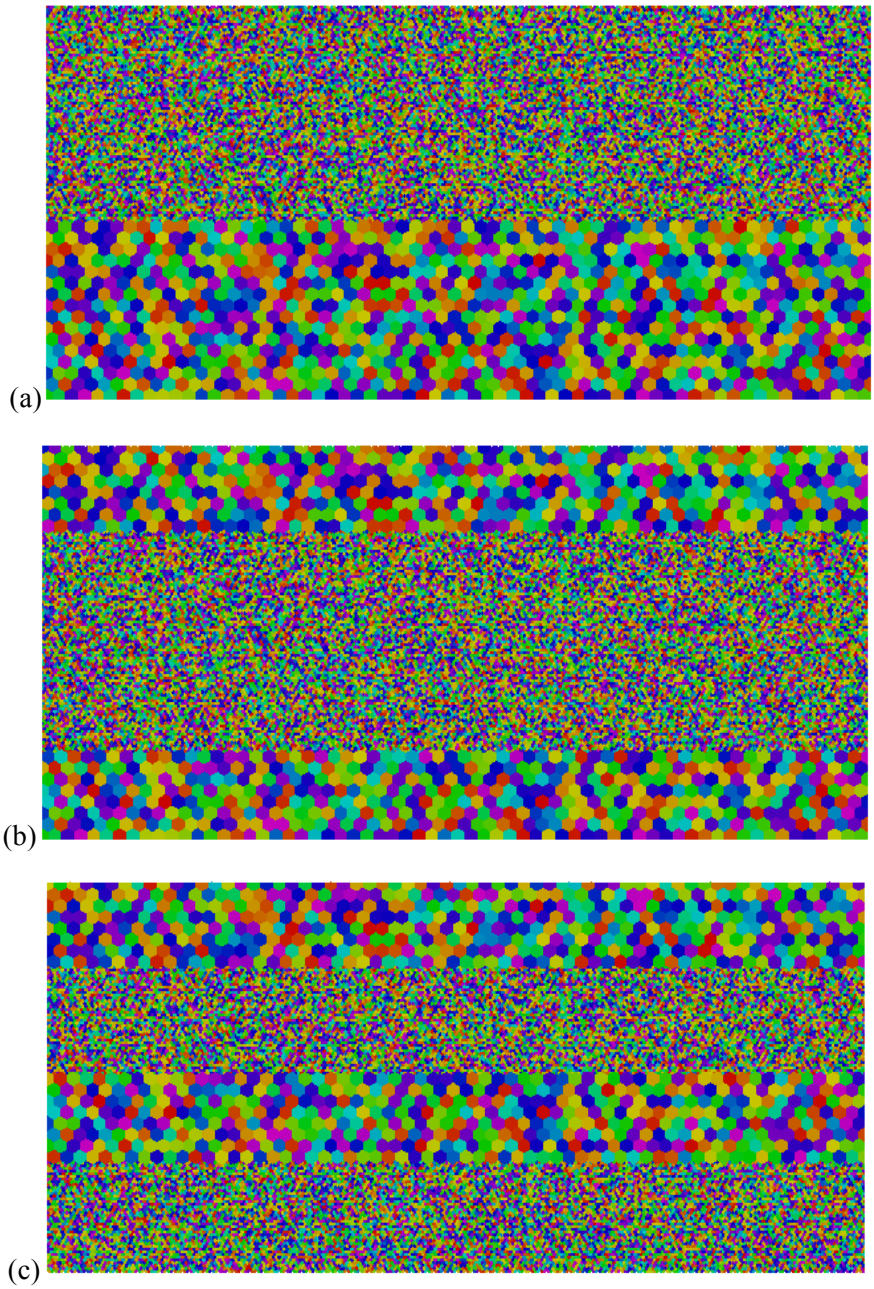

Fig. 4.22. Banded bimodal polycrystals with (a) two-layer, (b) three-layer and (c) four-layer microstructures

4.2.2.2 Effects of location distributions of the larger grains on ultrasonic attenuation and backscattering

Dispersions of ultrasonic attenuation over six samples for each type of location distribution of the larger grains, except for the banded location distributions there are only three samples, are at first presented in this section, followed by the averaged ultrasonic attenuation and backscattering over five types of location distributions of the larger grains.

The limited number of the larger grains in the studied bimodal microstructures makes the grain location distribution for each specific sample nonuniform and anisotropic in each spatial direction, especially for the samples containing clusters with ten large grains in each cluster. Fig. 4.23. shows dispersions of the attenuation coefficient between different samples for each distribution type. It is observed that the deviation from the averaged response of each specific sample can be significant. For example, the fifth sample with randomly distributed large grains exhibits much greater attenuation level than the other samples at low frequencies, approaching to the attenuation level of the unimodal microstructure with the larger grain size. The first sample with $N_{LG} = 10$ shows much more significant attenuation coefficient at high frequencies, similar to the one of the unimodal medium with the smaller grains quantitatively.

This phenomenon can be explained by two principle reasons. Firstly, for each distribution type, the set of crystallographic orientations for each grain remains unchanged. However, as the location distribution of the larger grains is changed, grain boundary misorientations between each larger grain and the smaller grains around are modified, which cause directly dispersions of ultrasonic attenuation between samples. Furthermore, the distribution of the larger grains cannot be homogeneous and ergodic due to the limited area of sample. Therefore, the number of grain boundaries in each sample which an ultrasonic wave propagates through is slightly different. To conclude, influence of location distributions of the larger grain on ultrasonic attenuation can be considerable for a given sample with a limited volume.

As discussed in Section 4.1.2.2, the oscillation level of backscattering coefficient with frequency for a specific sample is significant. Therefore, dispersions of the backscattered noises between different samples are not shown.

Taking into account the large dispersions between samples with different grain location distributions, it is of more interest to compare the averaged response of each type of distribution. Fig. 4.24. shows the attenuation and backscattering coefficients averaged over six samples for each type of the grain location distribution. Insignificant variations of the attenuation between different cases of grain location distributions are noticed. Variations of the backscattering coefficients between different cases are difficult to distinguishable due to the significant oscillation level. Careful comparison shows the similar tendency and comparable amplitude between different cases of grain location distributions. Exceptionally, a peak at about the frequency 12MHz is highlighted for the backscattering of the banded microstructures, which is about once larger than the backscattering level in the unimodal microstructure with the grain size of 80μm . In fact, only three samples of banded microstructures are considered (by contrast six samples are considered for the other four distribution types), for which a limited possibilities of grain boundary misorientations are considered. When the contributing grain boundary misorientations to the backscattering effectiveness around a certain frequency is insufficient,

it is believed that either an exceptional peak or a magnitude approach to zero at a certain frequency is possible to occur.

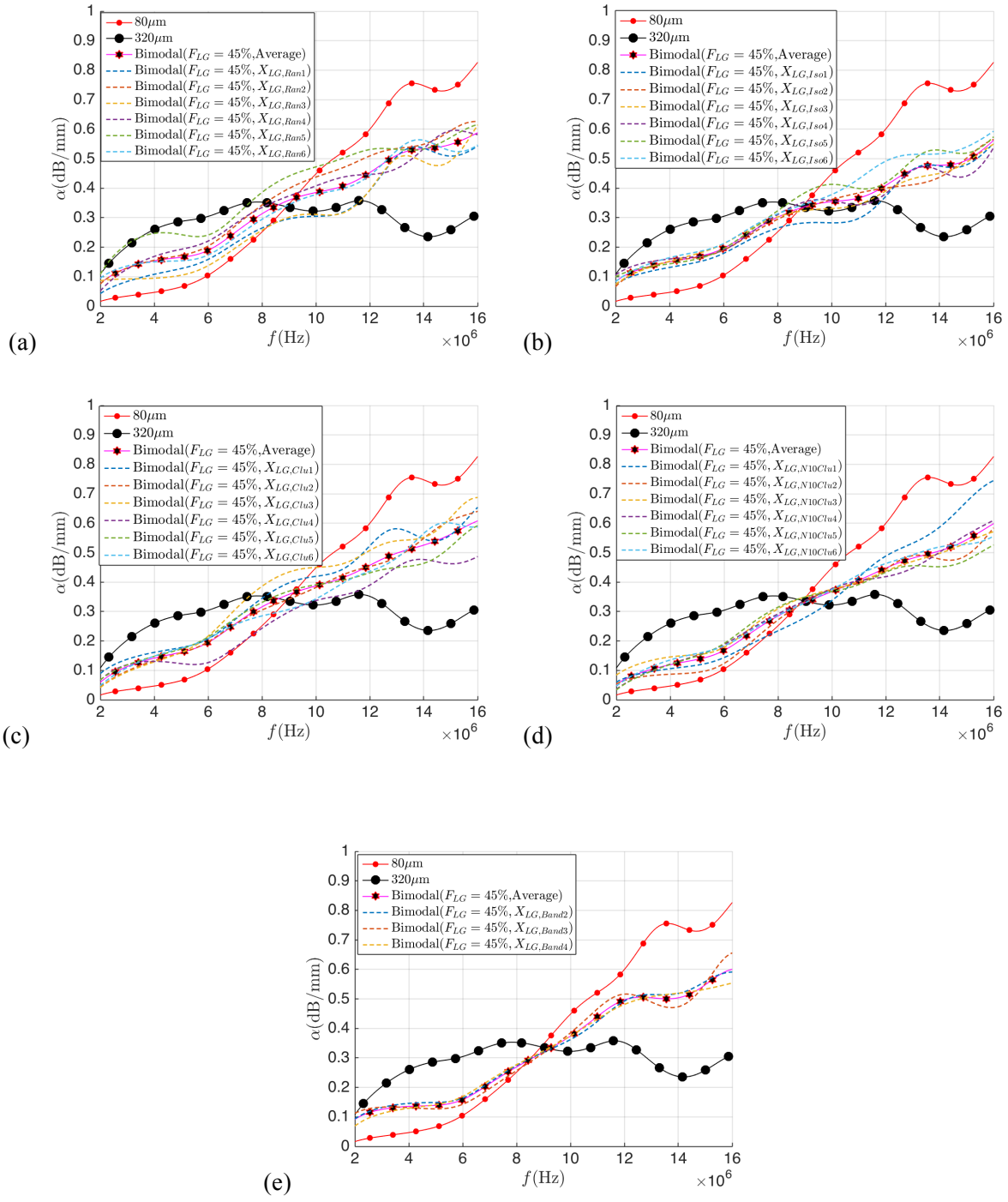

Fig. 4.23. Dispersions of the attenuation coefficient between different samples for five distinct large grain locations distribution: (a) a random distribution ($X_{LG,Ran}$), (b) an isolated distribution with N_{LG} = 1 ($X_{LG,Iso}$), (c) crystal clusters with $N_{LG} \in [1,10]$ ($X_{LG,Clu}$), (d) crystal clusters with $N_{LG} = 10$ ($X_{LG,N10Clu}$), and (e) banded microstructures ($X_{LG,Band2}$, $X_{LG,Band3}$ and $X_{LG,Band4}$ denote respectively two-layer, three-layer and four-layer microstructures). N_{LG} denotes the number of the larger grains in each cluster.

One important conclusion is drawn here: for a spatially uniform and isotropic medium, effects of the grain location distribution on the ultrasonic wave scattering in bimodal microstructures are insignificant. The location distribution of the larger grains in polycrystalline materials including the banded microstructure seems impossible to be characterized by inversion of ultrasonic attenuation and backscattering.

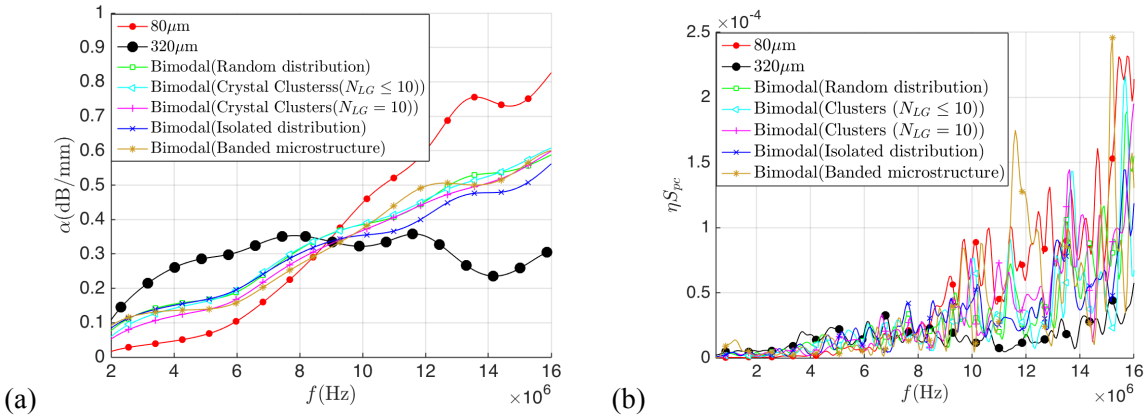

Fig. 4.24. Numerical estimations of the averaged frequency-dependent (a) attenuation and (b) backscattering coefficients in bimodal microstructures with five different types of location distributions of the larger grains: (1) a random location distribution, (2) an isolated distribution with $N_{LG} = 1$, (3) forming clusters with $N_{LG} \in [1,10]$, (4) forming clusters with $N_{LG} = 10$ and (5) a banded microstructure. N_{LG} denotes the number of the larger grains in each cluster.

4.2.3 Spatial autocorrelation function of the bimodal microstructure

In this section, to provide theoretical reflections on numerical measurements about effects of the volume fraction and of location distributions of the larger grains, the spatial autocorrelation functions in bimodal microstructures are analytically investigated.

Two-point autocorrelation function of elastic tensors $\langle \boldsymbol{\delta C}(\boldsymbol{x}) \otimes \boldsymbol{\delta C}(\boldsymbol{x}') \rangle$ influences significantly the ultrasonic wave scattering effectiveness in single-phase, untextured polycrystalline materials (Stanke et al. 1984). Based on the fundamental assumption that the crystallographic orientations in different crystallites vary independently, $\langle \boldsymbol{\delta C}(\boldsymbol{x}) \otimes \boldsymbol{\delta C}(\boldsymbol{x}') \rangle$ can be simplified into the multiplication of spatial autocorrelation function $W(\boldsymbol{r})$ and autocorrelation function of elastic tensors $\langle \boldsymbol{\delta C}^g \otimes \boldsymbol{\delta C}^g \rangle_\Theta$ (defined in (2.13) with the term $\langle \boldsymbol{\delta C}^g \rangle_\Theta = 0$). The second term is determined only by the elastic constants of single crystallite for an untextured medium. Therefore, for a bimodal microstructure where both the larger and the smaller grains are randomly-oriented and possess the same properties, the spatial autocorrelation function $W(\boldsymbol{r})$ plays a dominant role in the ultrasonic scattering. For a statistically isotropic and ergodic medium, we recall that $W(\boldsymbol{r})$ is determined only by the distance r between two points $\boldsymbol{x}$ and $\boldsymbol{x}'$, *i.e.* $W(\boldsymbol{r}) = W(r)$ with $r = |\boldsymbol{x} - \boldsymbol{x}'|$.

To quantify the function $W(r)$ in a spatially isotropic medium, it is useful to start with the function $W^{(I)}(r)$ which defines the possibility that two points separated by the distance r are located in

the grain *I*. $W^{(I)}(r)$ can be obtained by counting the relative number of times that a line segment of length *r* is wholly in the grain *I* when thrown randomly onto an infinite line in the system (Torquato 2013). *A* is denoted as the midpoint of the line segment of length *r*. The possibility that point *A* is in the grain *I* is equal to $f_V^{(I)}$, the volume fraction of the grain *I*. Then given that the point *A* is within the grain *I*, the possibility that point *A* is on a chord with length between *y* and $y+dy$ which meanwhile is entirely in the grain *I* can be written as $((y-r)H_v(y-r)p_c^{(I)}(y)/\overline{l}_c^{(I)})dy$ (Torquato 2013). Here $p_c^{(I)}(y)$ defines the chord-length density probability that a randomly placed point fall on a chord *c* with the length *y* in the grain *I*. $\overline{l}_c^{(I)}$ specifies the mean chord length for the grain *I*. $H_v(x)$ denotes the Heaviside step function defined to be 0 if $x<0$ and otherwise equal to *1*. Accordingly, $W^{(I)}(r)$ can be defined by combining the two possibilities mentioned immediately above and integrating the possibility over all possible chord length *y*, expressed as (Torquato 2013):

$$W^{(I)}(r) = f_V^{(I)} \int_0^\infty \frac{(y-r)H_v(y-r)}{\overline{l}_c^{(I)}} p_c^{(I)}(y)dy \tag{4.9}$$

Given that each grain is convex and has identical chord-length density possibility $p_c(y)$, $W(r)$ in the macroscopically isotropic medium with unimodal grain size distribution can be analytically evaluated by the average of $W^{(I)}(r)$ over all the grains in the ensemble medium, obtained as follows (Stanke 1986):

$$W(r) = \langle W^{(I)}(r) \rangle = \int_r^\infty \frac{(y-r)}{\overline{l}_c} p_c(y)dy \tag{4.10}$$

where $\overline{l}_c$ represents the mean chord length for the ensemble medium. The approximations to the mean chord length in the grain *I* based on *N* chords and in the medium containing *M* grains can be made as:

$$\overline{l}_c^{(I)} = \frac{1}{N}\sum_{n=1}^{N} l_{cn},\ \overline{l}_c = \frac{1}{M}\sum_{I=1}^{M} \overline{l}_c^{(I)} \tag{4.11}$$

For the medium with a Poisson grain size distribution, the mean chord length is equal to half of the mean grain size, *i.e.* $\overline{l}_c = \overline{d}/2$ (Stanke 1986). By contrast, the mean chord length in the medium with regular hexagonal single-size grains is defined as $\sqrt{3}/2$ times of the inscribed circle diameter of the hexagon, *i.e.* $\overline{l}_c = \sqrt{3}H/2$. It is assumed that the chord length is statistically independent of each other and the crystallites are non-overlapped with one another.

Considering a spatially isotropic microstructure with bimodal grain size distribution, the spatial autocorrelation function $W(r)$ is found as:

$$W^{Bi}(r) = F_{SG}\int_r^\infty \frac{(y-r)}{(\overline{l}_c)^{SG}} p_c^{SG}(y)dy + F_{LG}\int_r^\infty \frac{(y-r)}{(\overline{l}_c)^{LG}} p_c^{LG}(y)dy \tag{4.12}$$

where the superscript *Bi* represents the bimodal microstructure. F_{SG}, F_{LG} define the total volume fractions for two different modes of grains, respectively.

The spatial autocorrelation function $W(r)$ in unimodal polycrystalline media with regular hexagonal single-size grains can be empirically evaluated using the chord length measured from the micrograph of the studied medium as defined in (4.7). The analytical results of $W(r)$ for unimodal microstructures with grain sizes of 80μm and 320μm are shown as the red and black dashed lines in Fig. 4.25., respectively. Whereas, $W^{Bi}(r)$ in bimodal polycrystalline media containing regular hexagonal double grain sizes of 80μm and 320μm with $F_{LG}=45\%$ can be analytically measured by (4.12), shown as the magenta dashed line in Fig. 4.25.. It is obviously in-between the spatial autocorrelation functions of the unimodal media, and determined by the volume fractions of the constituent grains. It is a good approximation when the larger grains are statistically homogeneous distributed in the medium. However, for one specific sample containing a limited number of the larger grains, $W^{Bi}(r)$ can be beyond the analytical prediction by (4.12).

$W^{Bi}(r)$ in polycrystals with regular hexagonal double-size grains is further compared with the one in polycrystals consisting of randomly-shaped equiaxial grains with a bimodal Poisson grain size distribution. Negligible discrepancies are observed between bimodal polycrystals with the Poisson grain size distribution and with regular hexagonal double-size grains at small distances $r<200\mu$m. Afterwards, the discrepancy increases with the distance r and reaches up to the maximum magnitude 0.05 at around $r=320\mu$m, where W^{Bi} for the microstructure comprising bimodal grain sizes of 80μm and 320μm is expected to be zero since the two points separated by a distance of more than the larger grain size 320μm is impossible to be located in the same crystal. Therefore, from the aspect of the spatial correlation function, an idealized microstructure composed of double-size regular hexagonal grains is a good approximation of polycrystals composed of randomly shaped equiaxial grains with a bimodal Poisson grain size distribution at small distances $r<200\mu$m.

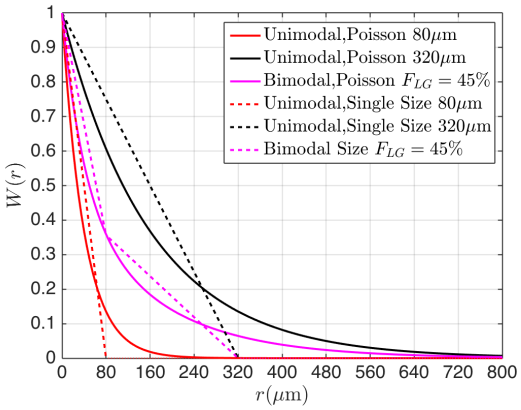

Fig. 4.25. Spatial autocorrelation function in a polycrystalline microstructure with bimodal grain sizes

4.2.4 Ultrasonic attenuation and backscattering driven by the volume fraction

Based on the investigation of spatial autocorrelation function, quantitative relation of the ultrasonic attenuation and backscattering coefficients between unimodal and bimodal polycrystalline

microstructures is first proposed analytically, then the numerical validation for the ultrasonic attenuation and backscattering driven by the volume fraction of the constituent grains is conducted.

4.2.4.1 Analytical prediction

According to theoretical investigations, it is seen from (2.37)-(2.39) that the ultrasonic wave scattering in polycrystalline materials are both affected by the elastic moduli of single crystal and the density of the material, the preferred grain orientation as well as the grain size and shape. Effects of grain size and shape are introduced by the spatial autocorrelation function $W(\boldsymbol{r})$. Considering a single-phase, untextured and macroscopically homogeneous and isotropic polycrystalline microstructure consisting of equiaxial grains, it is assumed that no density variation exists, the effective elastic properties of the ensemble medium is constant and $W(\boldsymbol{r})$ becomes one-dimensional spatial autocorrelation function $W(r)$. Therefore, the attenuation and backscattering coefficients in such a microstructure with bimodal grain sizes are driven only by $W(r)$. Taking into account the linear relationship of the spatial correlation function $W(r)$ between unimodal and bimodal microstructures mentioned in (4.12), quantitative measurements for the attenuation and backscattering coefficients of bimodal microstructures are proposed as follows:

$$\alpha^{Bi}(f) = F_{SG}\alpha^{SG}(f) + F_{LG}\alpha^{LG}(f) \tag{4.13}$$

$$\eta^{Bi}(f) = F_{SG}\eta^{SG}(f) + F_{LG}\eta^{LG}(f) \tag{4.14}$$

These expressions provide statistical estimations of the attenuation and backscattering coefficients in the single-phase, equiaxed and macroscopically homogeneous and isotropic polycrystalline microstructure with bimodal grain size distribution. It is concluded that the ultrasonic attenuation and backscattering levels in bimodal microstructures is determined by the volume fraction of their constituent grains.

4.2.4.2 Numerical validation

Numerical validation of the analytical relations of ultrasonic attenuation between the unimodal and bimodal microstructures predicted by (4.13) is conducted respectively in bimodal microstructures with grain sizes of 80μm and 320μm, 80μm and 160μm, as well as 80μm and 20μm. In the considered frequency region, the scattering characteristics combing the Rayleigh region and the Rayleigh-to-stochastic transition region is expected to be observed in the bimodal microstructure with the grain sizes of 80μm and 20μm. Three volume fractions of the larger grains $F_{LG} = 10\%$, 45% and 80% are investigated for each bimodal medium. The numerical estimation for each case of F_{LG} is averaged over eight samples with different grain location distributions including different types of location distributions of the larger grain. Exceptionally, due to the particular shape of regular hexagons, only the banded microstructure is studied for the bimodal microstructure with grain sizes of 80μm and 160μm.

Fig. 4.26. shows the averaged numerical measures of attenuation coefficient for bimodal microstructures with grain sizes of 80μm and 320μm. It is first compared to the analytical prediction by (4.13). The identical variation tendency and similar magnitude between the numerical estimations and analytical predictions for each volume fraction are observed. It is indicated that the linear combination of the attenuation coefficients in single-size microstructures with the respective volume fraction of each grain size provides a good estimation of the one in the double-size microstructure.

On the other hand, FE simulations of ultrasonic wave propagation within unimodal media with the grain sizes equal to the equivalent area diameters have been conducted, which are respectively 84μm , 105μm and 160μm for three volume fractions $F_{LG} = 10\%, 45\%$ and 80% . Comparison of the numerically measured attenuation coefficients between unimodal and bimodal microstructures with the same equivalent area diameter is also shown in Fig. 4.26.. For a low fraction of the larger grains $F_{LG} = 10\%,$ it seems that unimodal and bimodal microstructures with the same equivalent area diameter show a consistent variation tendency but with a notable discrepancy around the intersection point. Otherwise, for the fraction of the larger grains $F_{LG} = 45\%$, more and more significant discrepancy between the unimodal and bimodal microstructures at high frequencies $f > 6$MHz is noticed, with the attenuation in bimodal microstructure retaining in-between the ones of unimodal microstructures, whereas the other increasing rapidly and slight superior to the attenuation of the sample with 80μm . Similar phenomenon is observed for the bimodal microstructure with a relatively high fraction of the larger grains $F_{LG} = 80\%$. It is indicated that the equivalent area diameter is not a good approximation for the prediction of ultrasonic attenuation in the bimodal microstructure with a high volume fraction of the larger grains.

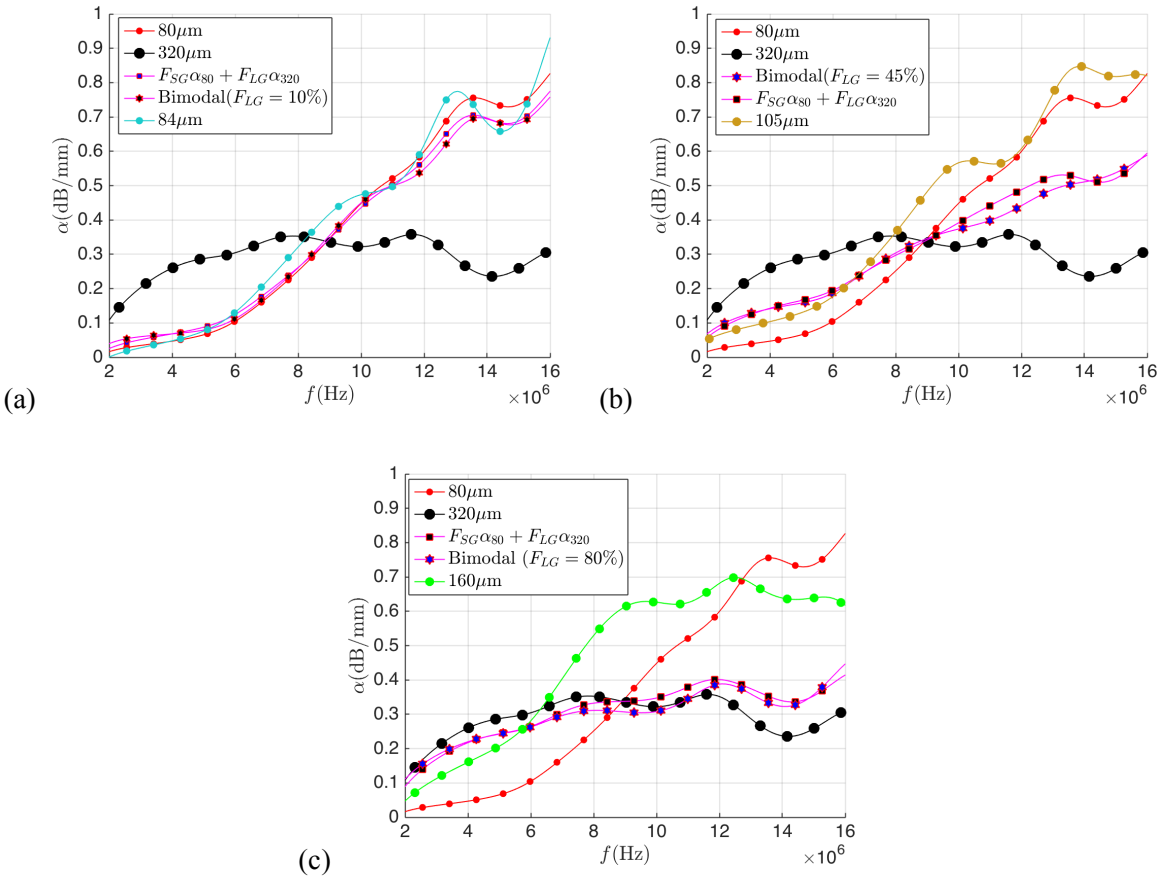

Fig. 4.26. Comparison between the analytical predictions and the numerical estimations for attenuation coefficient in bimodal microstructures containing grain sizes of 80μm and 320μm with the volume fraction of the larger grains (a) $F_{LG} = 10\%$, (b) $F_{LG} = 45\%$ and (c) $F_{LG} = 80\%$.

Numerical estimations for ultrasonic attenuation in bimodal microstructures with grain sizes of 80μm and 160μm, as well as 80μm and 20μm are presented in Fig. 4.27.. Overall, for each case of the volume fraction of the larger grains, the attenuation coefficient in bimodal microstructure is as expected in-between the ones of unimodal microstructures, and good consistence with the analytical estimation determined by the volume fraction of the constituent grains (predicted by (4.13)) is observed.

Particularly, for the bimodal microstructure with grain sizes of 80μm and 160μm, the attenuation coefficient roughly goes across the intersection point between two unimodal media at the frequency 13MHz. Almost identical attenuation level to the analytical prediction is observed before the intersection point for each volume fraction of the larger grain. However, the numerical estimation is quantitatively smaller than the analytical prediction after the intersection point, especially for the fraction of $F_{LG} = 10\%$ and 45%. This point is not yet been understood well. Considering the more and more significant dispersions of the attenuation as the increase of frequency between unimodal samples with different spatial distributions of crystallographic orientations (shown in Fig. 4.3.(a) and Fig. 4.3.(b)), it is believed

that increasing the number of samples can probably improve the comparison between the numerical and analytical estimations in the high frequency region.

Furthermore, for the bimodal microstructure with grain sizes of 80μm and 20μm, different from the two bimodal microstructures with grain sizes of 80μm and 160μm, 80μm and 320μm, no intersection point is observed between the unimodal and bimodal microstructures. In fact, for the studied wavelength range of 375μm-3000μm, the grain size of 20μm shows the Rayleigh scattering behavior with the fourth degree power law dependence of the attenuation on frequency and thus exhibits an insignificant attenuation level compared to the grain size of 80μm. By contrast, the attenuation for the grain size of 80μm increases rapidly with an approximately second degree power law dependence on frequency. The intersection between the attenuation of these two grain sizes occurs at a higher frequency.

As discussed in Section 4.1.2.2, limited by the number of contributing grains, a certain number of samples with different spatial distributions of crystallographic orientations are necessary to plot a curve of ultrasonic backscattering coefficient with recognisable variation tendency. Considering the computational cost, numerical confirmation of the analytical estimation for ultrasonic backscattering by (4.14) is carried out only in bimodal microstructures containing grain sizes of 80μm and 320μm. Three different volume fractions of the larger grains F_{LG}, and 20 samples with different larger grain location distributions X_{LG} for each case of F_{LG} are studied.

Frequency dependence of the averaged backscattering coefficients for each case of F_{LG} are shown in Fig. 4.28.. Overall, the numerical result for each volume fraction is in-between the backscattering coefficients of unimodal microstructures and intersects with them approximately at the frequency $f = 8\text{MHz}$. Comparison of the numerical estimations with the analytical predictions by (4.14) shows good coherence both in the variation tendency and the magnitude. Careful observations demonstrate a little more significant fluctuations in high frequency region between the averaged numerical estimation and the analytical prediction for the volume fraction $F_{LG} = 45\%$. Actually, the grain size of 80μm makes a dominant contribution to the backscattered noise level within the bimodal microstructure containing grain sizes of 80μm and 320μm at high frequencies. Due to the existence of 45% larger grains for each sample, the number of grain boundaries in the bimodal microstructure through which the wave propagates is much less than that in unimodal microstructure with the grain size of 80μm. Accordingly, based on the same number of samples, more obvious oscillations for the backscattering coefficient of bimodal microstructures are observed than the one of unimodal microstructures.

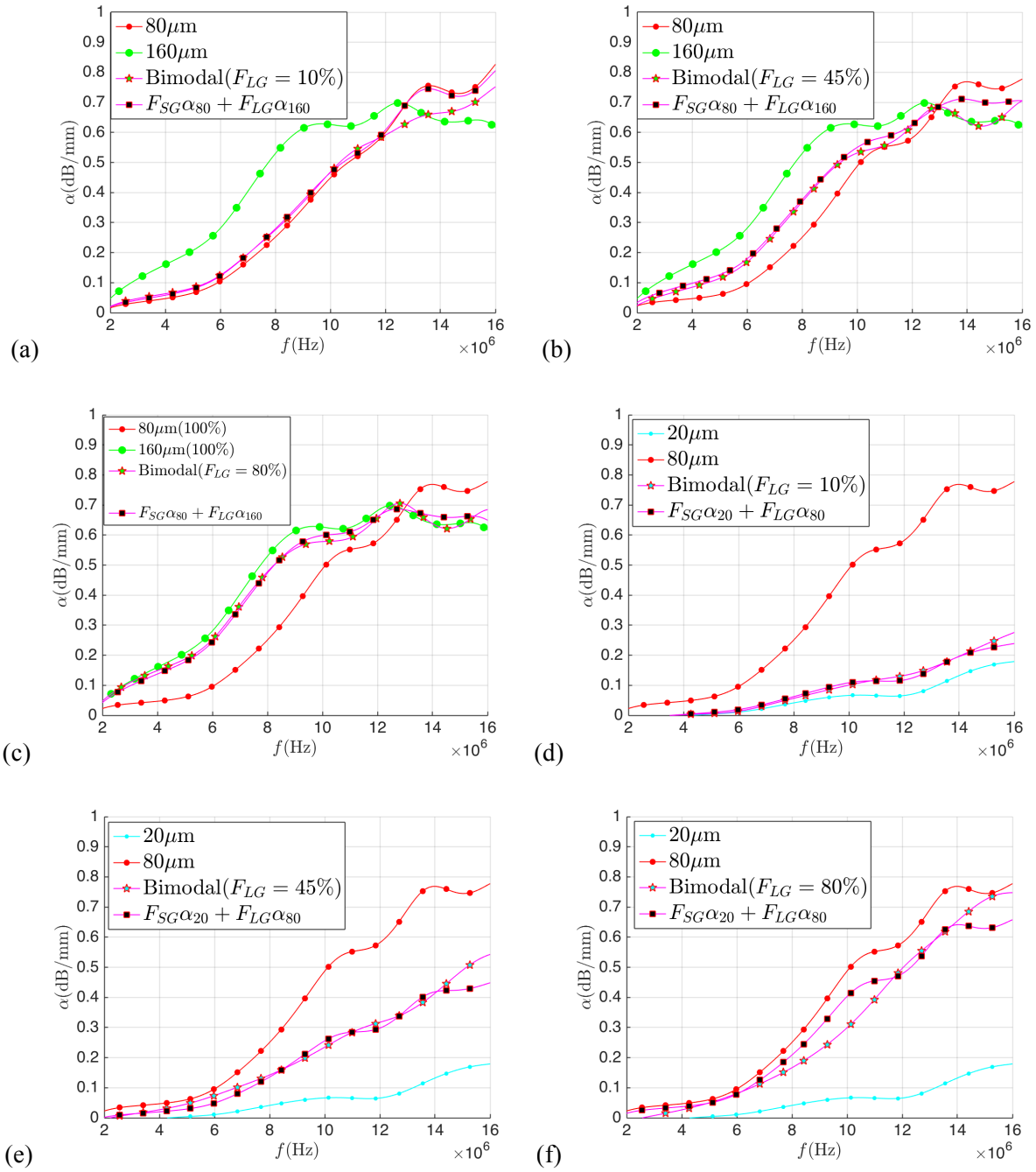

Fig. 4.27. Comparison between the analytical prediction and the numerical estimation for the attenuation coefficient in bimodal microstructures comprising double-size grains of 80μm and 160μm with the volume fraction of the larger grains (a) $F_{LG} = 10\%$, (b) $F_{LG} = 45\%$, and (c) $F_{LG} = 80\%$; and bimodal microstructures comprising double-size grains of 80μm and 20μm with the volume fraction of the larger grains (d) $F_{LG} = 10\%$, (e) $F_{LG} = 45\%$, and (f) $F_{LG} = 80\%$.

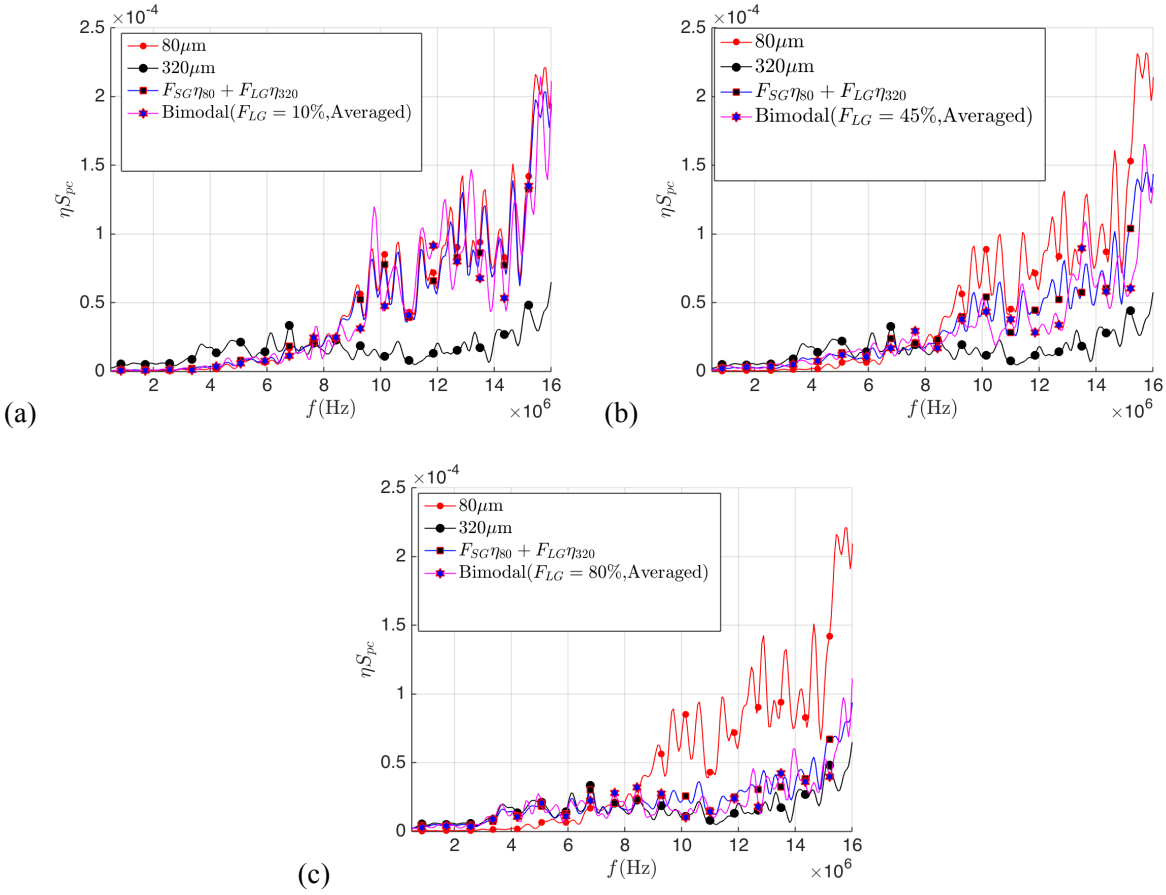

Fig. 4.28. Comparison between the analytical prediction and the numerical estimation for the backscattering coefficient in bimodal microstructures comprising double-size grains of 80μm and 320μm with the volume fraction of the larger grains (a) $F_{LG} = 10\%$, (b) $F_{LG} = 45\%$ and (c) $F_{LG} = 80\%$.

4.3 Conclusions

Ultrasonic wave attenuation and backscattering in single-phase and untextured polycrystalline materials composed of equiaxed grains with unimodal or bimodal grain sizes are subsequently investigated:

-In the case of unimodal microstructures, a second power dependence on grain size and a third power dependence on frequency of the longitudinal wave attenuation coefficient in the Rayleigh scattering region are observed according to the 2D numerical simulations. Coherent comparison with the 2D analytical prediction is obtained in the low frequency region $x_0 < 2$. However, in the high frequency region ($2 < x_0 < 5.5$), the insensitivity of attenuation to frequency is observed in the numerical estimation, contrary to the theoretical prediction of a first power dependence on frequency in this Rayleigh-to-stochastic region. Concerning grain size effects on the backscattering coefficient, the increase with the normalize frequency x_0, *i.e.* the ratio of grain size to wavelength, in the low frequency region and the insensitivity to frequency in the high frequency region are observed. Coherent variation tendency and amplitudes of the frequency-dependent backscattering coefficient are

obtained between the numerical measurements and the analytical prediction. It is found that the number of grains contributing to the backscattered noise echo signals has a significant influence on the oscillatory levels of the numerically estimated backscattering coefficient. Discussions on effects of the attenuation due to the multiple scattering on the analytical quantification of the backscattering coefficient have been proposed, which concluded that the analytical predictions based on the Born approximation overestimate the backscattering coefficient at high frequencies.

-With regard to the microstructure with bimodal grain sizes, effects of different parameters on the ultrasonic propagation have been investigated, such as the volume fraction of the larger grains, the location distribution of the larger grains in the matrix composed of the smaller grains. Numerical results indicate that the attenuation and backscattering coefficients in frequency domain are in-between the ones of unimodal microstructures and are only slightly affected by the location distributions of the larger grains whatever distributions types. Investigations on the spatial autocorrelation functions provide an analytical estimation for the attenuation and backscattering coefficients in bimodal microstructures, which are proved to be determined by the volume fraction of the constituent grains. 2D numerical validation is carried out for different volume fractions of the larger grains and for three bimodal microstructures with different couples of grain sizes. Furthermore, unimodal microstructures with corresponding equivalent grain size were systematically studied numerically. Their responses in attenuation have shown that it is not possible to define an equivalent grain size that can provide a good estimation for ultrasonic wave scattering effectiveness in a bimodal microstructure in both Rayleigh and stochastic regions.

Conclusions and perspectives

The first contribution of this work consists in proposing versatile approaches to numerically evaluate ultrasonic attenuation and grain-noise scattering coefficients in polycrystalline materials by using FE modeling. It is applicable for any material regardless of its anisotropy, crystallographic or morphological textures (grain size, grain elongation, etc.), and consequently allows accessing more realistic polycrystalline microstructures in a more accurate way than classical analytical models, for which assumptions as the single scattering or the Born approximation are required. More particularly, an original method based on the reciprocity theorem for the numerical evaluation of the grain-noise scattering coefficient is developed. The advantage of using the same theoretical frameworks as classical analytical models to develop our numerical method is that it allows to validate the latter in the cases of idealized textures for which the considered analytical models can be applied and remain relevant. The effect of multiple scattering is automatically included in the numerical measure of the ultrasonic attenuation and grain-noise scattering coefficients as actual scattered fields are solved by FE simulations.

Secondly, 2D analytical formulas for both ultrasonic attenuation and backscattering coefficients in single-phase and untextured polycrystals composed of equiaxed grains with cubic symmetry are developed. Concerning the attenuation coefficient, it is found that the Rayleigh scattering is linked closely to the scattering cross section and therefore the attenuation coefficient in the 2D model reduces from a third to a second power dependence on grain size, and from a fourth to a third power dependence on frequency compared to the 3D model. Explicit formulas for two components of the longitudinal wave attenuation, *i.e.* the longitudinal-to-longitudinal and longitudinal-to-shear wave attenuations, are developed within the framework of the Stanke-Kino unified theory. They are formulated based on the Born approximation and an additional assumption that the displacement vector $\boldsymbol{U}$ of the quasi-longitudinal wave is parallel to the wave vector $\boldsymbol{k}$, valid only for weakly-scattering materials. It is demonstrated that the longitudinal wave attenuation in the Rayleigh region is determined by the longitudinal-to-shear wave scattering generated by wave mode conversion, whereas the longitudinal-to-longitudinal wave scattering dominates the attenuation in the stochastic region. Concerning the backscattering coefficient, an important coefficient of proportionality is given in the 2D case considering the equivalence under the weak-scattering approximation of the reciprocity formulation and the isolated scatter model for evaluation of grain-noise scattering. It is proved to depend on spatial dimension, frequency and material properties. Analytical predictions involving this coefficient show that in the 2D case the Rayleigh-to-stochastic transition occurs earlier, and the backscattering coefficient is significantly larger than in the 3D case.

Thirdly, the proposed numerical approach is applied to quantifying grain size effects on ultrasonic attenuation and backscattering coefficients in single-phase and untextured polycrystals with unimodal and bimodal grain sizes respectively:

2D numerical simulations modeling idealized microstructures composed of hexagonal grains with different unimodal grain sizes are performed. The involved frequency range with respect to the considered grain sizes is large enough so that the Rayleigh, stochastic and Rayleigh-to-stochastic transition scattering regions, are studied. Coherent variation tendency and amplitudes of both attenuation and backscattering coefficients are obtained between the numerical measurements and the analytical predictions. Concerning the attenuation coefficient, a second power dependence on grain size and a third power dependence on frequency in the Rayleigh scattering region are observed. Concerning the backscattering coefficient, the increase with the normalized frequency x_0, *i.e.* the ratio of grain size to wavelength, in low frequency region and the insensitivity to frequency in high frequency region are observed. It is found that the number of grains contributing to the backscattered noise echo signals has a significant influence on the oscillatory levels of the numerically estimated backscattering coefficient. Discussions on the attenuation effect on analytical predictions of the backscattering coefficient have been proposed, which conclude that the analytical predictions based on the Born approximation overestimate the backscattering coefficient at high frequencies. Particularly, in high frequency region corresponding to $x_0 \in [2, 5.5]$, the insensitivity of attenuation to frequency is observed in the numerical estimation, contrary to the theoretical prediction of a first power dependence on frequency in this Rayleigh-to-stochastic transition region.

2D numerical simulations modeling idealized microstructures composed of double-size grains are also performed. Effects of different parameters on the ultrasonic wave scattering have been investigated, such as volume fractions of the larger grains, location distributions of the larger grains in the matrix of the smaller grains. Numerical results indicate that the levels of attenuation and backscattering coefficients are in-between the ones of unimodal microstructures and slightly affected by the grain location distributions. Investigations on spatial autocorrelation functions provide an analytical estimation for attenuation and backscattering coefficients in bimodal microstructures, which are proved to be determined by the volume fractions of the constituent grains. 2D numerical validation is carried out for different volume fractions of the larger grains and for three bimodal microstructures with different couples of grain sizes. The capability of characterizing grain sizes and their respective volume fractions of the constituent grains in bimodal microstructures by using ultrasonic attenuation and backscattering has been demonstrated, however, the detection of grain location distribution such as banded microstructures by using ultrasonic attenuation and backscattering coefficients is not straightforward. Furthermore, unimodal microstructures with corresponding equivalent grain size were systematically studied numerically. Their responses in attenuation have shown that it is not possible to

define an equivalent grain size that can provide a good estimation for ultrasonic wave scattering effectiveness in a bimodal microstructure in both Rayleigh and stochastic regions.

Further efforts could be devoted to the following aspects:

1) In the near future, supplementary numerical simulations need to be conducted to fully understand the insensitivity of attenuation to the high frequency region ($2 < x_0 < 5.5$), which is incoherent with the theoretical prediction of a first power dependence on frequency.

2) The capability of monitoring crystallographic textures or grain elongations by ultrasonic wave scattering has been demonstrated analytically in transversely isotropic polycrystalline microstructures (Ahmed et al. 1996). It is also of interest to investigate effects of crystallographic textures or grain elongations on ultrasonic wave attenuation and backscattering coefficients.

3) Investigations on ultrasonic wave scattering in bimodal polycrystals with double-size grains has proved the capability of characterizing grain sizes and their respective volume fractions of the constituent grains by inversion of ultrasonic attenuation and backscattering. It is of interest to conduct investigations on characterizations of grain size distribution by using ultrasonic signals.

4) There are a great quantity of difficulties concerned with experimental evaluations of ultrasonic attenuation and backscattering in real complex polycrystalline materials. For example, ultrasonic wave scattering in strongly-scattering materials has been beyond the classical theoretical predictions. It is of interest to understand a number of unresolved physical issues and reveal the quantitative features of ultrasonic wave propagation by using FE modeling in real complex polycrystals, especially strongly-scattering materials.

Appendix A
The second-order Keller approximation

The general formulas for determining the average wave field $\langle \boldsymbol{u}(\boldsymbol{x}) \rangle$ in a slightly inhomogeneous medium based on the second-order perturbation theory are recalled in this section. It was developed by Keller (Keller 1964, Karal et al. 1964), and thus is named as the second-order Keller approximation (Stanke et al. 1984) nowadays. The whole medium is represented as a family of media each particular member of which differs slightly from the homogeneous medium. The wave field in each particular medium is expressed by employing the pertubation theory in the second-order of the inhomogeneity degree ξ. Assuming that the average or mean wave is a plane wave, the mean wave field is formulated accurately up to the second order of ξ, and then the propagation constant of the mean wave is solved.

A position-dependent linear operator $L(\boldsymbol{x})$ describing the unkown response of the medium to an elastic wave is proposed, and then the stochastic wave euqation in the medium without external forces is formulated as:

$$L(\boldsymbol{x})\, \boldsymbol{u}(\boldsymbol{x}) = 0 \tag{A.1}$$

Define an operator L^0 in an equivalent homogeneous medium, which is independent of $\boldsymbol{x}$ and ξ, invertible and differs slightly from $L(\boldsymbol{x})$, and then the general perturbation solution for $L(\boldsymbol{x})$ is written as:

$$L(\boldsymbol{x}) = L^0 - \xi L_1(\boldsymbol{x}) - \xi^2 L_2(\boldsymbol{x}) - o(\xi^3) \tag{A.2}$$

Here $L_1(\boldsymbol{x})$ and $L_2(\boldsymbol{x})$ are perturbing operators in the first-order and the second-order of ξ respectively. The wave field $\boldsymbol{u}(\boldsymbol{x})$ in a random medium is usually an n component vector, then L^0, $L_1(\boldsymbol{x})$ and $L_2(\boldsymbol{x})$ are n^{th}-order square matrices. Considering the wave equation in the unperturbed medium $L^0\boldsymbol{u}^0(\boldsymbol{x}) = 0$, (A.1) is rewritten as:

$$L^0\boldsymbol{u}(\boldsymbol{x}) = L^0\boldsymbol{u}^0 + \xi L_1(\boldsymbol{x})\boldsymbol{u}(\boldsymbol{x}) + \xi^2 L_2(\boldsymbol{x})\boldsymbol{u}(\boldsymbol{x}) + o(\xi^3) \tag{A.3}$$

Multiplying the inverse of L^0 at both sides of (A.3), an implicit formulation for $\boldsymbol{u}(\boldsymbol{x})$ is obtained:

$$\boldsymbol{u}(\boldsymbol{x}) = \boldsymbol{u}^0 + \xi (L^0)^{-1} L_1(\boldsymbol{x})\boldsymbol{u}(\boldsymbol{x}) + \xi^2 (L^0)^{-1} L_2(\boldsymbol{x})\boldsymbol{u}(\boldsymbol{x}) + o(\xi^3) \tag{A.4}$$

By the iteration of (A.4) itself, the perturbation solution for $\boldsymbol{u}(\boldsymbol{x})$ is expressed by the unperturbed wave field $\boldsymbol{u}^0(\boldsymbol{x})$ as follows:

$$\boldsymbol{u}(\boldsymbol{x}) = \boldsymbol{u}^0 + \xi (L^0)^{-1} L_1(\boldsymbol{x})\boldsymbol{u}^0 + \xi^2 (L^0)^{-1} \left(L_1(\boldsymbol{x})(L^0)^{-1} L_1(\boldsymbol{x}) + L_2(\boldsymbol{x}) \right) \boldsymbol{u}^0 + o(\xi^3) \tag{A.5}$$

The objective is to find the solution for the mean wave field $\langle \boldsymbol{u}(\boldsymbol{x})\rangle$ which is defined as the ensemble average:

$$\langle \boldsymbol{u}(\boldsymbol{x})\rangle = \int \boldsymbol{u}(\boldsymbol{x}) p(\boldsymbol{x}) d\boldsymbol{x} \tag{A.6}$$

Here $p(\boldsymbol{x})$ denotes the possibility density function. Taking the expectation value of (A.5), it is found that $\langle \boldsymbol{u}(\boldsymbol{x})\rangle$ satisfies the following equation:

$$\langle \boldsymbol{u}(\boldsymbol{x})\rangle = \boldsymbol{u}^0 + \xi (L^0)^{-1}\langle L_1(\boldsymbol{x})\rangle \boldsymbol{u}^0 + \xi^2 (L^0)^{-1}\left(\langle L_1(\boldsymbol{x})(L^0)^{-1} L_1(\boldsymbol{x})\rangle + \langle L_2(\boldsymbol{x})\rangle\right)\boldsymbol{u}^0 + o(\xi^3) \tag{A.7}$$

From (A.7), the expression for $\boldsymbol{u}^0(\boldsymbol{x})$ accurate up to the first-order of ξ is written as:

$$\boldsymbol{u}^0 = \langle \boldsymbol{u}(\boldsymbol{x})\rangle - \xi (L^0)^{-1}\langle L_1(\boldsymbol{x})\rangle \boldsymbol{u}^0 + o(\xi^2) \tag{A.8}$$

Substituting (A.8) into (A.7), it is found that:

$$\langle \boldsymbol{u}(\boldsymbol{x})\rangle = \boldsymbol{u}^0 + (L^0)^{-1}\left(\xi\langle L_1(\boldsymbol{x})\rangle + \xi^2\left(\langle L_1(\boldsymbol{x})(L^0)^{-1} L_1(\boldsymbol{x})\rangle - \langle L_1(\boldsymbol{x})\rangle (L^0)^{-1}\langle L_1(\boldsymbol{x})\rangle + \langle L_2(\boldsymbol{x})\rangle\right)\right)\langle \boldsymbol{u}(\boldsymbol{x})\rangle + o(\xi^3) \tag{A.9}$$

Applying L^0 to both sides of (A.9) and omitting the $\boldsymbol{o}(\xi^3)$ term, then an explicit expression for $\langle \boldsymbol{u}(\boldsymbol{x})\rangle$ accurate to ξ^2 is written as follows:

$$\left(L^0 - \xi\langle L_1(\boldsymbol{x})\rangle - \xi^2\left(\langle L_1(\boldsymbol{x})(L^0)^{-1} L_1(\boldsymbol{x})\rangle - \langle L_1(\boldsymbol{x})\rangle (L^0)^{-1}\langle L_1(\boldsymbol{x})\rangle + \langle L_2(\boldsymbol{x})\rangle\right)\right)\langle \boldsymbol{u}(\boldsymbol{x})\rangle = 0 \tag{A.10}$$

Usually, the kernel of the operator $(L^0)^{-1}$ appearing in (A.10) is the Green's tensor $\boldsymbol{G}(\boldsymbol{x}';\boldsymbol{x})$, so that $(L^0)^{-1}$ can be expressed as an integral operator in terms of $\boldsymbol{G}(\boldsymbol{x}';\boldsymbol{x})$. A Green's tensor $\boldsymbol{G}(\boldsymbol{x}';\boldsymbol{x})$ at the point $\boldsymbol{x}$ corresponding to L^0 is the solution of the equation as follows:

$$L^0 \boldsymbol{G}(\boldsymbol{x}';\boldsymbol{x}) = -\delta(\boldsymbol{x}-\boldsymbol{x}')\,\mathbf{I} \tag{A.11}$$

Then $(L^0)^{-1}$ yields the equation:

$$(L^0)^{-1}\boldsymbol{u}(\boldsymbol{x}) = \int \boldsymbol{G}^T(\boldsymbol{x}';\boldsymbol{x})\cdot \boldsymbol{u}(\boldsymbol{x}')\, d\boldsymbol{x}' \tag{A.12}$$

The terms in (A.10) which involve $(L^0)^{-1}$ are written in the integral form as:

$$\langle L_1(\boldsymbol{x})(L^0)^{-1} L_1(\boldsymbol{x})\rangle\langle \boldsymbol{u}(\boldsymbol{x})\rangle = \langle L_1(\boldsymbol{x})\int \boldsymbol{G}^T(\boldsymbol{x}';\boldsymbol{x}) L_1(\boldsymbol{x}')\langle \boldsymbol{u}(\boldsymbol{x}')\rangle d\boldsymbol{x}'\rangle \tag{A.13}$$

$$(L^0)^{-1}\langle L_1(\boldsymbol{x})\rangle\langle \boldsymbol{u}(\boldsymbol{x})\rangle = \int \boldsymbol{G}^T(\boldsymbol{x}';\boldsymbol{x})\langle L_1(\boldsymbol{x}')\rangle\langle \boldsymbol{u}(\boldsymbol{x}')\rangle d\boldsymbol{x}' \tag{A.14}$$

The main equation for $\langle \boldsymbol{u}(\boldsymbol{x})\rangle$ by the substitution of (A.13) and (A.14) into (A.10) is rewritten as:

$$\begin{aligned} 0 = {} & L^0\langle \boldsymbol{u}(\boldsymbol{x})\rangle - \xi\langle L_1(\boldsymbol{x})\rangle\langle \boldsymbol{u}(\boldsymbol{x})\rangle \\ & + \xi^2\left(\langle L_1(\boldsymbol{x})\rangle\int \boldsymbol{G}^T(\boldsymbol{x}';\boldsymbol{x})\langle L_1(\boldsymbol{x}')\rangle\langle \boldsymbol{u}(\boldsymbol{x}')\rangle d\boldsymbol{x}' - \langle L_1(\boldsymbol{x})\int \boldsymbol{G}^T(\boldsymbol{x}';\boldsymbol{x}) L_1(\boldsymbol{x}')\langle \boldsymbol{u}(\boldsymbol{x}')\rangle d\boldsymbol{x}'\rangle + \langle L_2(\boldsymbol{x})\rangle\langle \boldsymbol{u}(\boldsymbol{x})\rangle\right) \end{aligned} \tag{A.15}$$

For the case of $\langle L_1(\boldsymbol{x})\rangle = 0$, (A.15) becomes:

$$L^0\langle \boldsymbol{u}(\boldsymbol{x})\rangle - \xi^2\langle L_1(\boldsymbol{x})\int \boldsymbol{G}^T(\boldsymbol{x}';\boldsymbol{x}) L_1(\boldsymbol{x}')\langle \boldsymbol{u}(\boldsymbol{x}')\rangle d\boldsymbol{x}'\rangle + \xi^2\langle L_2(\boldsymbol{x})\rangle\langle \boldsymbol{u}(\boldsymbol{x})\rangle = 0 \tag{A.16}$$

The application of the equation (A.16) to the complex case of anisotropic characterization, where three wave modes in any progagation direction in a solid are taken into account, is presented in Section 2.1.1. Providing the mathematical definition of the operators L^0, $L_1(\boldsymbol{x})$ and $L_2(\boldsymbol{x})$ in the case of anisotropic characterization, the general expression for the expected wave field accurate up to the second order of ξ and accounting for some degree of multiple scattering is presented as (2.7).

Appendix B

Derivation of the scattered field based on individual scatterer model

Based on individual scatterer model, the scattered field $\boldsymbol{u}^{scat}(\boldsymbol{x})$ (2.69) far from the single scatterer is associated to the variation of elastic tensors from the homogeneous reference material. It is formulated in terms of the volume integration over the scatterer by using the Green's function tensor in infinite reference medium in both 3D and 2D cases. When $\boldsymbol{x} \to \infty$ the asymptotic approximations $r^{-1} \sim |\boldsymbol{x}|^{-1}$ and $r \sim |\boldsymbol{x}| - \boldsymbol{x}' \cdot \boldsymbol{e}_{scat}$ can be made, so the calculation of derivatives contained in the Green's function tensor can be simplified and the following asymptotic formulas can be written.

In the 3D case, already given by Gubernatis et al. (1977):

$$\nabla\left(\frac{\exp(ikr)}{r}\right) \sim (ik)\frac{\exp(ik|\boldsymbol{x}|)}{|\boldsymbol{x}|}\exp(-i\boldsymbol{k}\cdot\boldsymbol{x}')\,\boldsymbol{e}_{scat} \tag{B.1}$$

$$\nabla\left(\nabla\left(\frac{\exp(ikr)}{r}\right)\right) \sim (ik)^2\frac{\exp(ik|\boldsymbol{x}|)}{|\boldsymbol{x}|}\exp(-i\boldsymbol{k}\cdot\boldsymbol{x}')\,\boldsymbol{e}_{scat}\otimes\boldsymbol{e}_{scat} \tag{B.2}$$

$$\nabla\left(\nabla\left(\nabla\left(\frac{\exp(ikr)}{r}\right)\right)\right) \sim (ik)^3\frac{\exp(ik|\boldsymbol{x}|)}{|\boldsymbol{x}|}\exp(-i\boldsymbol{k}\cdot\boldsymbol{x}')\,\boldsymbol{e}_{scat}\otimes\boldsymbol{e}_{scat}\otimes\boldsymbol{e}_{scat} \tag{B.3}$$

In the 2D case:

$$H_0^{(1)}(kr) \sim \frac{1-i}{(\pi k)^{1/2}}\frac{\exp(ik|\boldsymbol{x}|)}{|\boldsymbol{x}|^{1/2}}\exp(-i\boldsymbol{k}\cdot\boldsymbol{x}') \tag{B.4}$$

$$\nabla H_0^{(1)}(kr) \sim \frac{1-i}{(\pi k)^{1/2}}(ik)\frac{\exp(ik|\boldsymbol{x}|)}{|\boldsymbol{x}|^{1/2}}\exp(-i\boldsymbol{k}\cdot\boldsymbol{x}')\,\boldsymbol{e}_{scat} \tag{B.5}$$

$$\nabla\left(\nabla H_0^{(1)}(kr)\right) \sim \frac{1-i}{(\pi k)^{1/2}}(ik)^2\frac{\exp(ik|\boldsymbol{x}|)}{|\boldsymbol{x}|^{1/2}}\exp(-i\boldsymbol{k}\cdot\boldsymbol{x}')\,\boldsymbol{e}_{scat}\otimes\boldsymbol{e}_{scat} \tag{B.6}$$

$$\nabla\left(\nabla\left(\nabla H_0^{(1)}(kr)\right)\right) \sim \frac{1-i}{(\pi k)^{1/2}}(ik)^3\frac{\exp(ik|\boldsymbol{x}|)}{|\boldsymbol{x}|^{1/2}}\exp(-i\boldsymbol{k}\cdot\boldsymbol{x}')\,\boldsymbol{e}_{scat}\otimes\boldsymbol{e}_{scat}\otimes\boldsymbol{e}_{scat} \tag{B.7}$$

Substituting these asymptotic approximations into (2.34), (2.40) and (2.69), the far-field solutions of the scattered displacement and stress fields in the 2D and 3D models can be derived to obtained (2.70)-(2.74) and (2.75)-(2.76), respectively.

Appendix C
Résumé Substantiel

La corrélation des propriétés de propagation des ondes ultrasonores avec certaines caractéristiques de la microstructure polycristalline a des implications significatives dans le contrôle non destructif. Une analyse numérique basée sur la méthode des éléments finis permettant de quantifier les coefficients d'atténuation et de diffusion ultrasonores dans un polycristal en domaine temporel et fréquentiel est présentée. Elle est a priori applicable à tout type de matériaux polycristallins quelles que soient sa texture cristallographique (degré d'anisotropie et orientation d'axes d'anisotropie des grains, etc.) ou ses caractéristiques morphologiques (la taille et la forme des grains, etc.). Elle permet par conséquent de simuler la propagation des ondes ultrasonores dans des microstructures polycristallines réelles d'une manière plus pertinente donc plus précise que des modèles analytiques classiques dans lesquelles des hypothèses telles que la diffusion simple ou l'approximation de Born sont nécessaires.

En particulier, une méthode originale basée sur le théorème de réciprocité pour l'évaluation numérique du coefficient de diffusion est proposée. L'avantage d'utiliser un même cadre théorique que les modèles analytiques classiques pour développer notre procédure de mesure numérique est qu'il permet de valider ce dernier dans les cas de textures idéalisées où les modèles analytiques considérés peuvent être appliqués et restent pertinents. Des formules analytiques bidimensionnelles (2D) pour les coefficients d'atténuation ultrasonore et de rétrodiffusion sont développées en utilisant l'approximation de Born pour valider les évaluations numériques. Concernant le coefficient d'atténuation, la modélisation 2D réduit le mécanisme de diffusion dans le régime de Rayleigh, dans lequel l'atténuation des ondes longitudinales suit en effet une loi proportionnelle au carré de la taille des grains, au lieu d'une puissance cubique obtenue dans le cas tridimensionnel (3D). Concernant le coefficient de rétrodiffusion, un coefficient multiplicateur dépendant de la fréquence et des propriétés élastiques de grain est identifié et conduit à des niveaux de bruits rétrodiffusés plus élevés et à un léger avancement dans la transition Rayleigh-stochastique en 2D qu'en 3D

Comme exemples d'application de l'approche numérique proposée, elle est appliquée au titanium, un polycristal monophasé et non texturé. Toutes les simulations présentées sont 2D.

Premièrement, des simulations sont effectuées dans des microstructures idéalisées composées de grains en taille unimodale. Différentes tailles de grains ont été étudiées. La plage de fréquence utilisée par rapport aux tailles de grain considérées est assez grande pour que les régimes de diffusion de Rayleigh et stochastique ainsi que la transition entre ces deux régimes soient impliqués. Une comparaison cohérente entre les évaluations numériques et les prédictions analytiques 2D est obtenue. Les résultats numériques montrent que les coefficients d'atténuation et de rétrodiffusion en fonction de

la fréquence normalisée, qui est le ratio entre la taille de grains et la longueur d'onde, augmentent en continu à basses fréquences et deviennent insensibles a hautes fréquences. Par ailleurs, les grandes dispersions observées pour le coefficient de rétrodiffusion entre des échantillons ayant la même taille de grains mais différentes répartitions spatiales d'orientations cristallographiques sont analysées. Il est conclu que le niveau d'oscillation de rétrodiffusion est d'autant plus significatif que le nombre de grains contribuant aux bruits reçus est insuffisant. Enfin, les effets de l'atténuation induite par la diffusion multiple sur la mesure de rétrodiffusion, qui sont négligés par les modèles théoriques, sont quantifiés.

Deuxièmement, l'approche numérique proposée est appliquée aux polycristaux composés de grains en taille bimodale, fréquemment observés lors de la recristallisation avec une croissance hétérogène de grains. L'avantage de la modélisation numérique est mis en évidence dans ce cas, car aucun modèle analytique n'existe. Les effets de différents paramètres sur l'atténuation ultrasonore et la rétrodiffusion sont étudiés, tels que la fraction volumique et la répartition aléatoire des gros grains, la répartition et la taille des îlots de gros grains dans la matrice des petits grains, voire les microstructures en couches formées respectivement de gros grains et de petits grains. Les résultats numériques indiquent que les coefficients d'atténuation et de rétrodiffusion en domaine fréquentiel se situent au milieu des coefficients pour les microstructures unimodales et sont principalement déterminés par les fractions volumiques des grains constitutifs. Cependant, ils ne sont que légèrement affectés par la répartition des gros grains. Il est conclu que retrouver les caractéristiques de la microstructure en couches avec différentes tailles de grains, à partir des mesures des coefficients d'atténuation ou de rétrodiffusion ultrasonores n'est pas immédiat, contrairement à l'identification des fractions volumiques. Une étude de la fonction d'autocorrélation spatiale dans des telles microstructures bimodales est proposée afin d'obtenir une interprétation analytique des phénomènes expérimentés numériquement.

Bibliography

Ahmed, S., and Thompson, R. B. (1995). Influence of columnar microstructure on ultrasonic backscattering. In "*Review of Progress in Quantitative Nondestructive Evaluation*", pp. 1617-1624. Springer.

Ahmed, S., and Thompson, R. B. (1996). Propagation of elastic waves in equiaxed stainless-steel polycrystals with aligned [001] axes. *Journal of the Acoustical Society of America*, **99**, 2086-2096.

Ahmed, S., Thompson, R. B., and Panetta, P. D. (2003). Ultrasonic attenuation as influenced by elongated grains. *Review of Progress in Quantitative Nondestructive Evaluation, Vols 22a and 22b*, **20**, 109-116.

Alford, R. M., Kelly, K. R., and Boore, D. M. (1974). Accuracy of finite-difference modeling of the acoustic wave equation. *Geophysics*, **39**, 834-842.

Auld, B. A. (1979). General Electro-Mechanical Reciprocity Relations Applied to the Calculation of Elastic Wave Scattering Coefficients. *Wave Motion*, **1**, 3-10.

Bécache, E., Joly, P., and Tsogka, C. (2000). An analysis of new mixed finite elements for the approximation of wave propagation problems. *SIAM Journal on Numerical Analysis*, **37**, 1053-1084.

Bécache, E., Joly, P., and Tsogka, C. (2002). A new family of mixed finite elements for the linear elastodynamic problem. *SIAM Journal on Numerical Analysis*, **39**, 2109-2132.

Bhatia, A. B. (1959). Scattering of High-Frequency Sound Waves in Polycrystalline Materials. *Journal of the Acoustical Society of America*, **31**, 16-23.

Chassignole, B., Duwig, V., Ploix, M. A., Guy, P., and El Guerjouma, R. (2009). Modelling the attenuation in the ATHENA finite elements code for the ultrasonic testing of austenitic stainless steel welds. *Ultrasonics*, **49**, 653-658.

Chassignole, B., El Guerjouma, R., Ploix, M. A., and Fouquet, T. (2010). Ultrasonic and structural characterization of anisotropic austenitic stainless steel welds: Towards a higher reliability in ultrasonic non-destructive testing. *NDT & E International*, **43**, 273-282.

Du, H. L., and Turner, J. A. (2014). Ultrasonic attenuation in pearlitic steel. *Ultrasonics*, **54**, 882-887.

Dupond, O., Feuilly, N., Chassignole, B., Fouquet, T., Moysan, J., and Corneloup, G. (2011). Relation between ultrasonic scattering and microstructure of polycrystalline materials. In "*Journal of Physics: Conference Series*", *Vol. 269*, pp. 012010. IOP Publishing.

Eringen, A. C., Suhubi, E. S., and Elastodynamics, V. (1975). 2, Linear theory. Academic Press, New York.

Fellinger, P., Marklein, R., Langenberg, K. J., and Klaholz, S. (1995). Numerical modeling of elastic wave propagation and scattering with EFIT—elastodynamic finite integration technique. *Wave motion*, **21**, 47-66.

Fornberg, B. (1988). The pseudospectral method: accurate representation of interfaces in elastic wave calculations. *Geophysics*, **53**, 625-637.

Garcin, T., Schmitt, J. H., and Militzer, M. (2016). In-situ laser ultrasonic grain size measurement in superalloy INCONEL 718. *Journal of Alloys and Compounds*, **670**, 329-336.

Ghoshal, G., and Turner, J. A. (2009). Numerical model of longitudinal wave scattering in polycrystals. *IEEE transactions on ultrasonics, ferroelectrics, and frequency control*, **56**, 1419-1428.

Grede, A., Tie, B., and Aubry, D. (2006). Elastic wave propagation in hexagonal honeycomb sandwich panels: Physical understanding and numerical modeling. In "*Journal de Physique IV (Proceedings)*", *Vol. 134*, pp. 507-514. EDP sciences.

Gubernatis, J. E., Domany, E., and Krumhansl, J. A. (1977a). Formal Aspects of Theory of Scattering of Ultrasound by Flaws in Elastic-Materials. *Journal of Applied Physics*, **48**, 2804-2811.

Gubernatis, J. E., Domany, E., Krumhansl, J. A., and Huberman, M. (1977b). Born Approximation in Theory of Scattering of Elastic-Waves by Flaws. *Journal of Applied Physics*, **48**, 2812-2819.

Han, Y. K., and Thompson, R. B. (1997). Ultrasonic backscattering in duplex microstructures: Theory and application to titanium alloys. *Metallurgical and Materials Transactions a-Physical Metallurgy and Materials Science*, **28**, 91-104.

Hartwig, K. T., Wang, J., Baars, D. C., Bieler, T. R., Mathaudhu, S. N., and Barber, R. E. (2007). Microstructural refinement of niobium for superconducting rf cavities. *IEEE Transactions on Applied Superconductivity*, **17**, 1305-1309.

Hirsekorn, S. (1982). The Scattering of Ultrasonic-Waves by Polycrystals. *Journal of the Acoustical Society of America*, **72**, 1021-1031.

Hirsekorn, S. (1986). Directional Dependence of Ultrasonic Propagation in Textured Polycrystals. *Journal of the Acoustical Society of America*, **79**, 1269-1279.

Hughes, T. J. R., and Hulbert, G. M. (1988). Space-time finite element methods for elastodynamics: formulations and error estimates. *Computer methods in applied mechanics and engineering*, **66**, 339-363.

Huthwaite, P. (2014). Accelerated finite element elastodynamic simulations using the GPU. *Journal of Computational Physics*, **257**, 687-707.

Karal, F. C., and Keller, J. B. (1964). Elastic Electromagnetic and Other Waves in Random Medium. *Journal of Mathematical Physics*, **5**, 537-547.

Keller, J. B. (1964). Stochastic equations and wave propagation in random media. In "*Proceeding of the 16th symposium on applied mathematics*", pp. 145-179. American mathematical society.

Kino, G. S. (1978). Application of Reciprocity Theory to Scattering of Acoustic-Waves by Flaws. *Journal of Applied Physics*, **49**, 3190-3199.

Kino, G. S., and Khuri-Yakub, B. T. (1992). Application of the reciprocity theorem to nondestructive evaluation. *Research in Nondestructive Evaluation*, **4**, 193-204.

Komatitsch, D. and Vilotte, J. P. (1998). The spectral element method: An efficient tool to simulate the seismic response of 2D and 3D geological structures. *Bulletin of the seismological society of America*, **88** (2), 368-392.

Kube, C. M., and Turner, J. A. (2015). Ultrasonic attenuation in polycrystals using a self-consistent approach. *Wave Motion*, **57**, 182-193.

Kumar, S., Kurtz, S. K., Banavar, J. R., and Sharma, M. G. (1992). Properties of a three-dimensional Poisson-Voronoi tesselation: A Monte Carlo study. *Journal of Statistical Physics*, **67**, 523-551.

Lhémery, A., Calmon, P., Lecœur-Taıbi, I., Raillon, R., & Paradis, L. (2000). Modeling tools for ultrasonic inspection of welds. *NDT & E International*, **33** (7), 499-513.

Li, X. D., and Wiberg, N. E. (1998). Implementation and adaptivity of a space-time finite element method for structural dynamics. *Computer Methods in Applied Mechanics and Engineering*, **156**, 211-229.

Lindh-Ulmgren, E., Ericsson, M., Artymowicz, D., and Hutchinson, B. (2004). Laser-ultrasonics as a technique to study recrystallisation and grain growth. *Recrystallization and Grain Growth, Pts 1 and 2*, **467**, 1353-1362.

Liu, E., and Zhang, Z. (2001). Numerical study of elastic wave scattering by cracks or inclusions using the boundary integral equation method. *Journal of Computational Acoustics*, **9**, 1039-1054.

Margetan, F. J., Gray, T. A., and Thompson, R. B. (1991). A technique for quantitatively measuring microstructurally induced ultrasonic noise. In "*Review of Progress in Quantitative Nondestructive Evaluation*", pp. 1721-1728. Springer.

Margetan, F. J., Han, K. Y., Yalda-Mooshabad, I., Goettsch, S., and Thompson, R. B. (1995). The practical application of grain noise models in titanium billets and forgings. In "*Review of Progress in Quantitative Nondestructive Evaluation*", pp. 2129-2136. Springer.

Margetan, F. J., Haldipur, P., Yu, L., and Thompson, R. B. (2005a). Looking for Multiple Scattering Effects in Backscattered Ultrasonic Grain Noise from Jet-Engine Nickel Alloys. In "*Review of Progress in Quantitative Nondestructive Evaluation*", *Vol. 760*, **1**, 75-82. AIP Publishing.

Margetan, F. J., Panetta, P. D., and Thompson, R. B. (1998). Ultrasonic signal attenuation in engine titanium alloys. In "*Review of Progress in Quantitative Nondestructive Evaluation*", pp. 1469-1476. Springer.

Margetan, F. J., Thompson, R. B., and Yalda-Mooshabad, I. (1993). Modeling ultrasonic microstructural noise in titanium alloys. In "*Review of Progress in Quantitative Nondestructive Evaluation*", pp. 1735-1742. Springer.

Margetan, F. J., Thompson, R. B., and Yalda-Mooshabad, I. (1994). Backscattered microstructural noise in ultrasonic toneburst inspections. *Journal of nondestructive evaluation*, **13**, 111-136.

Margetan, F. J., Yu, L. X., and Thompson, R. B. (2005b). Computation of grain-noise scattering coefficients for ultrasonic pitch/catch inspections of metals. In "*Review of Progress in Quantitative Nondestructive Evaluation", Vols 24A and 24B*, **760**, 1300-1307.

Panetta, P. D., and Thompson, R. B. (1999). Ultrasonic attenuation in duplex titanium alloys. In "*Review of Progress in Quantitative Nondestructive Evaluation*", pp. 1717-1724. Springer.

Petry, W., Heiming, A., Trampenau, J., Alba, M., Herzig, C., Schober, H. R., & Vogl, G. (1991). Phonon dispersion of the bcc phase of group-IV metals. I. bcc titanium. *Physical Review B*, **43**(13), 10933.

Ram, P. B.-M. (1988). Le filtrage numérique. Sybex.

Rose, J. H. (1992). Ultrasonic backscatter from microstructure. In "*Review of Progress in Quantitative Nondestructive Evaluation*", *Vol. 11*, pp. 1677-1684.

Rose, C., Rupin, F., Fouquet, T., and Chassignole, B. (2014). ATHENA 3D: A finite element code for ultrasonic wave propagation. In "*Journal of Physics: Conference Series*", *Vol. 498*, pp. 012009. IOP Publishing.

Schubert, F., and Köhler, B. (2001). Three-dimensional time domain modeling of ultrasonic wave propagation in concrete in explicit consideration of aggregates and porosity. *Journal of computational acoustics*, **9**, 1543-1560.

Shahjahan, S., Rupin, F., Aubry, A., Chassignole, B., Fouquet, T., and Derode, A. (2014). Comparison between experimental and 2-D numerical studies of multiple scattering in Inconel600® by means of array probes. *Ultrasonics*, **54**, 358-367.

Stanke, F. E. (1986). Spatial Autocorrelation Functions for Calculations of Effective Propagation Constants in Polycrystalline Materials. *Journal of the Acoustical Society of America*, **80**, 1479-1485.

Stanke, F. E., and Kino, G. S. (1984). A Unified Theory for Elastic Wave-Propagation in Polycrystalline Materials. *Journal of the Acoustical Society of America*, **75**(3), 665-681.

Thebault, J. (2009). *Etudes expérimentale et numérique des mécanismes de déformation et de recristallisation de l'UDIMET 720 lors du forgeage. Relations entre la microstructure et la perméabilité aux ultrasons* (Doctoral dissertation, Châtenay-Malabry, Ecole centrale de Paris).

Thompson, R. B., Margetan, F. J., Haldipur, P., Yu, L., Li, A., Panetta, P., and Wasan, H. (2008). Scattering of elastic waves in simple and complex polycrystals. *Wave Motion*, **45**, 655-674.

Thompson, R. B., Yu, L. X., and Margetan, F. J. (2005). A formal theory for the spatial correlation of backscattered ultrasonic grain noise. *Review of Progress in Quantitative Nondestructive Evaluation, Vols 24A and 24B*, **760**, 1292-1299.

Tie, B., and Aubry, D. (2006). Adaptive time discontinuous Galerkin method for numerical modelling of wave propagation in shell and 3D structures. *European Journal of Computational Mechanics/Revue Européenne de Mécanique Numérique*, **15**(6), 729-757.

Tie, B., Aubry, D., and Boullard, A. (2003). Adaptive computation for elastic wave propagation in plate/shell structures under moving loads. *Revue Européenne des Eléments* **12**, 717-736 .

Tie, B., Aubry, D., Grédé, A., and Roux, P. (2005). Numerical modeling of elastic wave propagation in honeycomb sandwich panels under moving loads: application to space launcher. In "*6th International Symposium on Launcher Technologies*", pp. 12-pages.

Tie, B., Solas, D., Thébault, J., Rey, C., Baudin, T., and Mouronval, A.-S. (2010). Modélisation numérique de la propagation des ultrasons dans des milieux polycristallins. *10th French Congress of Acoustics (CFA2010)*, Lyon, France.

Torquato, S. (2013). Random heterogeneous materials: microstructure and macroscopic properties. Springer Science & Business Media.

Turner, J. A. (1999). Elastic wave propagation and scattering in heterogeneous, anisotropic media: Textured polycrystalline materials. *Journal of the Acoustical Society of America*, **106**, 541-552.

Van Pamel, A., Brett, C. R., Huthwaite, P., and Lowe, M. J. S. (2015). Finite element modelling of elastic wave scattering within a polycrystalline material in two and three dimensions. *The Journal of the Acoustical Society of America*, **138**, 2326-2336.

Weaver, R. L. (1990). Diffusivity of Ultrasound in Polycrystals. *Journal of the Mechanics and Physics of Solids*, **38**, 55-86.

Yang, L., Li, J., Lobkis, O. I., and Rokhlin, S. I. (2012). Ultrasonic Propagation and Scattering in Duplex Microstructures with Application to Titanium Alloys. *Journal of Nondestructive Evaluation*, **31**, 270-283.

Yang, L., Lobkis, O. I., and Rokhlin, S. I. (2011). Shape effect of elongated grains on ultrasonic attenuation in polycrystalline materials. *Ultrasonics*, **51**, 697-708.

Zeng, F., Agnew, S. R., Raeisinia, B., and Myneni, G. R. (2010). Ultrasonic Attenuation Due to Grain Boundary Scattering in Pure Niobium. *Journal of Nondestructive Evaluation*, **29**, 93-103.

Zhang, X. G., Simpson, W. A., Vitek, J. M., Barnard, D. J., Tweed, L. J., and Foley, J. (2004). Ultrasonic attenuation due to grain boundary scattering in copper and copper-aluminum. *Journal of the Acoustical Society of America*, **116**, 109-116.

Titre : Modélisation par éléments finis de la propagation des ondes ultrasonores dans des matériaux polycristallins

Mots clés : Eléments Finis, Matériaux Polycristallins, Atténuation et Rétrodiffusion Ultrasonore

Résumé : Une analyse numérique basée sur la méthode des éléments finis permettant de quantifier les coefficients d'atténuation et de diffusion ultrasonores dans un polycristal en domaine temporel et fréquentiel est présentée. En particulier, une méthode originale basée sur le théorème de réciprocité pour l'évaluation numérique du coefficient de diffusion est proposée. Des formules analytiques bidimensionnelles (2D) pour les coefficients d'atténuation ultrasonore et de rétrodiffusion sont développées en utilisant l'approximation de Born pour valider les évaluations numériques. L'approche numérique proposée est appliquée au titanium, un polycristal monophasé et non texturé. Premièrement, des simulations sont effectuées dans des microstructures idéalisées composées de grains en taille unimodale. Une comparaison cohérente entre les évaluations numériques et les prédictions analytiques 2D est obtenue. Par ailleurs, les effets de l'atténuation induite par la diffusion multiple sur la mesure de rétrodiffusion, qui sont négligés par les modèles théoriques, sont quantifiés. Deuxièmement, l'approche numérique proposée est appliquée aux polycristaux composés de grains en taille bimodale. Les résultats numériques indiquent que les coefficients d'atténuation et de rétrodiffusion en domaine fréquentiel se situent au milieu des coefficients pour les microstructures unimodales et sont principalement déterminés par les fractions volumiques des grains constitutifs. Cependant, ils ne sont que légèrement affectés par la répartition des gros grains. Une étude de la fonction d'autocorrélation spatiale dans des telles microstructures bimodales est proposée afin d'obtenir une interprétation analytique des phénomènes expérimentés numériquement.

Title : Finite element modeling of ultrasonic wave propagation in polycrystalline materials

Keywords : Finite Element, Polycrystalline Materials, Ultrasonic Attenuation and Backscattering

Abstract : A numerical approach based on the finite element method to quantify ultrasonic attenuation and grain-noise scattering coefficients in both time and frequency domains for polycrystalline materials is presented. More particularly, an original method based on the reciprocity theorem for the numerical evaluation of the grain-noise scattering coefficient is proposed. Two-dimensional (2D) analytical formulas of ultrasonic attenuation and backscattering coefficients are developed by using the Born approximation to validate numerical evaluations. Then the proposed numerical approach is applied to the single-phase and un-textured polycrystalline titanium. Firstly, 2D FE simulations are performed in idealized microstructures composed of equiaxed grains with different unimodal grain sizes. Coherent comparison between numerical estimates and 2D analytical predictions is obtained. Effects of attenuation due to multiple scattering on the backscattering measurement, which are neglected in the theoretical model, are quantified. Secondly, polycrystals with bimodal grain sizes are considered. Numerical results indicate that attenuation and backscattering coefficients in bimodal microstructures are in-between the ones of unimodal microstructures and are mainly determined by volume fractions of the constituent grains. However they are only slightly affected by the grain location distributions. The spatial autocorrelation function in bimodal microstructures is further quantified to gain an analytical interpretation of the above phenomena.